MOLECULAR GAS IN DUSTY HIGH-REDSHIFT GALAXIES

By

CHELSEA ELECTRA SHARON

A dissertation submitted to the

Graduate School—New Brunswick

Rutgers, The State University of New Jersey

in partial fulfillment of the requirements

for the degree of

Doctor of Philosophy

Graduate Program in Physics and Astronomy

written under the direction of

Dr. Andrew J. Baker

and approved by

_____

_____

_____

_____

_____

New Brunswick, New Jersey

May, 2013

ABSTRACT OF THE DISSERTATION

Molecular Gas in Dusty High-redshift Galaxies

By CHELSEA ELECTRA SHARON

Dissertation Director:

Dr. Andrew J. Baker

We present high-resolution observations of carbon monoxide (CO) emission lines for three high-redshift galaxies in order to determine their molecular gas and star formation properties. These galaxies (SMM J14011+0252, SMM J00266+1708, and SDSS J0901+1814) have large infrared luminosities, which imply high dust enshrouded star formation rates and substantial molecular gas masses. We observed these sources using the Robert C. Byrd Green Bank Telescope, the Karl G. Jansky Very Large Array, the Plateau de Bure Interferometer, and the Submillimeter Array in order to obtain measurements of multiple CO spectral lines, allowing us to determine the physical conditions of the molecular gas. Our high resolution and multi-line CO mapping of SMM J00266+1708 reveals that it is a pair of merging galaxies, whose two components have different gas excitation conditions and different gas kinematics. For SMM J14011+0252 (J14011), we find a near-unity CO(3–2)/CO(1–0) intensity ratio, consistent with a single phase (i.e., a single temperature and density) of molecular gas and different from the average population value for dusty galaxies selected at submillimeter wavelengths. Our radiative transfer modeling (using the large velocity gradient approximation) indicates that converting the CO line luminosity to molecular gas mass requires a Galactic (disk-like) scale factor rather than the typical conversion factor assumed for starbursts. Despite this choice of conversion factor, J14011 falls

in the same region of star formation rate surface density and gas mass surface density (the Schmidt-Kennicutt relation) as other starburst galaxies. SDSS J0901+1814 (J0901) was initially selected as a star-forming galaxy at ultraviolet wavelengths, but also has a large infrared luminosity. We use the magnification provided by the strong gravitational lensing affecting this system to examine the spatial variation of the CO excitation within J0901. We find that the CO(3–2)/CO(1–0) line ratio is higher in central regions than in extended structure, supporting a picture of the molecular gas where regions of higher excitation gas (higher temperature and density) are embedded in an extended low excitation phase. We also examine the resolved Schmidt-Kennicutt relation as a function of CO line excitation for J0901 and find no systematic difference between the best-fit power law indices for the two emission lines.

Acknowledgments

First, I would like to thank my advisor, Andrew Baker, for being a true mentor in all aspects of my career—imagining a better advisor would likely require breaking laws of nature, like the finite speed of typing and being in multiple places at once. I would also like to thank my thesis committee members (Jolie Cizewski, Eric Gawiser, Andrew Harris, and Jack Hughes) for their helpful career guidance and insightful questions. I would especially like to thank Eric Gawiser and Andrew Harris for their tireless letter writing efforts during job application season.

I would also like to thank the Rutgers astronomy group—everyone's door has always been open, and it has been a wonderful environment in which to be a student. I also have to thank the other astronomy grad students for being good friends and providing me with a healthy amount of distraction in the office. I would particularly like to thank Robert Lindner for his helpful discussions of all things technical, and Curtis McCully, my perennial coffee buddy.

I would like to thank my family, Scott, Marlene, and Haley Sharon, without whom I would not be the person I am today. Lastly, I especially thank my husband, Ben Olsen, who (among a great number of other things) has always pushed me to be the best I possibly can be, both personally and in my work.

Portions of this dissertation have appeared or will appear in publication elsewhere. Chapter 3 is published as Sharon et al. (2013a) and Chapter 2 will be submitted as Sharon et al. (2013b). I would like to thank my collaborators in these works (Andrew J. Baker, Andrew I. Harris, Steven N. Longmore, Dieter Lutz, Linda J. Tacconi, and Alasdair P. Thomson) for their helpful discussions, as well as acknowledge the assistance of Clair Chandler, Ric Davies, Dennis Downes, and Rob Ivison. Chapter 4 is in preparation to be submitted to the Astrophysical Journal in collaboration with Amitpal S. Tagore, Andrew J. Baker,

Jesus Rivera, Charles R. Keeton II, Linda J. Tacconi, Dieter Lutz, David J. Wilner, Alice E. Shapley, Huan Lin, H. Thomas Diehl, Sahar S. Allam, Douglas L. Tucker, and Erin K. S. Hicks. This work has been supported by NSF grants AST-0708653 and AST-0955810, NASA grant HST-GO-11143.01-A, two GAANN fellowships, and an American Fellowship from the American Association of University Women.

Table of Contents

List of Tables

List of Figures

List of Abbreviations

AGN active galactic nucleus

ALMA Atacama Large Millimeter/submillimeter Array

ARC Astrophysics Research Consortium

BAO baryon acoustic oscillations

CASA Combined Astronomy Software Applications

CLIC Continuum and Line Interferometer Calibration

CMB cosmic microwave background

CO carbon monoxide

COBE *Cosmic Background Explorer*

FIR far-infrared

FIRAS Farr-infrared Absolute Spectrophotometer

FWHM full width half maximum

FWHP full width half power

FWZI full width zero intensity

GALEX *Galaxy Evolution Explorer*

GBT Robert C. Byrd Green Bank Telescope

GBTIDL Green Bank Telescope Interactive Data Language

GILDAS Grenoble Image and Line Data Analysis

HST *Hubble Space Telescope*

IDL Interactive Data Language

IF intermediate frequency

IGM intergalactic medium

IMF initial mass function

IR infrared

IRAM Institut de Radioastronomie Millimétrique

ISM interstellar medium

JCMT James Clerk Maxwell Telescope

LBG Lyman-break galaxy

LIRG luminous infrared galaxy

LTE local thermodynamic equilibrium

LVG large velocity gradient

MAMBO Max-Planck Millimeter Bolometer

NICMOS Near Infrared Camera and Multi-object Spectrometer

NIRSPEC Near Infrared Spectrometer

OSRO Open Shared Risk Observing

PAH polycyclic aromatic hydrocarbon

PdBI Plateau de Bure Interferometer

RMS root mean square

SAM semi-analytic model

SCUBA Submillimeter Common Use Bolometer Array

SED spectral energy distribution

SFR star formation rate

SINFONI Spectrograph for Integral Field Observations in the Near Infrared

SLED spectral line energy distribution

SMA Submillimeter Array

SMG submillimeter galaxy

S/N signal-to-noise

SNe super novae

SPIFFI Spectrograph for Infrared Faint Field Imaging

SPIRE Spectral and Photometric Imaging Receiver

sSFR specific star formation rate

ULIRG ultraluminous infrared galaxy

UV ultraviolet

VLA Karl G. Jansky Very Large Array

VLT Very Large Telescope

WIDAR Wideband Interferometric Digital Architecture

Chapter 1

Introduction

1.1 Star Formation in Galaxies

Many of the observed properties of galaxies strongly depend on their star formation histories. The winds and ultraviolet (UV) light produced by young O and B stars (with $M \gtrsim 3\,M_{\odot}$) sweep away and photodissociate the molecular gas in clouds from which the stars formed (Hollenbach & Tielens 1997). For the first galaxies, UV emission from stars was also (at least partially) responsible for re-ionizing the universe (e.g., Loeb & Barkana 2001). Over a star's lifetime, nuclear reactions create heavier elements like carbon and oxygen. These metals are released into the surrounding interstellar medium (ISM) during stars' deaths, either when they exhaust their fuel for nuclear reactions and shed their atmospheres or when they explode as supernovae (SNe). The metal enrichment of the ISM is critical for the efficient cooling necessary to create stellar populations dominated by the low mass stars we see today (e.g., Bromm & Larson 2004). If enough SNe occur during a short period within a single galaxy, the cumulative effects of the explosions create massive winds, which extend the metal enrichment to the intergalactic medium (IGM) and remove gas from the galaxy (e.g., Veilleux et al. 2005). The gas lost in outflows is no longer available to form stars or fuel the growth of galaxies' central supermassive black holes, potentially explaining the observed correlation between black hole mass and bulge mass (i.e., the $M_{\rm BH}$-σ relation; Ferrarese & Merritt 2000; Gebhardt et al. 2000), as well as preventing the excess number of massive luminous galaxies predicted in cosmological galaxy simulations that lack feedback (e.g., Cole et al. 2000). In addition, theoretical studies indicate that nuclear bursts of star formation in young galaxies may preferentially remove the lowest angular momentum gas, keeping the average angular momentum sufficiently high to produce low-redshift disk galaxies with smaller central bulges (e.g., Binney et al. 2001; Maller & Dekel 2002; Brook et al. 2011).

Therefore, in order to understand the distribution of colors, masses, morphologies, and metallicities that we see in galaxies today (and the correlations between these properties), we need to understand star formation throughout cosmic history. Since stars form from the dense cores in clouds of molecular gas, this means we must also understand the connection between galaxies' star formation rates (SFRs) and molecular gas content.

SFRs can be estimated observationally via spectral line and continuum emission throughout the electromagnetic spectrum (see review by Kennicutt & Evans 2012). These estimates assume that the SFR is proportional to the luminosity of the tracer line or continuum band, including any corrections for known limitations or biases, where the proportionality constant is calculated from stellar population synthesis models. A key limitation of these models is the necessary assumption of the distribution of stars as a function of mass, the initial mass function (IMF; Salpeter 1955; Kroupa et al. 1993; Chabrier 2003). Measurements of the SFR rely on the characteristics of high-mass stars and/or their coupling to the ISM. Since stars with larger masses have shorter lifetimes during which they fuse hydrogen into helium on the main sequence (3–15 $M_\odot$ stars have lifetimes ranging from $\sim (5 \times 10^8)$–10^7 yr, as opposed to the Sun, which has a main sequence lifetime of $\sim 10^{10}$ yr), measurements tied to the highest mass stars characterize the most recent epoch of star formation. However, different SFR estimators work better in different regimes, influencing the selection of star-forming galaxies as a function of redshift.

Since massive stars are hotter, a greater fraction of their light is emitted at UV wavelengths, and thus relatively direct estimates of the SFR use measurements of a galaxy's UV luminosity (e.g., Kennicutt 1998; Hao et al. 2011; Murphy et al. 2011). In addition, the $\lambda < 91.2$ nm UV emission of young massive stars can ionize the surrounding ISM, which in turn produces strong hydrogen recombination lines. While Lyman-α ($\lambda = 121.6$ nm) is one of the strongest emission lines, resonant scattering off the ISM makes it difficult to scale the measured line flux to the emitted flux from the stars; instead, the lowest frequency Balmer line (Hα; $\lambda = 656.3$ nm) is used. While measurements of the UV continuum for local galaxies are restricted to observations using a limited number of space-based telescopes (the *Galaxy Evolution Explorer*, *GALEX*, the *Swift UV/Optical Telescope*, and the upgraded *Hubble Space Telescope*, *HST*), the UV is shifted into optical bands for high-redshift

sources, making it a fruitful method of characterizing star formation in distant galaxies. Lyman break galaxies (LBGs; Giavalisco 2002), for example, are selected as star-forming galaxies at $z > 2$ based on their rest-UV colors, since neutral gas absorbs nearly all of a galaxy's UV-photons with wavelengths shorter than the Lyman limit ($\lambda = 91.2\,\mathrm{nm}$). A complication for both UV- and optical-wavelength star formation tracers is obscuration by dust within the ISM; dust preferentially absorbs and scatters high-frequency light, causing a net reddening of the spectral energy distribution (SED). Therefore, in order to be confident in UV and optical SFR tracers, we must apply corrections to account for dust extinction (e.g., Calzetti et al. 1994; Kong et al. 2004; Moustakas et al. 2006; Hao et al. 2011). For systems with moderate to low amounts of dust, spectroscopic features (such as the relative strengths of Balmer transitions) and continuum color measurements calibrated to extinction curves (e.g., Koornneef & Code 1981; Howarth 1983; Bouchet et al. 1985; Calzetti et al. 1994) can be used to make dust corrections. In very dusty galaxies, the short wavelength light can be completely obscured, resulting in extreme underestimates of the SFR or even non-detections at UV and optical wavelengths.

Since the dust that absorbs the UV and optical photons re-emits that energy at longer wavelengths, observations of dust emission can be used as an alternative measure of SFRs (e.g., Rieke et al. 2009; Calzetti et al. 2010; Hao et al. 2011; Murphy et al. 2011). The total infrared (IR) luminosity, measured as the integrated 3–1100 μm continuum SED that peaks at (rest-frame) far-infrared wavelengths ($\sim 100\,\mu\mathrm{m}$), can be used as one way to measure obscured star formation. Galaxies with some of the highest SFRs have been discovered in surveys at millimeter and submillimeter wavelengths using both space-based facilities like the *Infrared Astronomical Satellite*, the *Spitzer Space Telescope*, and the *Herschel Space Observatory*, and instruments on the ground like the Submillimeter Common Use Bolometer Array (SCUBA; Holland et al. 1999) on the James Clerk Maxwell Telescope (JCMT) and the Max-Planck Millimeter Bolometer (MAMBO; Kreysa et al. 1998) array on the Institut de Radioastronomie Millimétrique (IRAM) 30 meter telescope. These facilities have identified populations of extremely dusty galaxies that are otherwise faint at optical wavelengths, such as ultra/luminous infrared galaxies (LIRGs: $L_{\mathrm{IR}} \gtrsim 10^{11}\,L_{\odot}$; ULIRGs: $L_{\mathrm{IR}} \gtrsim 10^{12}\,L_{\odot}$) at low redshifts (Sanders & Mirabel 1996) and submillimeter galaxies (SMGs) at high

redshifts (Blain et al. 2002; Section 1.2). This method has proved particularly effective at identifying highly obscured star-forming galaxies out to large redshifts; the drop in flux and corresponding change in wavelength caused by shifting the SED out to cosmological distances matches the slope of the Rayleigh-Jeans side of the dust peak, causing $\sim 1\,\mathrm{mm}$ continuum fluxes to be nearly identical for a wide range of redshifts (Figure 1.1). One difficulty with using L_{IR} to measure the SFR is that older stellar populations can also contribute to dust heating, so one must be confident that an observed galaxy is dominated by younger stellar populations when using L_{IR} as a SFR estimator. In addition, the dust in galaxies can also be heated by central active galactic nuclei (AGN), which would produce artificially high SFRs if not properly accounted for in dust SED measurements. At slightly shorter wavelengths, polycyclic aromatic hydrocarbons (PAHs; relatively large molecules that are also found in dusty environments) have a number of vibrational, bending, and stretching modes excited by UV light from stars, but are destroyed in the harder spectra of AGN (e.g., Voit 1992). Therefore, the broad PAH spectral features at ~ 3, 5–9, and 11-14 μm can be used to estimate the SFR without concern for AGN contamination. However, PAH emission depends on metallicity (Z; defined as the mass fraction of elements heavier than helium), making these spectral features poor traces of the SFR for $Z \lesssim 1/3\,Z_{\odot}$ (e.g., Madden 2000; Engelbracht et al. 2005; Calzetti et al. 2007). Since these long wavelength star formation tracers are complementary to UV and optical tracers, care must be taken to correct for stellar emission that is *not* obscured.

Two additional tracers at the short and long wavelength extremes are also used as SFR tracers, although both are bootstrapped to the methods described above (which can be calibrated from first principles using stellar population synthesis models). There is a tight correlation observed between L_{IR} and radio flux at $\nu \sim 1.4\,\mathrm{GHz}$ that allows the radio continuum to be used as star formation tracer (e.g., Murphy et al. 2011). This correlation is caused by synchrotron emission from SN remnants and free-free emission from H II regions at low frequencies, making radio continuum a viable tracer of the most recent epoch of star formation. At the opposite end of the spectrum, X-ray emission at 2–10 keV has been observed to correlate with dust and radio continuum emission, which allows the X-ray flux to be used as a tracer of the SFR (e.g., Ranalli et al. 2003). The X-ray emission (once

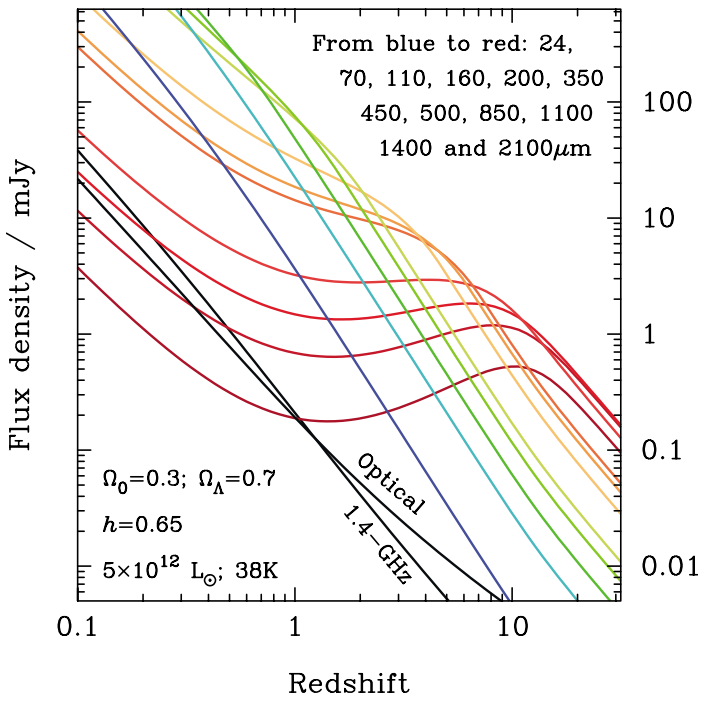

Figure 1.1 The flux density of a dusty galaxy as a function of redshift for several different wavelengths (from Blain et al. 2002). For the 850 μm–2 mm bands, the observed flux density remains relatively constant for $z \sim 1$–10 despite the large luminosity distances.

corrected for potential contributions from AGN accretion disks and X-ray binaries) arises from SNe, SN remnants, and massive stars.

Measurements of the SFR have been observed to correlate strongly with the molecular gas content that fuels the star formation within galaxies (Figure 1.2), which is known as the Schmidt-Kennicutt relation. Correlations between star formation and gas *densities* were first proposed in the theoretical work of Schmidt (1959), but many analyses use star formation and gas properties averaged over the entire galaxy (e.g., Kennicutt 1989; Buat et al. 1989; Kennicutt 1998; Genzel et al. 2010; Daddi et al. 2010; Tacconi et al. 2012) or avoid the additional uncertainties in source size and scaling factors by using the total luminosities of the star formation and gas tracers (e.g., Young et al. 1986; Solomon & Sage 1988; Gao & Solomon 2004). In a few analyses (e.g., Kennicutt et al. 2007; Bigiel et al. 2008, 2010; Wei et al. 2010) resolved maps of SFR and gas mass tracers are used to examine the true *surface density* version of the Schmidt-Kennicutt relation (i.e., compare $\Sigma_{\rm SFR}$ and $\Sigma_{\rm gas}$ on a pixel-by-pixel basis within individual galaxies). The different methods for determining SFRs and gas masses (see Section 1.3 for an introduction to molecular gas

measurements) make it difficult to compare different galaxy studies, leading to significant uncertainties in several characteristics of the Schmidt-Kennicutt relation. While there is a strong correlation between the SFR and gas mass surface densities ($\Sigma_{\rm SFR} \propto \Sigma_{\rm gas}^{n}$) over several orders of magnitude (Figure 1.2), the index (or indices) of the correlation's best-fit power law (n) is debated. The value of the power-law index probes the physical processes responsible for converting gas into stars. A linear correlation would indicate a constant star formation efficiency (or timescale over which all gas would be converted into stars), while super-linear correlations would be expected if star formation depends on collisional processes ($n \approx 2$) or on the free-fall timescale of gravitational collapse for the *total* gas ($n \approx 1.5$; where total means both the molecular and atomic phases of the ISM). Kennicutt & Evans (2012) present a compilation of disk-averaged values, where the star formation and gas mass properties have been calculated in a uniform manner across different galaxy types (including normal disk galaxies and dusty starburst galaxies selected in the IR), and find a power law index of $n \sim 1.4$. However, applying similarly uniform techniques to different tracers of the molecular gas content yields different indices, all $n < 1.5$ (e.g., Gao & Solomon 2004; Narayanan et al. 2005; Graciá-Carpio et al. 2008; Bussmann et al. 2008; Iono et al. 2009; Juneau et al. 2009). These discrepancies are likely due to different molecular gas tracers' being more or less sensitive to different density regimes in the molecular ISM (Krumholz & Thompson 2007; Narayanan et al. 2008, 2011), making the index dependent on the physical conditions of the star-forming gas. In analyses of the resolved star formation properties of nearby disks, a near-unity index for the Schmidt-Kennicutt relation is found in regimes where the molecular gas dominates the total gas mass surface density (e.g., Bigiel et al. 2008, 2010; Schruba et al. 2011). However, in the outermost regions of the disks where neutral gas dominates (and in galaxies entirely dominated by neutral gas), the gas mass surface density is uncorrelated with $\Sigma_{\rm SFR}$, producing an apparent increase in the index below a critical surface density of $\Sigma_{\rm gas} = 9\,M_{\odot}\,{\rm pc}^{-2}$.

At higher gas mass surface densities where a larger number of IR-luminous galaxies are found, there is also some evidence for a different Schmidt-Kennicutt relation. In merger-driven star-forming galaxies, gas masses are typically calculated using a different scaling factor, $\alpha_{\rm CO}$, from that of "normal" galaxies (using the scale factor for normal galaxies

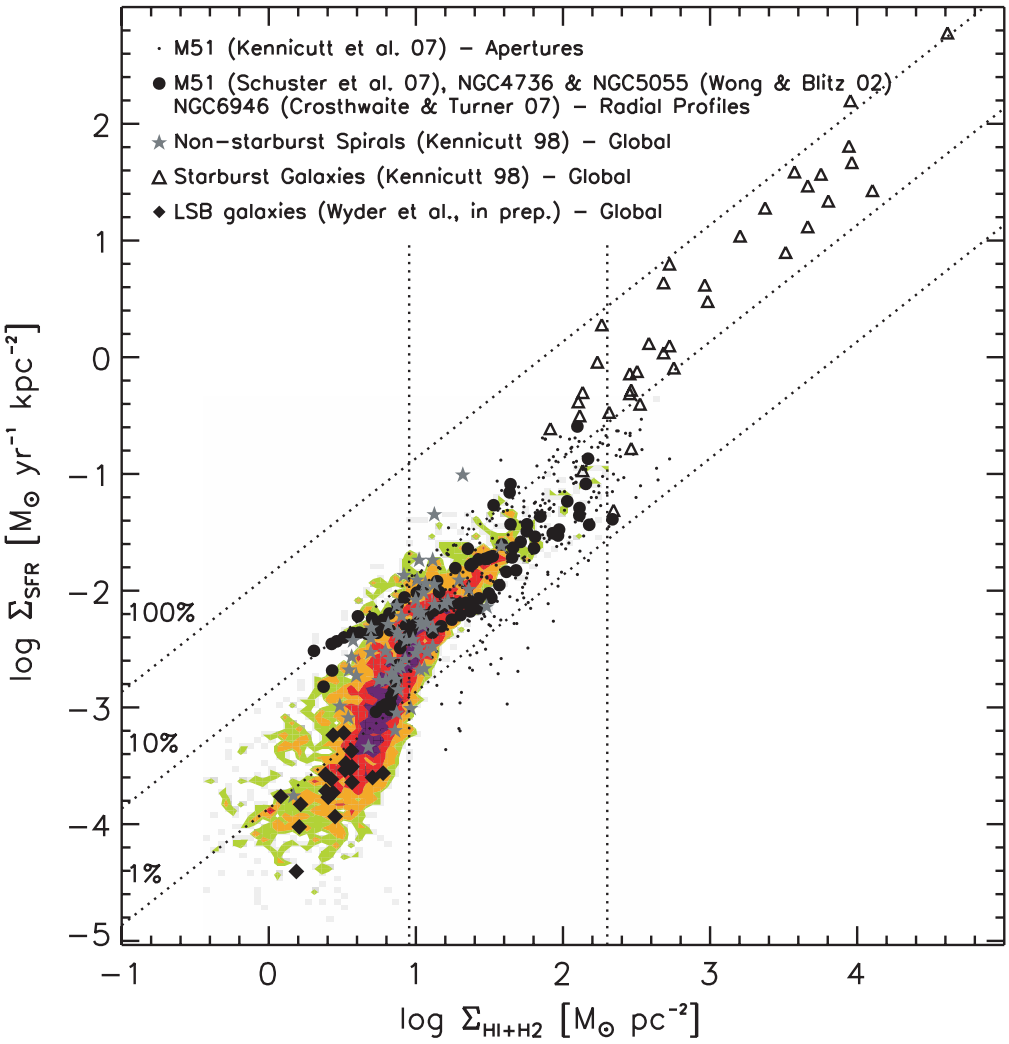

Figure 1.2 Star formation rate surface density vs. gas mass surface density for a collection of local galaxies from Bigiel et al. (2008). The diagonal lines represent the constant star formation efficiencies required to consume 1%, 10%, and 100% of the gas in 10^8 years, the left vertical line shows the HI surface density saturation, and the right vertical line marks a proposed transition between star formation laws at 200 $M_\odot$ pc^{-2}.

produces gas masses larger than the total masses implied by the galaxies' dynamics; see Section 1.3). The resulting horizontal displacement in the $\Sigma_{\rm SFR}$-$\Sigma_{\rm gas}$ plane (relative to normal galaxies) can be interpreted as a second offset star formation law for "starbursts" (see the triangle points in Figure 1.2; e.g., Bigiel et al. 2008; Daddi et al. 2010; Genzel et al. 2010). However, this bimodal star formation relation disappears both when one uses a uniform method of calculating the gas mass, and when one considers the correlation between $\Sigma_{\rm SFR}$ and $\Sigma_{\rm gas}/\tau_{\rm dyn}$ (e.g., Kennicutt 1998; Bouché et al. 2007; Krumholz et al. 2009; Daddi et al. 2010; Genzel et al. 2010), where $\tau_{\rm dyn}$ is a dynamical timescale related to galaxy rotation or the free-fall collapse of gas clouds (e.g., Silk 1997; Elmegreen 2002; Krumholz et al. 2009), suggesting that there is little difference in the fundamental process of star formation between these galaxies.

In addition to the Schmidt-Kennicutt relation, further evidence for different star formation modes has also been seen in measurements of specific SFRs (sSFRs), the SFR divided by the stellar mass. Rodighiero et al. (2011) examine a large sample of $1.5 < z < 2.5$ galaxies that includes a wide range of galaxy types, and find a bimodal distribution in the number of galaxies as a function of the sSFR (although outliers were already known to exist; e.g., Elbaz et al. 2007; Kennicutt & Evans 2012). Further analysis by Sargent et al. (2012) that corrects for the change in mean sSFR as a function of stellar mass clearly identifies two Gaussian peaks in the galaxy distribution, where the class of starburst galaxies has (on average) a four times larger sSFR than "main sequence" normal galaxies (but only represent $\sim 3\%$ of galaxies). These two modes of star formation are proposed to be caused galaxies' dynamical states. Normal galaxies are typically characterized as undisturbed disks, where the star formation is driven by the gravitational collapse of over-densities in the turbulent ISM (e.g., Shu et al. 1987; Li et al. 2005; Krumholz et al. 2005; McKee & Ostriker 2007). In order to produce a starburst, however, a violent event like a major merger is thought to produce increased star formation efficiency as large gravitational torques drive gas into a high-density region in the galaxy's center (e.g., Hernquist 1989; Sanders & Mirabel 1996; Conselice et al. 2003; Narayanan et al. 2010; Engel et al. 2010; Bournaud et al. 2011). Alternative models propose that efficient accretion of gas onto galaxies via filamentary cosmological over-densities can create a starburst without requiring a major merger (e.g., Davé

et al. 2010).

Determining the relative importance of these two star formation modes as function of cosmic history has been somewhat complicated. Observations of multiple star formation tracers suggest that the cosmic SFR density peaked near $z \sim 2$–3 and has declined to the present day (e.g., Madau et al. 1996; Hopkins & Beacom 2006; Reddy & Steidel 2009), making this epoch a crucial period for understanding galaxy evolution. Observationally, starburst galaxies are typically selected for their extreme SFRs observed in infrared tracers. While these U/LIRGs are dominated by major mergers at low redshifts, star formation rates appear to be globally elevated at earlier times, making the distinction between merger-driven starbursts and normal galaxies difficult without additional spatial or kinematic information (e.g., Daddi et al. 2010; Tacconi et al. 2010, 2012; Hayward et al. 2013). Semi-analytic models (SAMs; e.g., Lacey & Silk 1991; White & Frenk 1991), which use cosmological dark matter simulations with general prescriptions for baryonic physics added in post-processing, have been useful for understanding the evolution of galaxy populations statistically (e.g., Granato et al. 2000; Somerville et al. 2001; Balland et al. 2003). Hydrodynamic simulations are too computationally intensive to produce simulations on large enough spatial scales and with enough dynamic range to track the evolution of a significant number of galaxies in adequate detail to capture their baryonic physics. Ideally, SAMs (which are tuned to reproduce the infrared background) would be used to identify which galaxies undergo a starburst and determine their predecessors and descendants. However, SAMs consistently have difficulty reproducing the numbers of high-mass dusty starbursts and their redshift distribution (e.g., Granato et al. 2000; Fontanot et al. 2007; Swinbank et al. 2008; Niemi et al. 2012; Somerville et al. 2012) without resorting to top-heavy IMFs (Baugh et al. 2005; Lacey et al. 2008), non-standard cosmologies (Guiderdoni et al. 1998; Devriendt & Guiderdoni 2000), or other extremes (e.g., Blain et al. 1999; Kaviani et al. 2003; although see recent improvements by Hayward et al. 2013).

In order to better understand star formation in the $z \sim 2$ epoch of galaxy evolution, for my dissertation, I have worked on characterizing the molecular gas that fuels extreme SFRs in high-redshift dusty galaxies. In the remaining sections of the introduction, I describe

the population of dusty galaxies from which the sources I study are (largely) drawn (Section 1.2) and how observations of the molecular gas are used to understand these galaxies (Section 1.3). Finally, in Section 1.4, I describe a few of the open questions about molecular gas in high-redshift star-forming galaxies that I address in my dissertation.

1.2 Submillimeter Galaxies

On the heels of the discovery of the cosmic microwave background (CMB), early theories of galaxy evolution predicted the existence of an infrared background caused by the redshifted light from galaxies in the early universe (e.g., Partridge & Peebles 1967; Low & Tucker 1968). The existence of the infrared background was not confirmed until observations were made using the Far-infrared Absolute Spectrophotometer (FIRAS) instrument on the *Cosmic Background Explorer* (*COBE*; Puget et al. 1996; Fixsen et al. 1998; Lagache et al. 1999), which spurred an effort to identify the source(s) of the FIR and submillimeter background (which is now known to contain nearly half of the energy from star formation; e.g., Fixsen et al. 1998; Barger et al. 1999; Takeuchi et al. 2005; Hopkins & Beacom 2006). Surveys at millimeter and submillimeter wavelengths using SCUBA on the JCMT and MAMBO on the IRAM 30 m telescope (largely) targeted galaxy clusters in order to leverage their gravitational lensing magnification to boost the observed flux from the high-redshift galaxies that produce the infrared background (e.g., Smail et al. 1997; Barger et al. 1998; Hughes et al. 1998; Bertoldi et al. 2000). These surveys discovered a surprisingly large number of submillimeter-bright ($S_{850\,\mu\mathrm{m}} \gtrsim 5\,\mathrm{mJy}$) star-forming galaxies, now termed submillimeter galaxies (SMGs; see review article by Blain et al. 2002).

Further characterization of the population of SMGs was made difficult by the poor spatial resolution of the bolometer arrays ($\sim 7.5''$–$15''$, depending on the observing wavelength), making it hard to identify counterparts to SMGs at other wavelengths where observations have significantly higher resolution. Multi-wavelength identifications initially relied on the FIR-radio correlation; a better-resolved source in a deep high-resolution 21 cm map near the submillimeter centroid position would be used to identify an SMG's location, which would be used as the position for optical and near-IR spectroscopy measurements of the SMG's redshift (e.g., Chapman et al. 2005). While this method leads to some selection effects (the

highest redshift sources may not be detected in the radio, and the most obscured galaxies may not have optical counterparts), the original redshift distribution in Chapman et al. (2005) has been verified using other samples of dusty galaxies (e.g., Chapin et al. 2009; Wardlow et al. 2011; Yun et al. 2012), including samples that do not depend on these pre-selection techniques (e.g., Harris et al. 2012). The peak of the SMG redshift distribution appears to be at $z \sim 2.2$, near the epoch of peak cosmic SFR density, with a tail out to larger redshifts (e.g., Vieira et al. 2013). SMGs' large FIR luminosities ($\gtrsim 10^{12}\,L_{\odot}$) and implied extreme SFRs ($\gtrsim 100\,M_{\odot}\,\mathrm{yr}^{-1}$) indicate that a substantial fraction of the infrared background is produced by dusty galaxies at $z \gtrsim 1$ (e.g., Devlin et al. 2009; Le Floc'h et al. 2009; Domínguez et al. 2011; Béthermin et al. 2012; Gilmore et al. 2012).

At similar redshifts of $z \sim 2$–3, AGN are also common (e.g., Cowie et al. 2003; La Franca et al. 2005; Bongiorno et al. 2007); since the host galaxies of AGN can also have centrally concentrated star formation and large dust contents (e.g., Rowan-Robinson 1995; Barvainis & Ivison 2002; Netzer et al. 2007; Lutz et al. 2008), potentially due to an evolutionary connection between the two populations (e.g. Granato et al. 2001; Somerville et al. 2008; Bonfield et al. 2011), accurately characterizing SMGs' star formation properties requires disentangling the potential contribution of dust heating by the central AGN to the FIR luminosity. The faintness of SMGs' X-ray counterparts (Alexander et al. 2003) and the presence of PAH emission features atop an otherwise weak mid-infrared continuum (e.g., Lutz et al. 2005; Valiante et al. 2007; Menéndez-Delmestre et al. 2009) indicate that most of SMGs' luminosity is likely due to star formation rather than obscured AGN (although this is not true for all SMGs; Coppin et al. 2010). Given SMGs' large SFRs, dust contents, and the large halo and/or baryonic masses seen in both observational and theoretical studies (e.g., Genzel et al. 2003; Blain et al. 2004; Tecza et al. 2004; Swinbank et al. 2008; Ivison et al. 2010; Hainline et al. 2011), SMGs appear to be "scaled-up" versions of the local population of U/LIRGs (i.e., more massive, more luminous, etc.; Sanders & Mirabel 1996; Tacconi et al. 2006). Since U/LIRGs in the local universe appear to be major mergers of gas-rich galaxies, SMGs are largely believed to be the predecessors of present-day elliptical galaxies caught in their merger-driven starburst formation phase (e.g., Conselice et al. 2003; Thomas et al. 2005; Narayanan et al. 2005; Engel et al. 2010). However, some cosmological

simulations suggest that high SFRs are not necessarily caused by major mergers, and the smooth infall of gas along filamentary over-densities (Davé et al. 2010) and globally elevated gas mass fractions at high redshifts can create submillimeter-bright galaxies. Therefore, selecting high-redshift submillimeter-bright systems picks out mostly disk galaxies (including unresolved galaxy pairs that are not necessarily mergers; Hayward et al. 2011), and only a relatively small fraction ($\sim 15\%$) at the brightest end of the luminosity distribution are actually major mergers (Hayward et al. 2013). These predictions are in line with recent high-resolution observations of SMGs' gas distributions and kinematics that indicate SMGs are a diverse population of galaxies, which includes at least some disks (e.g., Swinbank et al. 2011; Hodge et al. 2012).

1.3 Molecular Gas

Determining the starburst nature and evolutionary state of SMGs and other galaxies requires understanding the molecular gas that fuels star formation.

In the highest density regions of the ISM ($n > 100$ cm^{-3}), molecular hydrogen (H_2) efficiently forms on the surfaces of dust grains (for sufficiently metal-rich environments). These dusty molecular gas clouds are self-shielding, which prevents dissociation of molecular species by interstellar radiation. Molecular clouds in galaxies such as the Milky Way are gravitationally bound objects that have a wide range of sizes, and can contain densities in their cores in excess of 10^4–10^6 cm^{-3}. In the densest regions of molecular clouds, the gas gravitationally collapses to form stars. Even though H_2 is the most abundant molecular species by a factor of $\sim 10^4$–10^5, it is not a strong emitter in the physical conditions typically found in the bulk of molecular clouds; the rotational transitions are forbidden, and the vibration-rotation lines occur only in extreme environments such as shock fronts or near sources of hard UV emission.

Carbon monoxide (CO) is one of the best tracers of the molecular ISM; it is the second most abundant molecule and is not easily destroyed by the UV radiation of young stars. In addition, CO's strong electric dipole moment results in a series of rotational transitions (between levels quantized by the letter J) that are easily excited by collisions with H_2 and

helium at typical molecular cloud temperatures (a few tens of Kelvin) and densities. The relative strengths of the CO rotational transitions (whose frequencies are integer multiples of $\sim 115\,\mathrm{GHz}$) can be used to determine the gas conditions, since the higher frequency lines require higher temperatures and larger densities for the CO to be collisionally excited to those levels. For optically thick thermalized CO emission, the brightness temperature (or the integrated line luminosity in units of brightness temperature, L'; Solomon & Vanden Bout 2005), are independent of rotational transition (i.e., $L'_{\mathrm{CO(3–2)}} = L'_{\mathrm{CO(1–0)}}$ for $n_{\mathrm{H_2}} \gg n_{\mathrm{crit,CO(1–0)}}$ and $n_{\mathrm{crit,CO(3–2)}}$, where the critical density, n_{crit}, is defined as the ratio of the spontaneous emission rate and collisional de-excitation rate per collider density). In order to probe gas conditions that the CO rotational lines are not sensitive to, other species have been used as gas tracers, such as rotational HCN lines in high-density regions and C I fine structure lines for the outer regions of clouds where there is insufficient CO to self-shield.

Under the assumption of non-overlapping virialized molecular clouds, Dickman et al. (1986) showed that the integrated CO brightness temperature is directly proportional to the total molecular gas mass. The proportionality constant, α_{CO}, has been measured through several independent methods for the Milky Way (Dickman 1978; Bloemen et al. 1986; Solomon et al. 1987; Strong et al. 1988), which has resulted in a consensus value of $\alpha_{\mathrm{CO}} = M_{\mathrm{H_2}}/L'_{\mathrm{CO}} = 4.6\,M_\odot\,(\mathrm{K\,km\,s^{-1}\,pc^2})^{-1}$. Even though the conversion was found to be consistent with local galaxies in which giant molecular clouds could be resolved (summarized in Young & Scoville 1991), application of this value to local U/LIRGs and some disk galaxy centers results in high, and sometimes unphysical, gas mass fractions (e.g., Scoville et al. 1991; Garcia-Burillo et al. 1993; Downes et al. 1993; Solomon et al. 1997; Scoville et al. 1997; Oka et al. 1998; Hinz & Rieke 2006; Meier et al. 2010). An alternative model was developed for major mergers (like U/LIRGs) that assumed the molecular gas fills the potential well of the galaxy instead of being contained in individual gravitationally bound clouds (Downes et al. 1993). Under this assumption, a combination of kinematic and radiative transfer models yields an effective conversion factor for U/LIRGs of $\alpha_{\mathrm{CO}} = 0.8\,M_\odot\,(\mathrm{K\ km\ s^{-1}\,pc^2})^{-1}$ (Downes & Solomon 1998; see also Scoville et al. 1997). At high redshifts where obtaining resolved maps of the molecular gas and its dynamics is difficult (Solomon & Vanden Bout 2005), the application of the CO-to-$\mathrm{H_2}$ conversion factor is

largely bimodal, leading to the adoption of a "disk" value ($\alpha_{\rm CO} = 4.6\,M_\odot\,(\rm K\,km\,s^{-1}\,pc^2)^{-1}$) for normal star-forming galaxies and a "starburst" value ($\alpha_{\rm CO} = 0.8\,M_\odot\,(\rm K\,km\,s^{-1}\,pc^2)^{-1}$) for mergers and other high surface density environments. Some effort has been made to find a suitable continuous form of $\alpha_{\rm CO}$ (e.g., Glover & Mac Low 2011; Narayanan et al. 2012) that also matches observed trends in metallicity (the CO-to-H_2 conversion factor may decrease with increased metallicity; e.g., Wilson 1995; Arimoto et al. 1996; Israel 1997; Leroy et al. 2006; Bolatto et al. 2008; Genzel et al. 2012).

In addition to the integrated line strength determining the molecular gas mass, the velocity sensitivity of spectral lines provides kinematic information about galaxies and their molecular gas. For well-resolved disks, molecular emission can be used to trace out rotation curves, which probe the dynamical (total) masses of galaxies. By removing the global velocity gradients caused by rotation, the velocity dispersion of the molecular gas measures the turbulence within the molecular clouds (or *of* the molecular clouds if there is significant random motion on large scales). If the galaxy is not resolved, the line width and shape can be used to estimate the total mass for the assumption of rotating disk-like kinematics or dispersion-dominated kinematics. However, the double peaked line profile one would expect from rotating galaxies can also be created in a merger where the two colliding galaxies are slightly offset in velocity, making the interpretation of line profiles for unresolved galaxies difficult (as is the case for many high redshift systems).

Since the different CO rotational lines are more or less luminous depending on the physical conditions of the molecular gas, these line ratios can be used to determine the gas excitation. The line ratio, $r_{J,J'}$, is the ratio of the integrated brightness temperature of the CO($J \rightarrow J-1$) line to that of the CO($J' \rightarrow J'-1$) line:

$$\begin{aligned} r_{J,J'} &= \frac{\int T_B(J \rightarrow J-1)dv}{\int T_B(J' \rightarrow J'-1)dv} \\ &= \frac{\int S_\nu(J \rightarrow J-1)dv}{\int S_\nu(J' \rightarrow J'-1)dv} \left(\frac{\nu_{J' \rightarrow J'-1}}{\nu_{J \rightarrow J-1}}\right)^2 \\ &= \frac{L'_{J \rightarrow J-1}}{L'_{J' \rightarrow J'-1}}. \end{aligned} \tag{1.1}$$

Since the integrated line luminosities for two transitions should be equal if the lines are optically thick and thermalized, line ratios that differ from unity indicate either multiple phases of molecular gas (i.e., multiple temperatures and densities) or subthermal gas excitation (e.g., Downes & Solomon 1998; Aravena et al. 2010). Since strong CO(1–0) emission requires relatively low temperatures and densities ($T_{\rm kin} \gtrsim 5\,{\rm K}$ and $n_{\rm H_2} \gtrsim 10^3, {\rm cm}^{-3}$) compared to CO(3–2) emission ($T_{\rm kin} \gtrsim 30\,{\rm K}$ and $n_{\rm H_2} \gtrsim 10^4, {\rm cm}^{-3}$), $r_{3,1}$ is a useful probe of the relative fractions of cold quiescent molecular gas and warm gas that is more likely involved in star formation. Near-unity values of $r_{3,1}$ suggest that molecular ISM has temperatures and densities that are at least sufficient to excite CO(3–2) (i.e., $T_{\rm kin} \gtrsim 30\,{\rm K}$ and $n_{\rm H_2} \gtrsim 10^4, {\rm cm}^{-3}$). Sub-unity values of $r_{3,1}$ either indicate the gas is subthermally excited (i.e., the gas temperatures and densities are too low to excite a significant fraction of CO to the $J = 3$ level) or the gas has a mixture of excitation conditions (where some gas strongly emits in higher-J lines and some gas does not).

While early studies of the molecular gas in high-redshift star-forming galaxies used solely mid-J CO lines (i.e., CO(3–2), CO(4–3), and CO(5–4)) and produced line ratios consistent with a single phase of gas (e.g., Weiß et al. 2007), recent expansions of radio telescopes' frequency coverage into the Ka band (26.5–40 GHz) have allowed observations of CO(1–0) for SMGs whose redshifts fall near the $z \sim 2$–3 peak of the redshift distribution (building on CO(1–0) detections of other $z > 1$ populations in other bands; e.g., Papadopoulos et al. 2001; Carilli et al. 2002; Greve et al. 2003, 2004; Klamer et al. 2005; Hainline et al. 2006; Riechers et al. 2006; Dannerbauer et al. 2009; Carilli et al. 2010; Aravena et al. 2010). Observations have shown that SMGs favor CO(3–2) to CO(1–0) line ratios of $r_{3,1} \sim 0.6$ (Table 1.1). Since subthermal excitation is inconsistent with observed high-J CO emission (i.e., if the temperature and density is low enough to produce only weak CO(3–2) emission, there should be *even less* CO(7–6) emission), these line ratios indicate the presence of a multi-phase molecular ISM that includes a substantial cold gas reservoir (Swinbank et al. 2010b; Harris et al. 2010; Ivison et al. 2011; Danielson et al. 2011). While similar line ratios have been observed in other types of high-redshift star-forming systems like Lyman break galaxies (Riechers et al. 2010) and BzK-selected galaxies (Dannerbauer et al. 2009; Aravena et al. 2010), and in low-redshift dusty galaxies (albeit with a much wider range of $r_{3,1}$; e.g.,

Table 1.1. Summary of High Redshift $r_{3,1}$ Measurements

Population	$\overline{X}_{\rm w}$[a]	σ	N[b]	Range
SMGs	0.64	0.08	6	0.54–0.75
Quasar-host	1.05	0.05	4	0.93–1.06
LBGs	0.74	0.04	2	0.72–0.78
BzKs	$0.61^{+0.39}_{-0.26}$	...	1	...
Excluded[c]	...	...	4	0.37–1.14

[a]Weighted mean; for the BzK-selected galaxy the measured value is given.

[b]Number of sources with measured $r_{3,1}$.

[c]Sources with uncertain classifications.

Note. — Includes only sources with *measured* values of $r_{3,1}$ and excludes sources from this thesis (Swinbank et al. 2010b; Harris et al. 2010; Riechers et al. 2010; Danielson et al. 2011; Ivison et al. 2011; Riechers et al. 2011c,b,a; Thomson et al. 2012).

Mauersberger et al. 1999; Yao et al. 2003), this result is in direct contrast to those for quasar host galaxies, whose near-unity value of $r_{3,1}$ is consistent with single-phase molecular gas (Riechers et al. 2006, 2011a; though the comparison is based on the relatively small number of measurements listed in Table 1.1). These low $r_{3,1}$ values indicate that a substantial gas component is undetected in mid-J observations, and that gas masses in SMGs have been underestimated by at least a factor of ~ 1.5 (Harris et al. 2010).

More details about the gas physical conditions can be obtained from the analysis of the full CO spectral line energy distribution (SLED; e.g., Wild et al. 1992; Guesten et al. 1993; Mao et al. 2000; Ward et al. 2003; Weiß et al. 2005b, 2007), the velocity-integrated line flux as a function of rotational quantum number (which is often normalized to the $J = 1-0$ flux). Comparing the peak of the CO SLED for different galaxies probes the relative excitation of the sources, where the SLED peak for more excited (higher temperature and density) gas is at larger J. For local disk galaxies, including the Milky Way, the CO SLED peaks

near $J_{\rm upper} \sim 2$–3. Mergers and other U/LIRGs tend to have hotter and denser molecular gas, resulting in a CO SLED peak at $J_{\rm upper} \sim 3$–4. High redshift U/LIRGs, like SMGs, peak at even larger values of $J_{\rm upper} \sim 5$–6. The relative excitation increases even further for galaxies hosting AGN, whose CO SLEDs peak anywhere from $J_{\rm upper} \sim 6$–10.

The CO SLED can be used to constrain the gas temperature and density by fitting the observed line ratios to a radiative transfer model. Since the emission from molecular clouds is optically thick, full radiative transfer modeling is difficult; photons emitted in one region of the cloud (or galaxy) can scatter to affect other regions, which would impose the computationally intense problem of iteratively solving the rate balance equations for each location in the medium. A popular way of simplifying the calculation is to assume a large velocity gradient (LVG; Goldreich & Kwan 1974; Scoville & Solomon 1974; Ward 2002; van der Tak et al. 2007), where gas flows along the line of sight (~ 1–$10\,{\rm km\,s^{-1}}$ for individual molecular clouds) are larger than the local random thermal velocities ($\sim 0.1\,{\rm km\,s^{-1}}$). In this approximation, the relative velocities of the gas make individual regions transparent to emission from other regions due to their relative Doppler shifts, making the radiative transfer analysis a purely local problem (i.e., the LVG simplifies the calculation of the line optical depth). In LVG models, the kinematic temperature, H_2 density, and CO column length per unit line width (or sometimes the CO abundance per unit velocity gradient; which parameterizes the LVG in the eponymous model) are varied to determine which values of these physical condition parameters best reproduce the measured line ratios in the CO SLED. In the case of a multi-phase molecular ISM, the line ratios from multiple models can be combined together with an additional factor that parameterizes the fraction of the molecular gas in each phase. A detailed description of the LVG modeling, computational method, and method of comparison to measured line ratios used in this work is given in Chapter 2.4.2 and Appendix B.

1.4 Open Questions

A significant effort has been made to characterize the molecular gas that fuels the rapid star formation observed in dusty galaxies at high redshifts (e.g., Frayer et al. 1998, 1999; Neri et al. 2003; Greve et al. 2005; Tacconi et al. 2006, 2008). A small but growing number

of IR-luminous $z > 2$ galaxies now have sets of measured CO line fluxes that are complete from low to high J, which has resulted in a clearer picture of the multi-phase nature of the molecular gas in SMGs. However, the lack of high resolution observations leaves some margin for error in interpreting the observed line ratios and fails to address the debate on SMGs' dynamical state relative to other high-redshift star-forming populations.

High-resolution observations are necessary if we are to be confident in assessing gas physical conditions. Analysis of line ratios assumes that the CO lines are being emitted from the same localized regions. Given the clumpy structure observed in SMGs (e.g., Tacconi et al. 2008; Swinbank et al. 2010b), and the role major mergers are likely playing in the star formation bursts of (at least) some of these systems (e.g., Conselice et al. 2003; Narayanan et al. 2010; Engel et al. 2010; Davé et al. 2010), it is not safe to assume a homogenous distribution of gas conditions within every galaxy (e.g., Mao et al. 2000; Zhu et al. 2003). In addition, since many of the well-studied SMGs are gravitationally lensed, it is possible that differential lensing (the variation in magnification factor across a spatially extended source with regional differences in emission at different wavelengths) could be affecting the observed line ratios (e.g., Blain 1999; Serjeant 2012). Indirect evidence for the spatial variation of excitation in SMGs has been seen in the more extended distribution of CO(1–0) relative to radio continuum emission (from the synchrotron radiation from SN remnants and free-free emission from H II regions, which trace more actively star-forming and higher-excitation gas; Ivison et al. 2011). Evidence for the larger spatial extent of SMGs' cold gas reservoirs is also bolstered by the larger line widths of CO(1–0) vs. CO(3–2) (Ivison et al. 2011; Thomson et al. 2012).

The high-resolution observations necessary for determining spatial distributions of excitation conditions are also important for determining the dynamical state of SMGs and other high-redshift galaxies. While the picture of submillimeter-selected galaxies as major merger driven starbursts is based on similarities to U/LIRGs in the local universe and the clumpy morphologies observed in several systems (e.g., Tacconi et al. 2006, 2008), recent observational and theoretical work seems to indicate that a substantial fraction of IR-luminous star-forming galaxies at $z \sim 2$ may not be mergers (e.g., Hayward et al. 2011; Hodge et al. 2012). Unresolved CO observations are insufficient to distinguish between mergers and

disks, as both can result in double-peaked line profiles, and in dusty systems, optical/near-IR morphologies can appear clumpy due to obscuration (e.g., Smail et al. 2004; Swinbank et al. 2010a; Alaghband-Zadeh et al. 2012). In addition to resolved kinematics, differing excitation conditions can also be helpful for distinguishing between clumpy/obscured disks and mergers; if velocity components are physically associated with one another, it is unlikely that they will have vastly different excitation conditions.

High-resolution CO observations are also important for evaluating where SMGs fall on the true surface density version of the Schmidt-Kennicutt relation (e.g., Kennicutt et al. 2007; Bigiel et al. 2008; Wei et al. 2010). Comparisons between the Schmidt-Kennicutt relations for high- and low-redshift galaxies may be affected by the different CO lines observed (Narayanan et al. 2011); the molecular gas in local galaxies is measured via the CO(1–0) line, while the molecular gas at high redshift has typically been measured via mid-J CO lines. In addition, at high redshift, observations of the molecular gas and star formation tracers are largely unresolved, restricting analyses of the Schmidt-Kennicutt relation to globally averaged values of the surface densities. Resolved multi-J CO mapping will not only help with comparisons of different excitation gas tracers and more accurate surface density measurements, but it will also help determine which value (or values) of $\alpha_{\rm CO}$ is appropriate for high-redshift galaxies (e.g., Tacconi et al. 2008; Narayanan et al. 2012). Resolving the distribution of the molecular gas (whether this be individual virialized clouds, a continuous distribution of gas that fills the gravitational potential, or something in between) and determining the gas physical conditions (like global and/or local velocity gradients) will help us better constrain gas masses and thus the value of $\alpha_{\rm CO}$. More accurate gas masses will help resolve the apparent bimodality in the high-redshift Schmidt-Kennicutt relation (where SMGs fall along the low-redshift starburst track, and more "normal" high-redshift galaxies extend the low-redshift disk galaxy track to higher masses and SFRs; e.g., Daddi et al. 2010; Genzel et al. 2010; cf. Ivison et al. 2011) as either an artifact of bimodal choices of $\alpha_{\rm CO}$ or a real feature caused by a burst mode of star formation.

For my thesis, I have obtained high-resolution CO mapping of three high-redshift dusty galaxies in order to help address these issues. In Chapter 2, I present results from multi-J mapping of the SMG SMM J00266+1708, which indicate that the source is a merger whose

two components have different gas conditions and dynamics. In Chapter 3, I discuss high-resolution CO(1–0) mapping of the SMG SMM J14011+0252, which I compare to Hα data in order to derive a resolved Schmidt-Kennicutt relation for this source. In Chapter 4, I present CO(1–0) and CO(3–2) mapping of a strongly lensed disk galaxy, SDSS J0901+1814, which was initially selected in the UV but is also a bright submillimeter source. I conclude in Chapter 5, where I also discuss how these three sources affect our understanding of high-redshift dusty galaxies. Additional information describing the basic calculations performed and the details of the LVG modeling can be found in the Appendices.

In order to calculate physical source sizes and distances for the high-redshift galaxies in this thesis, I must assume a specific cosmology. I adopt the concordance cosmology where the sum of the (present-day) dominant energy density components of the universe, matter (both baryonic matter and cold dark matter, $\Omega_{\rm m}$) and dark energy (Ω_Λ), are sufficient for the universe to be spatially flat ($\Omega_{\rm m} + \Omega_\Lambda = 1$; i.e., ΛCDM). Cosmological parameters have been constrained by a number of observational methods, including fits to the angular power spectrum of fluctuations in the CMB, measurements of the sound horizon from two-point correlations in the spatial distribution of galaxies (i.e., baryonic acoustic oscillations; BAO), and SNe measurements of the expansion rate of the universe (H_0). Throughout this work I assume the flat WMAP7+BAO+H_0 mean ΛCDM cosmology from Komatsu et al. (2011), with $\Omega_\Lambda = 0.725$ and $H_0 = 70.2\,{\rm km\,s^{-1}\,Mpc^{-1}}$.

Chapter 2

SMM J00266+1708

2.1 Background

In this chapter we report observations of a SMG, SMM J00266+1708 (J00266 hereafter), whose multiple components have line ratios differing from the standard $r_{3,1} \sim 0.6$. J00266 is the second brightest SMG in the SCUBA Lens Survey (Smail et al. 2002) and has unusually high obscuration: it is the faintest of the detected SMGs in Frayer et al. (2004), with $K = 22.36 \pm 0.16$ and $J > 24.27$. Difficulties in counterpart identification led to an incorrect initial redshift (Frayer et al. 2000). However, Valiante et al. (2007) identified strong PAH emission features using the *Spitzer Space Telescope* and estimated the source's redshift to be $z_{\rm PAH} = 2.73 \pm 0.02$. Based on this estimate, we observed J00266 with the Zpectrometer (Harris et al. 2007) on the Robert C. Byrd Green Bank Telescope (GBT) and successfully detected the CO(1–0) line at $z_{\rm CO} = 2.742$. We then used this more precise redshift to make interferometric observations of CO(1–0) at the Karl G. Jansky Very Large Array (VLA), CO(3–2) and CO(5–4) at the IRAM Plateau de Bure Interferometer (PdBI), and CO(7–6) at the Submillimeter Array (SMA).

2.2 Observations

2.2.1 Robert C. Byrd Green Bank Telescope

J00266 was observed at the GBT on 2007 November 8, 9, 19, 25, 28, and 29, and on 2008 March 6, using the Zpectrometer (Harris et al. 2007). The Zpectrometer is a fixed-bandwidth instrument covering a $25.6 - 36\,{\rm GHz}$ range within the Ka band that allows for blind detections of the CO(1–0) line for sources with $2.2 < z < 3.5$. Observations were carried out with the standard combination of position switching and sub-reflector nodding

described in Harris et al. (2010), using SMM J00265+1710 (Smail et al. 2002) as a position-switching "partner." We observed 3C48 for flux calibration, and processed the spectrum using a custom set of GBTIDL and R scripts. We measure $z_{\rm GBT} = 2.74189 \pm 0.00065$ for the CO(1–0) line centroid, which we use as the reference velocity for analysis of the other CO observations.

2.2.2 Plateau de Bure Interferometer

CO(3–2) and CO(5–4) emission from J00266 was observed at the PdBI (Guilloteau et al. 1992). The CO(3–2) line was observed on 2009 October 25 with the array in a five-antenna version of the C configuration (with a maximum baseline of 144.5 m) and on 2011 January 20 and 31 with the full A configuration array (maximum baseline of 760 m), all in excellent weather conditions. The CO(5–4) line was observed on 2010 May 15, also with excellent weather conditions, but with the full array in the D configuration (maximum baseline 97.0 m). For all observations we used the narrow-band correlator mode with 5 MHz channels and a total bandwidth of 1 GHz, obtaining both horizontal and vertical polarizations. For the CO(3–2) line, the correlator was tuned to 92.707 GHz for the 2009 observations and to 92.505 GHz for the 2011 observations (the change in tuning was informed by the line profile of the earlier observations). For the CO(5–4) observations, the correlator was tuned to 154.104 GHz. The CO(3–2) and CO(5–4) lines of J00266 were observed for 10.5 hours in the 3 mm band and 7.7 hours in the 2 mm band, respectively.

Bandpass and flux calibration was carried out using MWC 349 or 3C454.3 near the beginning of each observing session. Phase and amplitude variation were tracked by alternating observations of the target with nearby bright quasars. Calibration and flagging for data quality were carried out using the CLIC program (part of the IRAM GILDAS package; Guilloteau & Lucas 2000). The resulting *uv* datasets were smoothed by factors of three and four, resulting in 48.66 km s^{-1} and 38.96 km s^{-1} spectral resolution, for the CO(3–2) and CO(5–4) observations respectively. The GILDAS package was also used to produce the naturally weighted maps, with synthesized beams of $1''.36 \times 0''.81$ at position angle 31.07° for the CO(3–2) observations and $3''.70 \times 3''.04$ at position angle 120.24° for the CO(5–4) observations. The average RMS noise per channel of the CO(3–2) observation

is $0.323\,\mathrm{mJy\,beam^{-1}}$, and is $0.715\,\mathrm{mJy\,beam^{-1}}$ for the CO(5–4) observations. Analysis of the resulting data cubes used a custom set of IDL scripts.

2.2.3 Submillimeter Array

We observed the CO(7–6) line in J00266 at the SMA on 2010 October 3 and 21, with good and excellent weather conditions, respectively. The tracks were both taken with the array in its compact configuration (maximum baseline of 78 m) using seven antennas, and together resulted in a total of 14.1 hours on source. The correlator was in the standard mode to deliver the maximum bandwidth (4 GHz per sideband) for single-receiver observations, giving a channel width of 812.5 kHz. The correlator was tuned to 215.567 GHz at "chunk s14" so that the CO(7–6) line would fall in the upper sideband, well away from the sideband's edges and the sideband's 32 MHz coverage gap between the two intermediate frequency (IF) bands.

Flux calibration used Uranus or Neptune. Phase and amplitude variation were tracked by alternating observations of the target with several nearby bright quasars, which were also used for bandpass calibration. The initial system temperature correction was carried out using the MIR package[1], but all other calibration and mapping were done in CASA[2]. The calibrated data were re-binned into $100\,\mathrm{km\,s^{-1}}$ channels, and the resulting naturally weighted map has a synthesized beam of $3''.44 \times 3''.03$ at a position angle of 73.23° and an RMS noise of $3.8\,\mathrm{mJy\,beam^{-1}}$ in each channel. Analysis of the resulting data cube used the same custom set of IDL scripts as the PdBI observations.

2.2.4 Karl G. Jansky Very Large Array

To complement our GBT detection, the CO(1–0) line was observed at the VLA on 2010 November 6 in excellent weather conditions. A single track was taken with the array in the C configuration (maximum baseline 3.4 km) using 19 antennas, which resulted in a total of 3.24 hours on source. We observed with the Wideband Interferometric Digital Architecture (WIDAR) correlator tuned to 30.8047 GHz in "Open Shared Risk Observing 2 (OSRO2)

[1] https://www.cfa.harvard.edu/∼cqi/mircook.html
[2] http://casa.nrao.edu

1 Subband/Dual polarization" mode, using the lowest available spectral resolution (256 channels at 500 kHz resolution).

Flux calibration used the quasar 3C48. Phase and amplitude calibration relied on interleaved observations of the nearby quasar J0056+1625. Calibration and mapping were carried out in CASA. While these data did not have sufficient S/N for detection of the full line profile of CO(1–0) in J00266, we were able to detect the source by integrating over the $-625 \rightarrow 275\,\mathrm{km\,s^{-1}}$ velocity range (relative to z_{GBT}) given by the mid-J spectra. The integrated line map has a synthesized beam of $0''.78 \times 0''.74$ at position angle 3.0°, and RMS noise of $31.5\,\mathrm{mJy\,km\,s^{-1}\,beam^{-1}}$.

2.3 Results

We have successfully detected the CO(1–0) line with the GBT/Zpectrometer, and both CO(3–2) and CO(5–4) lines at the PdBI. The CO(1–0) observations at the VLA resulted in only a weak detection in the integrated line map, and J00266 was undetected in CO(7–6) at the SMA. In addition, the position-switching partner for the GBT/Zpectrometer observations, SMM J00265+1710, was not detected in CO(1–0). The integrated line maps for the interferometric observations of J00266 are shown in Figure 2.1, plotted relative to the Frayer et al. (2000) continuum detection. For the CO(1–0) and CO(7–6) line maps, we integrate over the $-625 \rightarrow 275\,\mathrm{km\,s^{-1}}$ velocity range relative to z_{GBT} that best matches the FWZI of the CO(3–2) and CO(5–4) lines. For the PdBI maps, the CO(3–2) emission is resolved, but the CO(5–4) emission is not. An elliptical Gaussian fit to the CO(3–2) uv data gives a major axis of $1.''40 \pm 0.''11$ at position angle -59 ± 9 degrees and a minor axis of $0''.91 \pm 0''.11$.

The PdBI spectra of the mid-J lines and the GBT/Zpectrometer spectrum of CO(1–0) for J00266 are shown in Figure 2.2 relative to the rest-frame velocity determined by the initial GBT/Zpectrometer detection. J00266 has a clear double-peaked structure in both mid-J lines that is not seen in the GBT spectrum; it appears that the GBT/Zpectrometer detected the CO(1–0) line in only the redder of the two peaks, with an integrated line flux of $0.380 \pm 0.074\,\mathrm{Jy\,km\,s^{-1}}$. While we have not spectrally resolved the CO(1–0) line

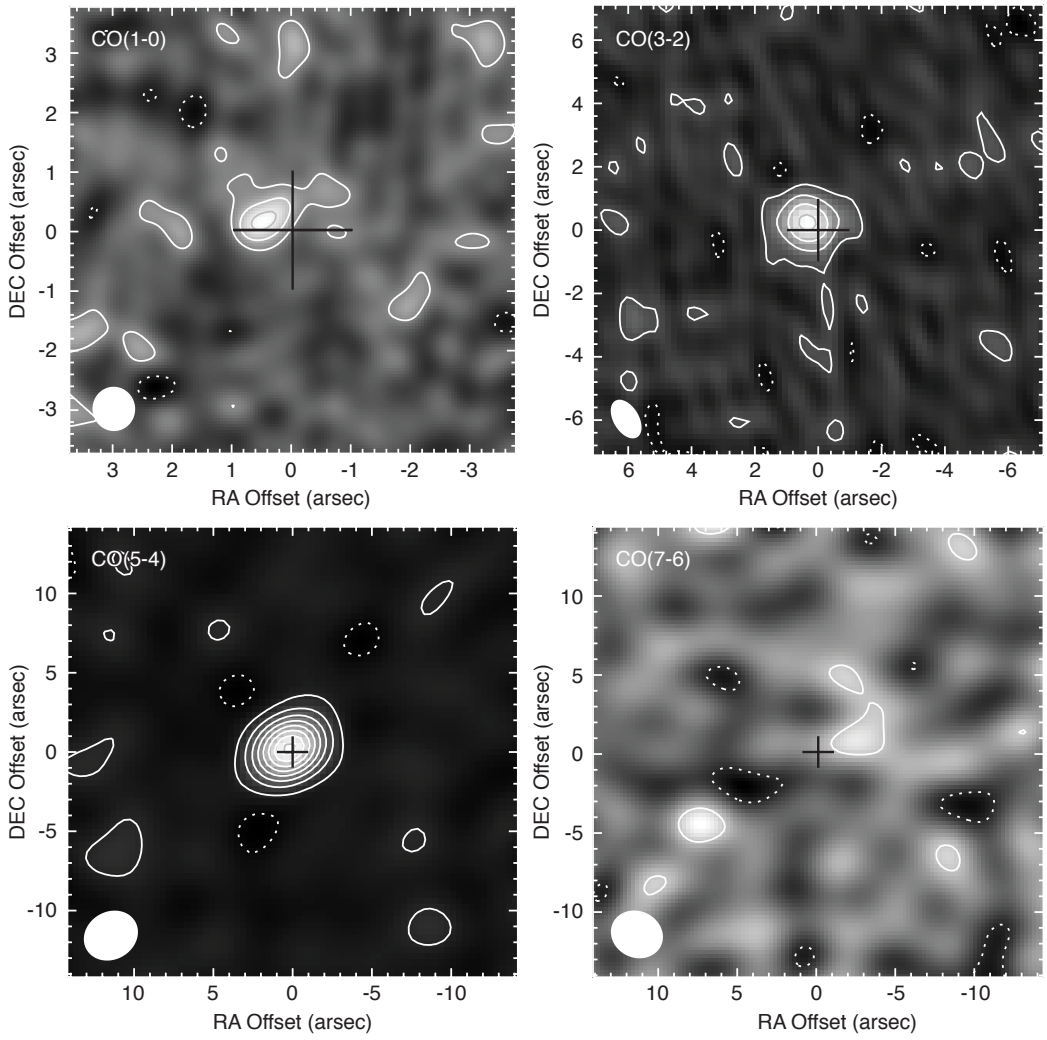

Figure 2.1 The CO(1–0) (top left), CO(3–2) (top right), CO(5–4) (bottom left), and CO(7–6) (bottom right) integrated line maps centered on the Frayer et al. (2000) continuum detection (α(J2000) = $00^{\rm h}26^{\rm m}34.^{\rm s}10$ and δ(J2000) = $+17°08'33.''7$). In order of increasing J, the contours are in multiples of $\pm2\sigma$ ($\sigma = 35\,\mu$Jy beam^{-1}), $\pm4\sigma$ (but starting at $\pm2\sigma$; $\sigma = 1.6$ mJy beam^{-1}), $\pm4\sigma$ (but starting at $\pm2\sigma$; $\sigma = 3.8$ mJy beam^{-1}), and $\pm2\sigma$ ($\sigma = 1.5$ mJy beam^{-1}), where negative contours are dotted. Synthesized beams are shown in lower left corners. The center cross indicates the position and astrometric uncertainty of Frayer et al. (2000) scaled up by a factor of five for visual clarity. Continuum subtraction has been performed for the CO(7–6) map; no other line has a significant continuum contribution.

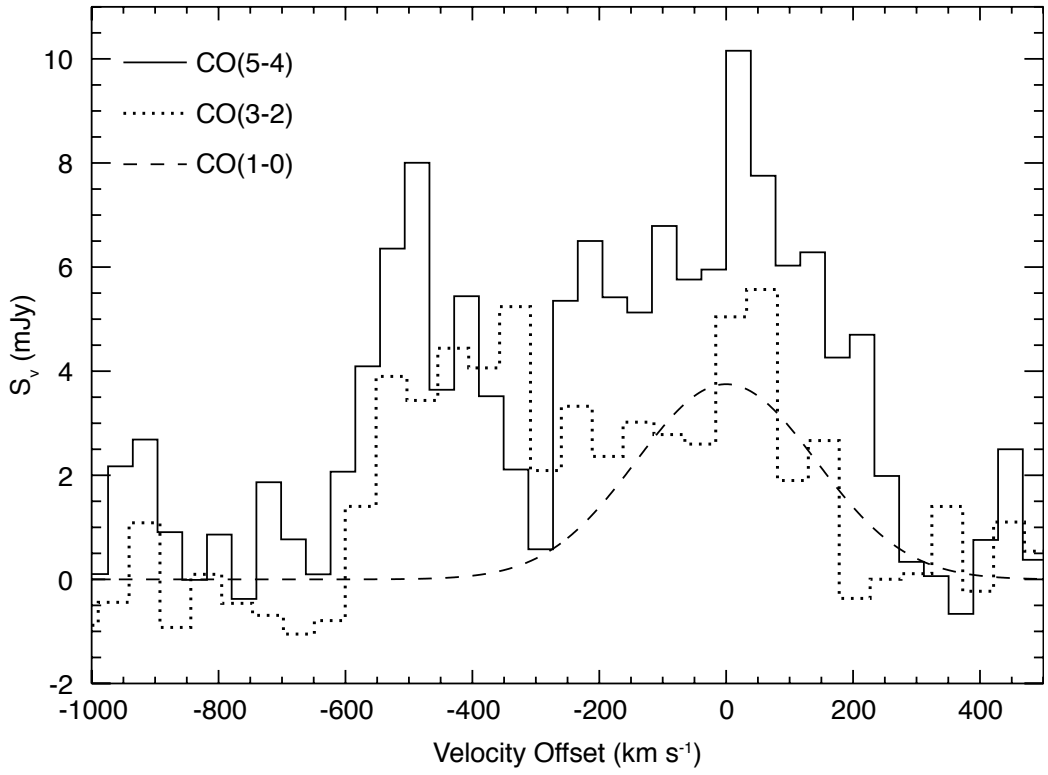

Figure 2.2 The CO(5–4) (solid) and CO(3–2) (dotted) spectral lines, plotted relative to the velocity centroid of the GBT CO(1–0) detection (Gaussian fit shown in dashed lines; multiplied by a factor of five for clarity). A second peak, blue-shifted from the CO(1–0) centroid by $\sim 500\,\mathrm{km\,s^{-1}}$, is clearly visible in the mid-J spectra.

at the VLA, integrating over the FWZI of the mid-J lines gives an integrated line flux of $0.48 \pm 0.12(\pm 0.05)\,\mathrm{Jy\,km\,s^{-1}}$, where the latter 10% uncertainty is associated with the flux calibration. The integrated line fluxes of the CO(3–2) and CO(5–4) lines are $2.62 \pm 0.25(\pm 0.26)\,\mathrm{Jy\,km\,s^{-1}}$ and $4.59 \pm 0.27(\pm 0.69)\,\mathrm{Jy\,km\,s^{-1}}$, respectively, which include 10% and 15% flux calibration uncertainties in those bands. The 3σ upper limit on the CO(7–6) line is $4.07\,\mathrm{Jy\,km\,s^{-1}}$ for a point-like source. The line fluxes and Gaussian fits to the line profiles are summarized in Table 2.1.

We do not detect significant continuum emission in the 1 cm, 3 mm, or 2 mm bands (with 3σ upper limits of 0.18 mJy, 0.16 mJy, and 0.45 mJy, respectively, for a point-like source). The observational method of position switching used with the Zpectrometer does not allow for an unambiguous continuum detection; a difference spectrum whose continuum is consistent with zero implies J00266 has continuum emission nearly equal to that of

Table 2.1. J00266 Line Measurements

Transition (Telescope)	Peak	$S\Delta\nu$ (Jy km s^{-1})	$L'_{\rm line}$[a] (10^{10} K km s^{-1} pc^2)	Peak S_ν[b] (mJy)	FWHM[b] (km s^{-1})	Offset[b,c] (km s^{-1})
CO(1–0) (GBT/Zpec)	Red	0.38 ± 0.07	7.71 ± 1.50	0.75 ± 0.14	337 ± 60	0
CO(1–0) (VLA)	Total	0.48 ± 0.13	9.81 ± 2.61	...	...	...
	Blue	0.12 ± 0.04	2.34 ± 0.89	...	...	...
	Red	0.29 ± 0.08	5.98 ± 1.61	...	...	...
	Red Core	0.15 ± 0.05	3.06 ± 0.94	...	...	...
CO(3–2) (PdBI)	Total	2.62 ± 0.36	5.91 ± 0.82	...	...	...
	Blue	1.09 ± 0.29	2.47 ± 0.65	4.76 ± 0.76	288 ± 70	-381 ± 27
	Red	1.53 ± 0.38	3.44 ± 0.85	4.51 ± 0.87	241 ± 66	13 ± 27
CO(5–4) (PdBI)	Total	4.59 ± 0.74	3.73 ± 0.60	...	...	...
	Blue	1.37 ± 0.27	1.11 ± 0.22	6.64 ± 0.98	164 ± 31	-497 ± 13
	Red	3.20 ± 0.52	2.60 ± 0.43	7.59 ± 0.67	442 ± 47	-22 ± 18
CO(7–6)[d] (SMA)	Total	< 3.93	< 1.63	...	...	...
	Blue	< 2.61	< 1.08	...	...	...
	Red	< 2.92	< 1.21	...	...	...
C I $^3P_2 \rightarrow {}^3P_1$ (SMA)	Total	4.24 ± 2.32	1.75 ± 0.96	...	...	...
	Blue[d]	< 2.37	< 0.98	...	...	...
	Red	2.44 ± 1.78	1.00 ± 0.73	...	...	...

[a]Where line refers to either CO or C I; magnification corrected.

[b]From Gaussian fits to the line profile.

[c]Relative to the CO(1–0) velocity centroid of the GBT/Zpectrometer observations.

[d]3σ upper limits.

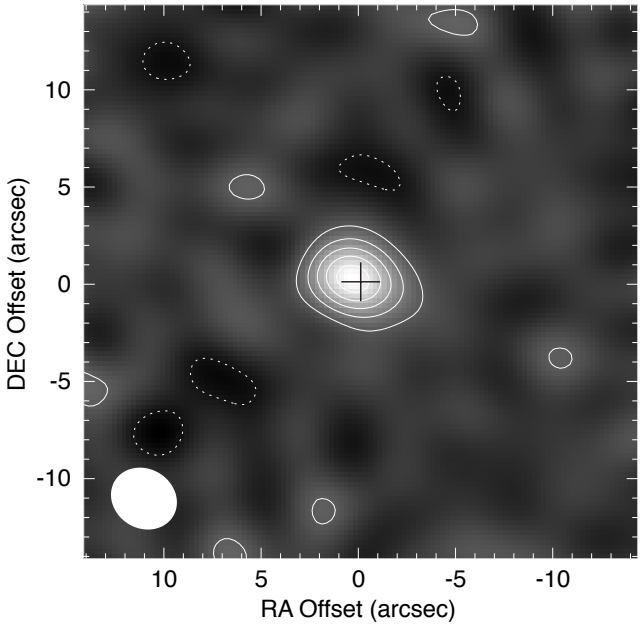

Figure 2.3 The 1 mm continuum map centered on the Frayer et al. (2000) continuum detection; $S_{1\,\mathrm{mm}} = 5.34 \pm 1.44\,\mathrm{mJy}$. Contours are in multiples of $\pm 2\sigma$ ($\sigma = 0.41\,\mathrm{mJy\,beam^{-1}}$), where negative contours are dotted. The synthesized beam is shown at lower left. The center cross indicates the position and astrometric uncertainty of Frayer et al. (2000) scaled up by a factor of five for visual clarity.

SMM J00265+1710. We do, however, detect continuum emission in the 1 mm SMA observations (Figure 2.3), with $S_{1\,\mathrm{mm}} = 5.34 \pm 0.97(\pm 1.07)\,\mathrm{mJy}$ (using a 20% flux calibration uncertainty). The continuum fluxes measured in the upper and lower sidebands (separated by 12 GHz in their band centers) are consistent within their 1σ statistical uncertainties, indicating a flat spectral index. Assuming this spectral index, our 1.4 mm continuum detection is consistent with $S_{1.3\,\mathrm{mm}} = 6.0 \pm 1.1\,\mathrm{mJy}$ from Frayer et al. (2000). The position of our continuum detection is also consistent with those of the CO line detections and the Frayer et al. (2000) 1.3 mm detection.

In Figure 2.4, we show the continuum-subtracted spectra for the upper sideband of our SMA observations, indicating the velocity range over which we would expect to see the CO(7–6) line based on our PdBI observations. Within the observed spectral bandpass we have marginally detected the C I $^3\mathrm{P}_2 \rightarrow {}^3\mathrm{P}_1$ fine structure line at a $> 4\sigma$ level (Figure 2.5). The total line flux is $4.24 \pm 2.16(\pm 0.85)\,\mathrm{Jy\,km\,s^{-1}}$. While the position of the C I emission is consistent with those of our CO and 1 mm continuum detections, it is only marginally

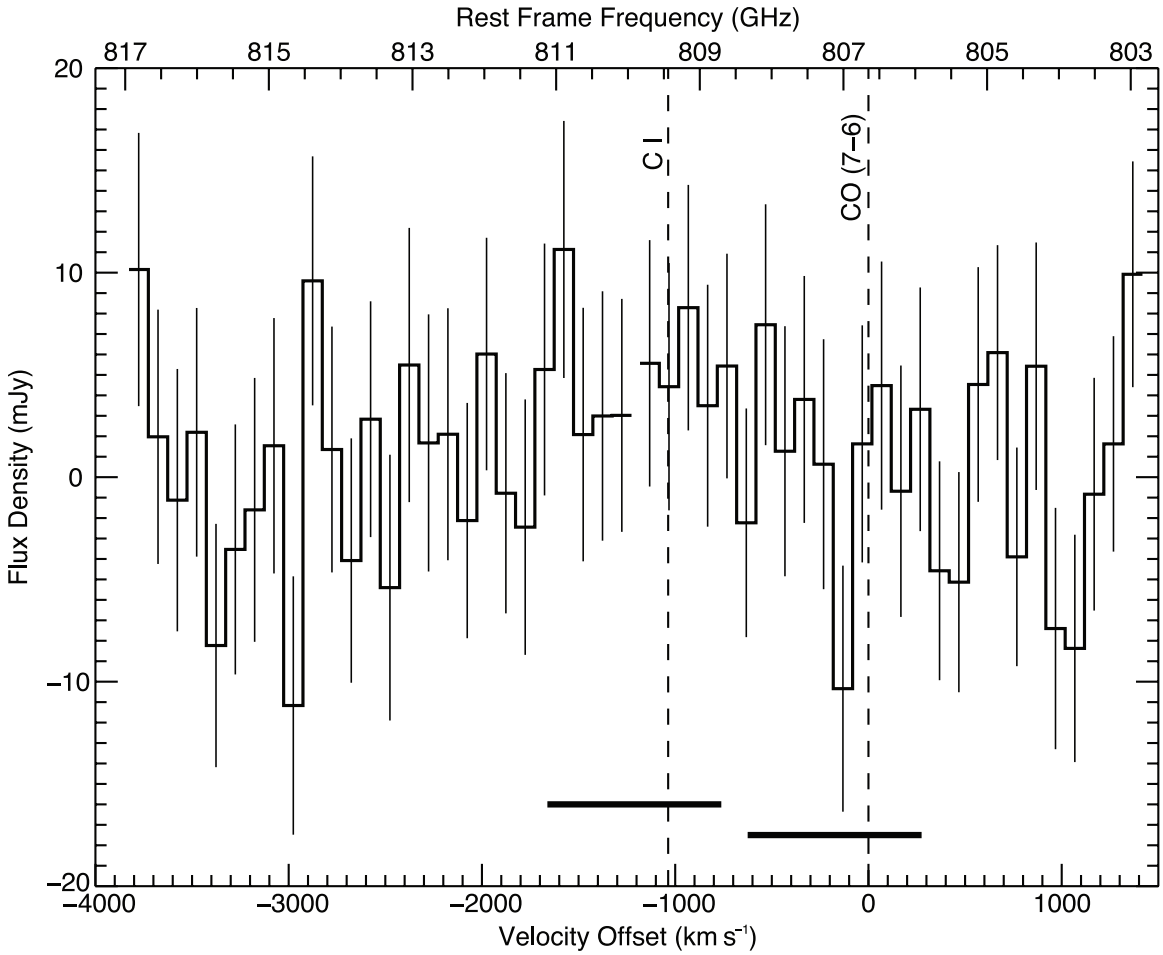

Figure 2.4 The $100\,\mathrm{km\,s^{-1}}$ resolution SMA spectrum plotted relative to the expected CO(7–6) rest frame velocity. The vertical dashed lines indicate the undetected CO(7–6) line and the marginally detected C I $^3P_2 \rightarrow {}^3P_1$ line; the expected FWZI velocity range for those lines, based on the PdBI observations, are show with thick horizontal bars. The break at $\sim -1200\,\mathrm{km\,s^{-1}}$ is from a 32 MHz coverage gap of the SMA correlator.

consistent with that of the Frayer et al. (2000) continuum detection.

2.4 Analysis

2.4.1 Physical and Dynamical Structure

The two peaks in the mid-J spectra of J00266 are indicative of either a rotating structure or two separate physical components. Several lines of evidence lead us to favor the latter scenario, with a division between the two components occurring at $\sim -300\,\mathrm{km\,s^{-1}}$. First, the higher S/N CO(5–4) spectrum shows a strong division and asymmetry between the two

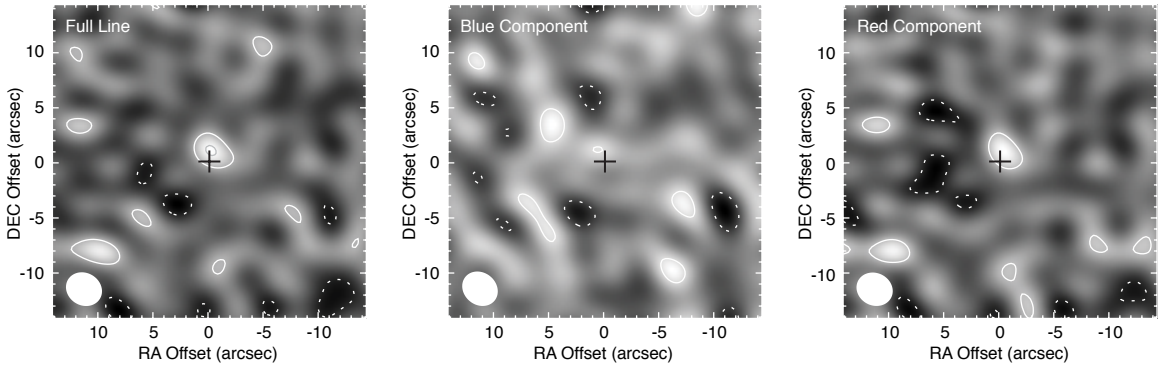

Figure 2.5 Tentative detection of the C I line for the full line (left), blue component (middle), and red component (right). Contours are in multiples of $\pm 2\sigma$ (the negative contours are dotted) where $\sigma = 1.45\,\mathrm{mJy\,beam^{-1}}$, $2.25\,\mathrm{mJy\,beam^{-1}}$, and $1.81\,\mathrm{mJy\,beam^{-1}}$ from left to right. The synthesized beam is shown at lower left. The center cross indicates the position and astrometric uncertainty of Frayer et al. (2000) scaled up by a factor of five for visual clarity.

peaks, which is somewhat unlikely for a rotating disk. Second, we see different kinematics in the two components. Figure 2.6 shows the $\pm 3\sigma$ contours of the CO(3–2) channel maps; the $-527 \rightarrow -332\,\mathrm{km\,s^{-1}}$ channels of the blue peak are spatially coincident with each other and clearly separate from the redder channels, which show a notable velocity gradient. Examination of the peak flux positions in the individual channel maps of the CO(3–2) line also shows a clear progression in velocity along a line of position angle ~ -70 degrees for the channels redder than $-300\,\mathrm{km\,s^{-1}}$, while the peak flux positions in the remaining blue channels are scattered. Third, rescaling the CO(3–2) line profile so that the peak flux of the red peak component matches that of the CO(5–4) line would *not* result in similarly matching line strengths in the blue peak. The different mid-J line ratios between the two peaks is indicative of different excitation conditions, which is further supported by the strong Zpectrometer detection of the CO(1–0) line at the velocity of the red peak but not at the velocity of the blue peak. If the two CO peaks were produced by the same structure, the close physical association makes it unlikely that they would have very different excitation conditions. The differing kinematics and gas conditions are strong evidence that J00266 is a merger between two galaxies, one with a velocity gradient and multi-phase molecular ISM (see Section 2.4.2) and one with no evidence for ordered motion and a single-phase ISM (see Section 2.4.2), with a relative velocity offset of $\sim 500\,\mathrm{km\,s^{-1}}$ and close alignment along

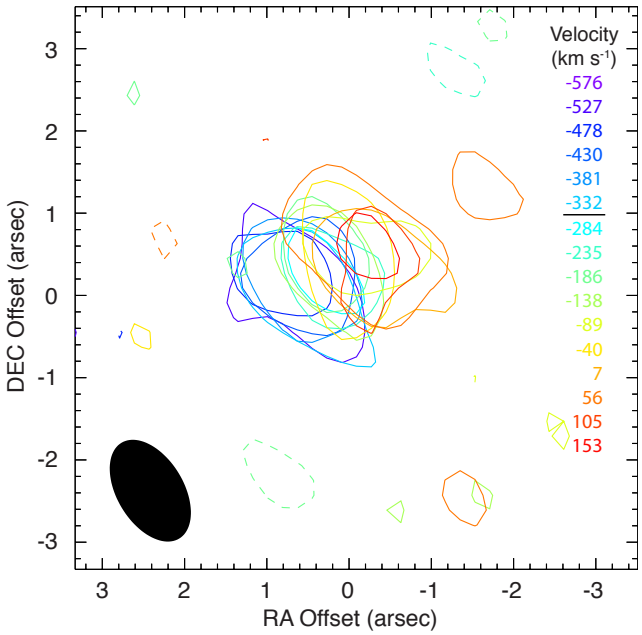

Figure 2.6 Overlaid contours of the CO(3–2) channel maps, colorized by the channels' relative velocities; the black horizontal line marks the division between the two components. The synthesized beam is shown at lower left. Only the positive (solid) and negative (dashed) 3σ contours are shown ($1\sigma = 3.6\,\mathrm{mJy\,beam^{-1}}$).

our line of sight.

For the rest of the analysis, we therefore consider the blue component (defined by the $-600 \rightarrow -308\,\mathrm{km\,s^{-1}}$ velocity range for the CO(3–2) line, and the $-624 \rightarrow -312\,\mathrm{km\,s^{-1}}$ velocity range for the CO(5–4) line) and the red component (defined by the $-308 \rightarrow 178\,\mathrm{km\,s^{-1}}$ velocity range for the CO(3–2) line, and the $-273 \rightarrow 273\,\mathrm{km\,s^{-1}}$ velocity range for the CO(5–4) line) separately. It is important to note that this division between the components for the CO(3–2) line is not a particularly good match to the double-Gaussian line profile fit given in Table 2.1. However, fixing the velocity offset of the blue component of the CO(3–2) line to match the CO(5–4) value results in a much closer match between the different line FWHMs for each component, with only a slight change in the reduced-χ^2 value of the two fits (0.66 without the constraint vs. 0.79 with the constraint).

The integrated line component maps are given in Figure 2.7 for the CO lines, and in Figure 2.5 for the C I line. In order to obtain upper limits for our non-detections, and line measurements for our weak detections, we consistently integrate over the $-275 \rightarrow 275\,\mathrm{km\,s^{-1}}$ velocity range for the red component and the $-625 \rightarrow -275\,\mathrm{km\,s^{-1}}$ velocity

range for the blue component. Our line measurements and upper limits for the VLA and SMA observations are insensitive to the exact velocity selection for the two components, with reasonable variations in the velocity selection ($< 100\,\mathrm{km\,s^{-1}}$) yielding results that are consistent within the maps' 1σ statistical uncertainties. The component line measurements are summarized in Table 2.1.

For the CO(1–0) VLA observations, we have a 4.6σ detection of the blue component that was not seen by the Zpectrometer; our measured line flux is consistent with the Zpectrometer upper limits. The red component map hints at the presence of an extended emission structure surrounding a bright core. The integrated line flux for the red component from the VLA data is lower than (but consistent with) the prior single-dish GBT Zpectrometer measurement. Test VLA maps made using a Gaussian taper with up to a $3''$ FWHM do not reveal any additional resolved-out flux. If we ignore the extended emission and concentrate only on the bright core, the measured line flux is $0.15 \pm 0.05\,\mathrm{Jy\,km\,s^{-1}}$, making the bright core the source of $\sim 50\%$ of the total red component emission. The position of the red core is consistent with the positions of the red components in the other detected lines.

For the marginal detection of the C I line, it appears that the bulk of the emission originates from the red component. The red component is detected at the 3.75σ level, with an integrated line flux of $2.44 \pm 1.78\,\mathrm{Jy\,km\,s^{-1}}$. The peak flux position is consistent with the red component maps of the CO lines.

Second moment maps give us estimates for the turbulent velocity widths in both components of J00266 (although with the large beam size relative to the source, we expect these to be affected by beam smearing). We find the velocity dispersion in the blue component to be $61 \pm 28\,\mathrm{km\,s^{-1}}$, consistent with the line FWHM. The red component has an average velocity dispersion of $101 \pm 37\,\mathrm{km\,s^{-1}}$, which is significantly less than the line FWHM. This distinction is consistent with a picture in which the blue component has dispersion-dominated kinematics while the red component has an additional velocity gradient.

uv-plane fits to the resolved CO(3–2) emission of the red and blue components show a centroid position offset of $0.''73$, which is significant considering the $1.''36 \times 0.''81$ beam and $> 10\sigma$ detection of the two components. To convert this separation to a physical scale, we must account for gravitational lensing. Frayer et al. (2000) suggests a magnification factor

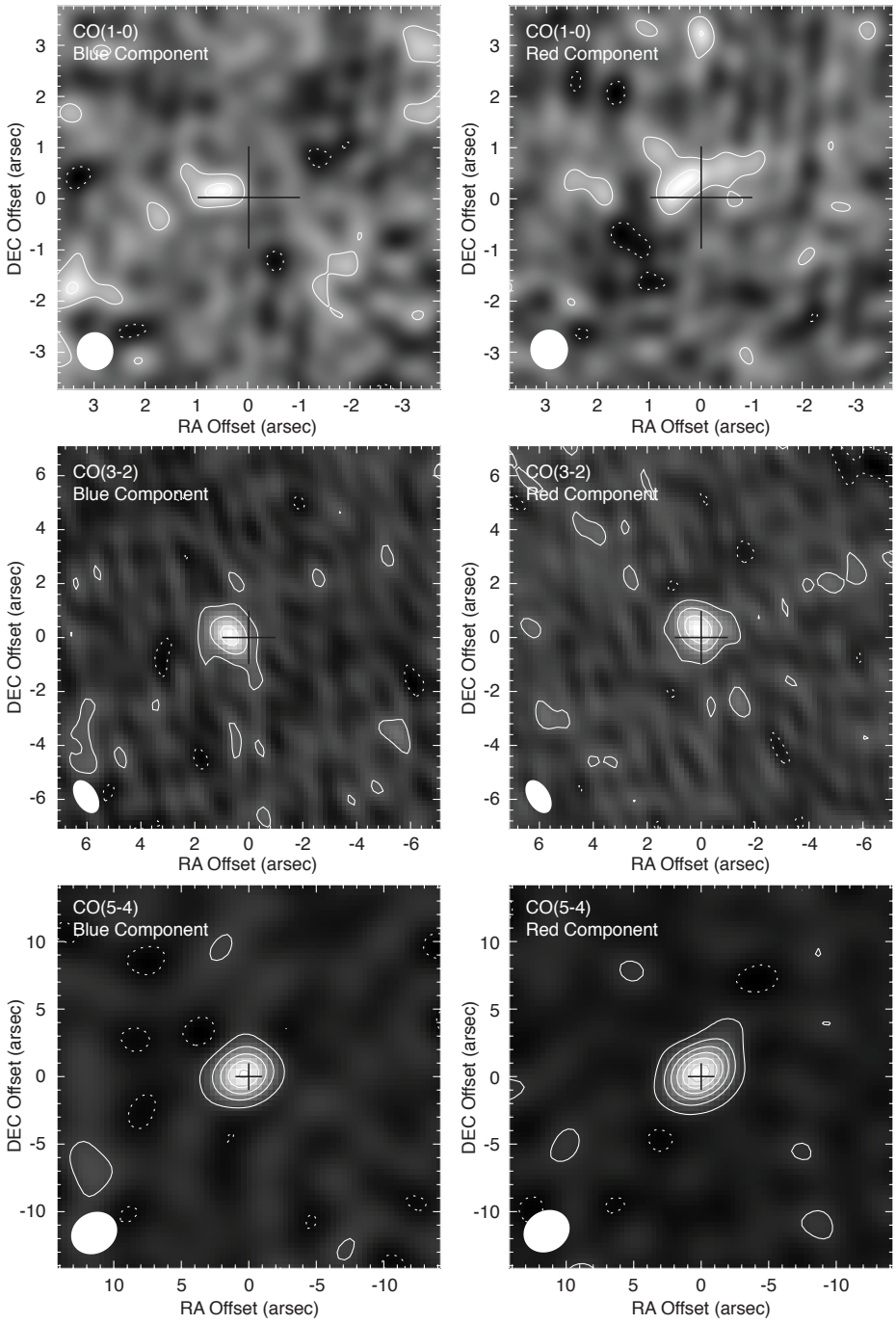

Figure 2.7 The CO(1–0) (top row), CO(3–2) (middle row), and CO(5–4) (bottom row) integrated line maps of the blue component (left column) and red component (right column) centered on the Frayer et al. (2000) continuum detection. In order of increasing J, the contours are in multiples of $\pm 2\sigma$ ($\sigma_{\rm blue} = 57\,\mu{\rm Jy\,beam^{-1}}$; $\sigma_{\rm red} = 43\,\mu{\rm Jy\,beam^{-1}}$), $\pm 4\sigma$ (but starting at $\pm 2\sigma$; $\sigma_{\rm blue} = 0.93\,{\rm mJy\,beam^{-1}}$; $\sigma_{\rm red} = 1.24\,{\rm mJy\,beam^{-1}}$), and $\pm 4\sigma$ (but starting at $\pm 2\sigma$; $\sigma_{\rm blue} = 2.13\,{\rm mJy\,beam^{-1}}$; $\sigma_{\rm red} = 3.09\,{\rm mJy\,beam^{-1}}$) where negative contours are dotted. The center cross indicates the position and astrometric uncertainty of Frayer et al. (2000) scaled up by a factor of five; synthesized beams are shown in lower left corners.

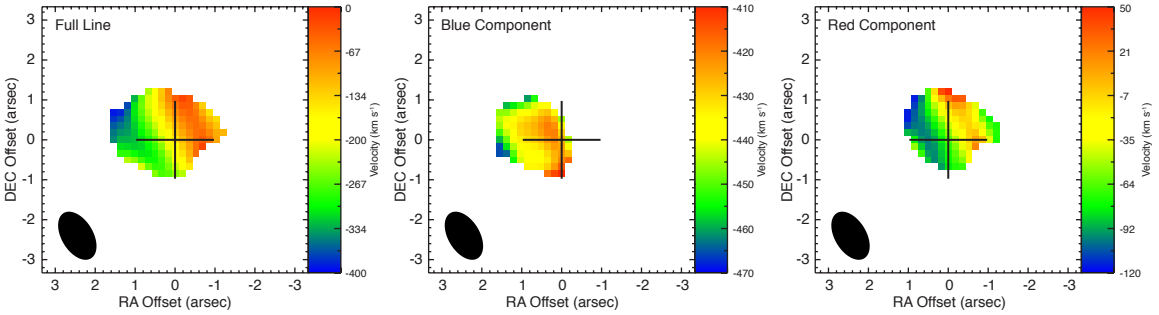

Figure 2.8 The CO(3–2) first moment maps of the full line (left), blue component (middle), and red component (right). Positions are relative to the Frayer et al. (2000) continuum detection (center cross) where the astrometric uncertainty is scaled up by a factor of five. Pixels with values $< 3\sigma$ in the corresponding integrated line map have been blanked out. Synthesized beams are shown in lower left corners. These maps indicate that the blue component is dispersion dominated while the red component has a velocity gradient. Apparent "flips" in the red component velocity gradient are caused by the large spatial extent of the central channels (illustrated in Figure 2.6).

of 2.4 arising from a combination of the lensing cluster (Cl0024+1654; $z = 0.39$) and the galaxy M8 ($z = 0.44$), but assumes the redshift of J00266 to be $z = 3.5$. Following the procedure outlined by Frayer et al. (2000) to re-scale the lensing magnifications based on the appropriate angular size distance, we adopt a new magnification factor of 1.75 (albeit with considerable uncertainty). The projected separation between the two components of J00266 is therefore 4.44 kpc at $z = 2.742$, with an unknown separation along the line of sight. The blue component is best fit by a circular Gaussian with a FWHP of $0.''86 \pm 0.''11$ (radius of 2.23 ± 0.28 kpc). The red component is best fit by an elliptical Gaussian of major and minor axis FWHPs of $1.''11 \pm 0.''12$ and $0.''85 \pm 0.''11$; the major axis is at a position angle of -59 ± 19 degrees, which is closely aligned with the velocity gradient apparent in the first moment map (Figure 2.8). The *uv* fit result corresponds to a radius along the velocity gradient of 2.88 ± 0.31 kpc. Using the measured source sizes and velocity structures observed in the two components (assuming the blue component is a dispersion-dominated virialized sphere, and the velocity gradient of the red component is from rotation), we estimate dynamical masses of $(1.30 \pm 0.52) \times 10^{10}\, M_\odot$ for the blue component and $M_{\rm dyn} \sin^2(i) = (1.01 \pm 0.30) \times 10^{11}\, M_\odot$ for the red component. Based on these estimates of the dynamical masses, we find that J00266 is a merger with a mass ratio of $(7.7 \pm 3.9)/\sin^2(i)$. Assuming an average inclination correction of 2/3, the mass ratio becomes 11.7 ± 5.8.

Based on the lensing-corrected line luminosities given in Table 2.1, we estimate the gas masses for the two components of J00266. Using the Zpectrometer-measured CO(1–0) line flux, the molecular gas mass of the red component is $(6.17 \pm 1.20) \times 10^{10} (\alpha_{\rm CO}/0.8)\,{\rm M}_\odot$. For the blue component, using the VLA-measured CO(1–0) line flux, the molecular gas mass is $(1.88 \pm 0.72) \times 10^{10} (\alpha_{\rm CO}/0.8)\,{\rm M}_\odot$. The gas masses for both components are less than or approximately equal to their estimated dynamical masses. In the case of the blue component, the gas mass nearly matches the dynamical mass. While it is possible for the dynamical mass to be dominated by the gas mass for the limited volume probed by the gas distribution, more reasonable gas fractions are within the uncertainties of our measurements, so we do not think the tension between those two values is significant. While we have assumed a standard gas mass conversion factor of $\alpha_{\rm CO} = 0.8\,M_\odot\,({\rm K\,km\,s^{-1}\,pc^2})^{-1}$ for U/LIRGs, there is some evidence for variation in $\alpha_{\rm CO}$ within the population of SMGs (e.g., Tacconi et al. 2008; Hodge et al. 2012; Sharon et al. 2013a). Galactic values of the CO-to-H_2 conversion factor could make both components' gas masses larger than their dynamical masses (depending on the inclination correction for the red component's $M_{\rm dyn}$), and are therefore disfavored. The gas mass ratio of these two components is therefore $(3.3 \pm 1.4) \times (\alpha_{\rm CO}/0.8)_{\rm red}/(\alpha_{\rm CO}/0.8)_{\rm blue}$.

Our marginal detections of the C I can also be used as an alternative test of the gas mass (e.g. Weiß et al. 2003). Since we do not have measurements of both fine structure lines, we assume $T_{ex} = 50\,{\rm K}$ for the blue component and $T_{ex} = 12\,{\rm K}$ for the red component based on the LVG modeling presented in Section 2.4.2. This yields C I masses of $M_{\rm C\,I} = (2.42 \pm 1.76) \times 10^8\,M_\odot$ for the red component and a 3σ upper limit of $M_{\rm C\,I} < 1.34 \times 10^7\,M_\odot$ for the blue component. Assuming the average C I/CO abundance ratio for SMGs given in Walter et al. (2011) (though corrected by a factor of 0.6 for the red component given our measured $r_{3,1}$), this yields $M_{\rm H_2} = (8.00 \pm 5.82) \times 10^{11}\,M_\odot$ for the red component and $M_{\rm H_2} < 2.67 \times 10^{10}$ for the blue component. While the blue component molecular gas mass upper limit is consistent with that determined using the CO line luminosity, there is a large discrepancy for the red component gas mass. This discrepancy is likely caused by the assumed excitation temperature; this temperature may be representative of the cold molecular gas in the red component, but the neutral carbon emission traces warmer neutral gas. Assuming a more conventional $T_{\rm ex} = 30\,{\rm K}$ reduces the masses to

Table 2.2. J00266 Line Ratios

Component	$r_{7,5}$[a]	$r_{7,3}$[a]	$r_{7,1}$[a]	$r_{5,3}$	$r_{5,1}$	$r_{3,1}$
Total	< 0.44	< 0.28	< 0.21	0.63 ± 0.13	0.48 ± 0.12	0.77 ± 0.18
Blue	< 0.97	< 0.44	< 0.46	0.45 ± 0.15	0.48 ± 0.20	1.05 ± 0.49
Red	< 0.47	< 0.35	< 0.16	0.75 ± 0.22	0.34 ± 0.09	0.45 ± 0.14

Note. — Uses the Zpectrometer measured CO(1–0) line flux for the total and red component fluxes, and the VLA CO(1–0) measurement for the blue component.

[a]3σ upper limits.

$M_{\rm C\,I} = (2.19 \pm 1.60) \times 10^7\,M_\odot$ and $M_{\rm H_2} = (7.24 \pm 5.29) \times 10^{10}\,M_\odot$, which is entirely consistent with CO-determined molecular gas mass.

2.4.2 Excitation Conditions

We can compare CO excitation in J00266 to that in other SMGs by analyzing line ratios (Equation 1.1). Table 2.2 lists our measured values of $r_{J,J'}$ for J00266, for both the full line and the two components separately (in the case of CO(7–6) line, 3σ upper limits are given). For both the full-line and red component values of $r_{J,1}$ we use the Zpectrometer CO(1–0) measurements, while the blue component values are determined from the VLA map.

For typical SMG kinetic temperatures, brightness temperature ratios are likely not in the asymptotic Rayleigh-Jeans limit, even if the gas is sufficiently dense for CO levels to be thermalized (Harris et al. 2010). We therefore are not surprised to measure $r_{J>1,1}$ to be less than unity for J00266. All of our measured $r_{3,1}$ values, including for the two separate components, are formally consistent with the average $r_{3,1} \sim 0.6$ observed in other SMGs (e.g., Swinbank et al. 2010a; Harris et al. 2010; Ivison et al. 2011; Danielson et al. 2011; Bothwell et al. 2013). However, the red and blue components of J00266 have different line ratios. The red component $r_{3,1}$ is about 1σ lower than the population average, and the blue component $r_{3,1}$ is approximately equal to unity (though with substantial uncertainty), similar to those of quasar host galaxies (Riechers et al. 2011a) and the SMG SMM J14011+0252

(Sharon et al. 2013a). Differences between the two components of J00266 are also seen in the CO(5–4)/CO(3–2) line ratio, $r_{5,3}$, where the red component $r_{5,3}$ is higher than the population average and the blue component value is lower than the population average ($r_{5,3} = 0.62$; Bothwell et al. 2013).

In order to constrain the physical conditions of the molecular gas in J00266, we have compared our measured line ratios to the results of a radiative transfer model using the large velocity gradient (LVG) approximation. The LVG modeling follows the methods detailed in Ward (2002); additional details about the LVG modeling can be found in Appendix B. The model was adapted to include the CMB radiation, which can affect CO rotational level populations at high redshift where $T_{\rm CMB}$ and $T_{\rm exc}$ are comparable (for low-J lines). Collision rates between CO and both ortho- and para-H_2 were taken from Yang et al. (2010), and collision rates between CO and He were taken from Cecchi-Pestellini et al. (2002). These collision rates were interpolated onto the temperature spacing we probe in the LVG model using a quadratic spline. The ortho-to-para-H_2 ratio is determined as a function of temperature (Takahashi 2001), which asymptotes to the common assumption of a constant ratio equal to three for high temperatures ($\sim 100\,{\rm K}$; the differences in the CO level populations resulting from the temperature-dependent and constant values of the ortho-to-para ratio are negligible). We assume a spherical cloud geometry with the escape probability given by Goldreich & Kwan (1974).

The output of the LVG code is the calculated line luminosity per unit density, $\Lambda_{J,J-1} = h\nu_{J,J-1}A_{J,J-1}n_{\rm H_2}x_{\rm CO}\chi_J\beta_{J,J-1}$ for a specific $J \rightarrow J-1$ transition (χ_J, the fraction of CO in the Jth rotational state, and the escape probability, $\beta_{J,J-1}$, are the chief unknowns determined by the LVG code). The line luminosity is a function of three parameters that detail the physical conditions of the molecular gas: the kinetic temperature, the H_2 density, and the CO column density per unit line width (T, $n_{\rm H_2}$, and $N_{\rm CO}/\Delta v$). We generate a library of line luminosities for the three input parameters, which are sampled at $\Delta T = 2\,{\rm K}$ for $0\,{\rm K} \leq T \leq 200\,{\rm K}$, $\Delta \log(n_{\rm H_2}/{\rm cm^{-3}}) = 0.1$ for $0 \leq \log(n_{\rm H_2}/{\rm cm^{-3}}) \leq 7$, and $\Delta \log((N_{\rm CO}/\Delta v)/{\rm cm^{-2}\,km^{-1}\,s}) = 0.25$ for $15 \leq \log((N_{\rm CO}/\Delta v)/{\rm cm^{-2}\,km^{-1}\,s}) \leq 22$. By taking the ratio of two transitions for the same input parameter triplet (T, $n_{\rm H_2}$, and $N_{\rm CO}/\Delta v$), we have a predicted line ratio as produced by a single phase molecular ISM to

compare to our measurements. By evaluating the model line ratios, we avoid uncertainty due to choice of $x_{\rm CO}$, the relative abundance of CO to H_2. Given observed parameters like the source size and velocity structure and a best fit model, we can determine a most likely value of $x_{\rm CO}$.

Since recent work indicates that the line ratios of SMGs are largely inconsistent with single-phase models of the molecular ISM (Swinbank et al. 2010a; Harris et al. 2010; Ivison et al. 2011; Danielson et al. 2011; Bothwell et al. 2013), we also consider two-phase models. In order to determine the predicted line ratios for the two-phase LVG model, we iteratively determine the line intensity for every possible pair of input parameter triplets for a range of filling factors. The two-phase line ratio for given CO transitions $J \rightarrow J-1$ and $J' \rightarrow J'-1$ is given by

$$r_{J,J'} = \frac{f_{\rm c}\Lambda_J(T_{\rm c}, n_{\rm c}, N_{\rm c}/\Delta v) + f_{\rm w}\Lambda_J(T_{\rm w}, n_{\rm w}, N_{\rm w}/\Delta v)}{f_{\rm c}\Lambda_{J'}(T_{\rm c}, n_{\rm c,}N_{\rm c}/\Delta v) + f_{\rm w}\Lambda_{J'}(T_{\rm w}, n_{\rm w}, N_{\rm w}/\Delta v)} \left(\frac{\nu_{J'}}{\nu_J}\right)^3, \tag{2.1}$$

where the "c" and "w" subscripts denote the cold and warm phases, we have dropped the redundant H_2, CO, $J-1$, and $J'-1$ subscripts, and the additional frequency term is used to put the predicted line ratio in units of brightness temperature. Since $r_{J,J'}$ depends on the ratio of $f_{\rm c}/f_{\rm w}$ rather than a single choice in each parameter (the filling factors can be any value between zero and one, which means $f_{\rm c}/f_{\rm w}$ can be any value between zero and infinity), we can eliminate an excess parameter by only probing the ratio of the filling factors; the ratio was sampled every $\Delta \log(f_{\rm c}/f_{\rm w}) = 0.2$ for $0 \leq \log(f_{\rm c}/f_{\rm w}) \leq 5$.

Since both the single-phase and two-phase LVG models have numbers of free parameters comparable to or greater than the number of measurements for J00266, and these measurements have significant uncertainties, we use a Bayesian analysis to determine the likelihood distributions for the various model parameters. This approach (detailed in Ward et al. 2003) is preferred to a χ^2 minimization technique since it more accurately reflects the uncertainties in the measurements. Priors have been carefully chosen to (1) reflect our lack of pre-existing knowledge about the physical conditions of the molecular gas, (2) rule out scenarios that are obviously physically unrealistic, and (3) compensate for biases towards

high temperature/density models that result from the large logarithmically sampled parameter space. We therefore adopt a uniform prior in the logarithm of kinetic temperature, H_2 density, CO column density per velocity gradient, and (in the case of the two-phase model) filling factor ratio. While this choice effectively weights the likelihood distribution towards colder phase solutions, a substantial fraction of SMGs' gas mass is in the cold phase, making its characterization of primary interest. For systems well-described by a single-phase molecular ISM, χ^2 minimization and Bayesian techniques favor similar models. The best-fit models for J00266 are relatively insensitive to the choice between logarithmic or uniform priors, meaning that the logarithmic prior is not significantly biasing our results. Additional priors are used to rule out models with kinetic temperatures less than the CMB temperature and regions of the two-phase parameter space where the cool phase is warmer than the warm phase.

In addition to the basic priors described above, which are in place for all applications of the Bayesian analysis, in cases where the LVG model produces extremely degenerate results, it is worth considering additional (physically motivated) priors to limit the available parameter space. First, in a multi-phase ISM, optically thick emission should dominate the observed light, overwhelming any optically thin emission. We therefore restrict our analysis to models that produce optically thick CO emission. Second, detectability constrains the CO brightness temperature to be greater than the CMB temperature (at the source redshift). This prior requires knowledge of the source size, which can be uncertain if unresolved structure exists in the source, and assumes that the emission in different CO lines is coming from the same physical regions of gas (though the latter assumption is necessary for all single-phase LVG models, as well as for some fraction of the emission in multi-phase models). In practice, even with the most severe assumptions about source size, this prior eliminates $< 1\%$ of parameter space and duplicates other cuts (such as the requirement of $\tau > 1$). Third (also dependent on source size), we require that the CO column length be less than the diameter of the object. Given an estimate of the source size and line width, cuts on the CO column can remove the highest values of $N_{\rm CO}/\Delta v$. Fourth, we require the molecular gas mass implied by the model to be less than the dynamical mass ($n_{\rm H_2} \leq 3M_{\rm dyn}/(m_{\rm H_2} 4\pi r^3)$). Fifth, in cases where we expect that most of the gas mass is in dense, star-forming, virialized

clouds, we can introduce a prior based on the degree of virialization (Equation 3.1 and Appendix C.3; e.g., Papadopoulos & Seaquist 1999; Ivison et al. 2011); we eliminate large densities that would create velocity gradients smaller than the measured value for J00266 under the assumption of virialization, which are dynamically unobtainable. Additional details about the priors used in the LVG modeling can be found in Appendix C.

We note that in the portions of the LVG analysis where the global velocity gradient is assumed, we use the source size uncorrected for the magnification factor. The velocity gradients are therefore $\sim 30\%$ smaller than the lensing-corrected values. However, this difference would not significantly effect our results.

The Blue Component

The line ratios for the the blue component of J00266 can be reproduced by single-phase LVG models. Based on the Bayesian analysis, the best-fit model parameters are $T = 16\,\mathrm{K}$, $n_{\mathrm{H_2}} = 10^{7.0}\,\mathrm{cm^{-3}}$, and $N_{\mathrm{CO}}/\Delta v = 10^{16.25}\,\mathrm{cm^{-2}\,km^{-1}\,s}$; the best-fit CO SLED is shown in Figure 2.9. However, the best-fit H_2 density is at the edge of the parameter space, indicating it may not be a trustworthy value. In addition, a wide range of parameters can reproduce the line ratios within the measured errors. To illustrate this degeneracy, we show three additional CO SLEDs in Figure 2.9: the minimum χ^2 model ($T = 18\,\mathrm{K}$, $n_{\mathrm{H_2}} = 10^{5.2}\,\mathrm{cm^{-3}}$, $N_{\mathrm{CO}}/\Delta v = 10^{16.25}\,\mathrm{cm^{-2}\,km^{-1}\,s}$), the highest probability model in which all line emission is optically thick ($T = 16\,\mathrm{K}$, $n_{\mathrm{H_2}} = 10^{4.0}\,\mathrm{cm^{-3}}$, $N_{\mathrm{CO}}/\Delta v = 10^{18.00}\,\mathrm{cm^{-2}\,km^{-1}\,s}$), and the minimum χ^2 model in which all line emission must also be optically thick ($T = 48\,\mathrm{K}$, $n_{\mathrm{H_2}} = 10^{3.6}\,\mathrm{cm^{-3}}$, $N_{\mathrm{CO}}/\Delta v = 10^{17.00}\,\mathrm{cm^{-2}\,km^{-1}\,s}$).

The posterior probability distributions for these parameters are given in Figure 2.10. The marginalized probability distributions generally do not peak at the locations of the maximum probability (or mininimum χ^2) model parameters. This apparent inconsistency is due to the significant degeneracies between models that adequately reproduce the observed line ratios, illustrated in Figure 2.11 and Figure 2.12. In the case of the blue component in J00266, the line ratios are indicative of an increased population of CO in excited rotational states relative to a thermalized distribution at the temperature of the CMB. These possibilities result in the "L"-shaped degenerate parameter space along T_{kin} and $n_{\mathrm{H_2}}$ seen in the top

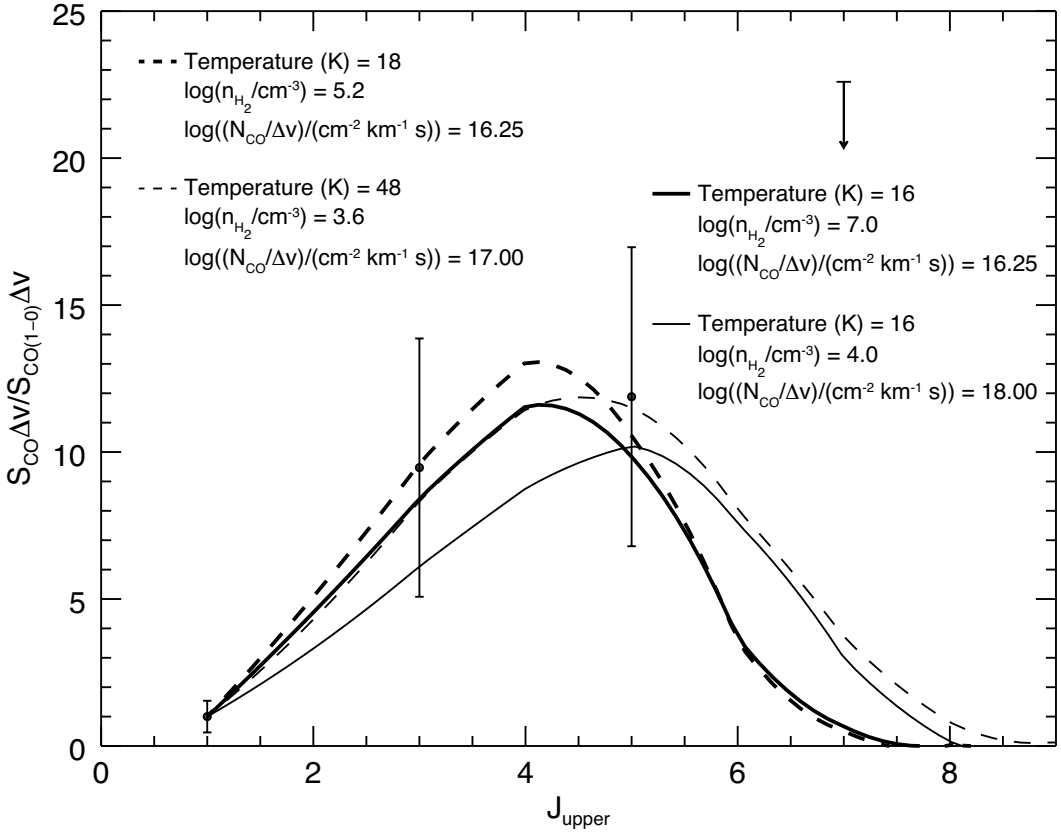

Figure 2.9 CO SLEDs for the best-fitting models (lines) and the measured line ratios and 1σ errors (points) for the blue component of J00266. The 3σ upper limit on the CO(7–6) line is given by the arrow. The solid lines are for the highest-probability models from the Bayesian analysis, and the dashed lines are for models that minimize χ^2. Thick lines are for the models where the full LVG parameter space was considered (with the exception of $T < T_{\rm CMB}$) and thin lines are for models that require all of the line emission to be optically thick.

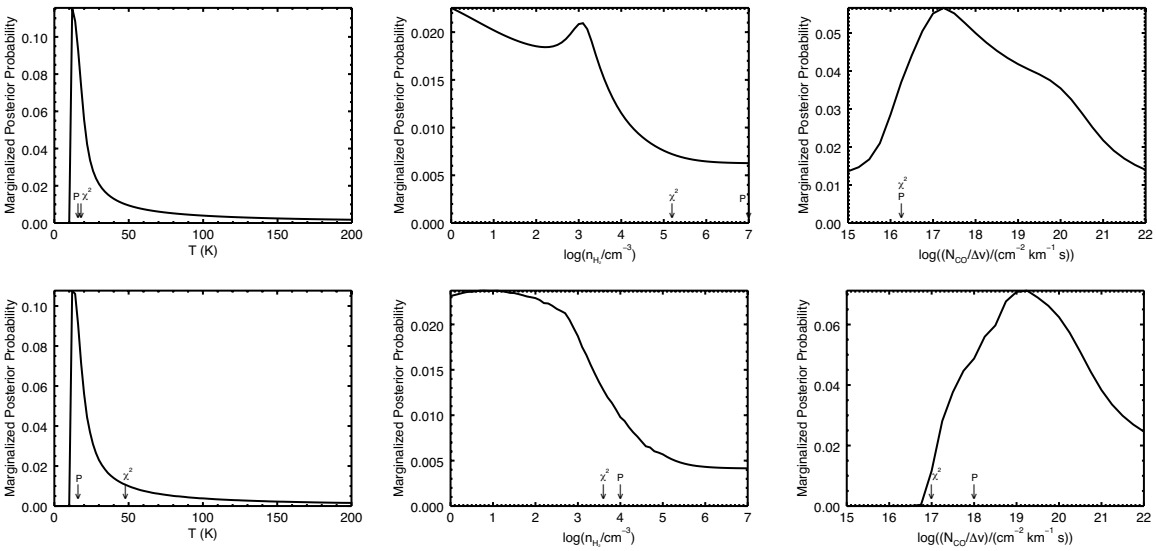

Figure 2.10 The marginalized likelihood distributions for the single-phase model for the blue component of J00266, where the entire parameter space is available (top row) and where models with optically thin line emission have been removed (bottom row). The exact parameters of the highest-probability and minimum-χ^2 models are indicated with arrows (labeled with "P" and "χ^2", respectively).

panels of Figure 2.11. Since the number of collisions that occurs is proportional to both CO density and H_2 density, the additional degeneracy between n_{H_2} and $N_{CO}/\Delta v$ is illustrated in the bottom panels of Figure 2.11. However, at very low $N_{CO}/\Delta v$, the emission becomes optically thin (Figure 2.12), and only increased H_2 density will keep the CO in excited states. The Bayesian and χ^2 analyses both prefer optically thick line emission ($1 < \tau \lesssim 5$) for the three *detected* CO lines, even without enforcing the $\tau > 1$ prior. Requiring the undetected CO(7–6) line also to be optically thick imposes the cuts in parameter space seen in Figure 2.12. In this case, the best-fit models have $\tau \sim 1 - 2$ for the CO(7–6) line, and moderately optically thick emission ($1 < \tau < 15$) for the lower-J lines in the minimum χ^2 model compared to the highest probability model ($50 < \tau < 300$).

Given the degeneracies in LVG model parameters that can reproduce the blue component's line ratios, the best-fit models should be interpreted as rough estimates of the range of gas conditions that dominate the CO emission. Based on our results, the molecular gas in the blue component of J00266 is poorly constrained with $T_{kin} = 15 - 50\,K$, $n_{H_2} \lesssim 10^4\,cm^{-3}$, and $N_{CO}/\Delta v \gtrsim 10^{17}\,cm^{-2}\,km^{-1}\,s$. Barring additional line measurements to constrain acceptable LVG models, we consider additional priors. Requiring that the H_2

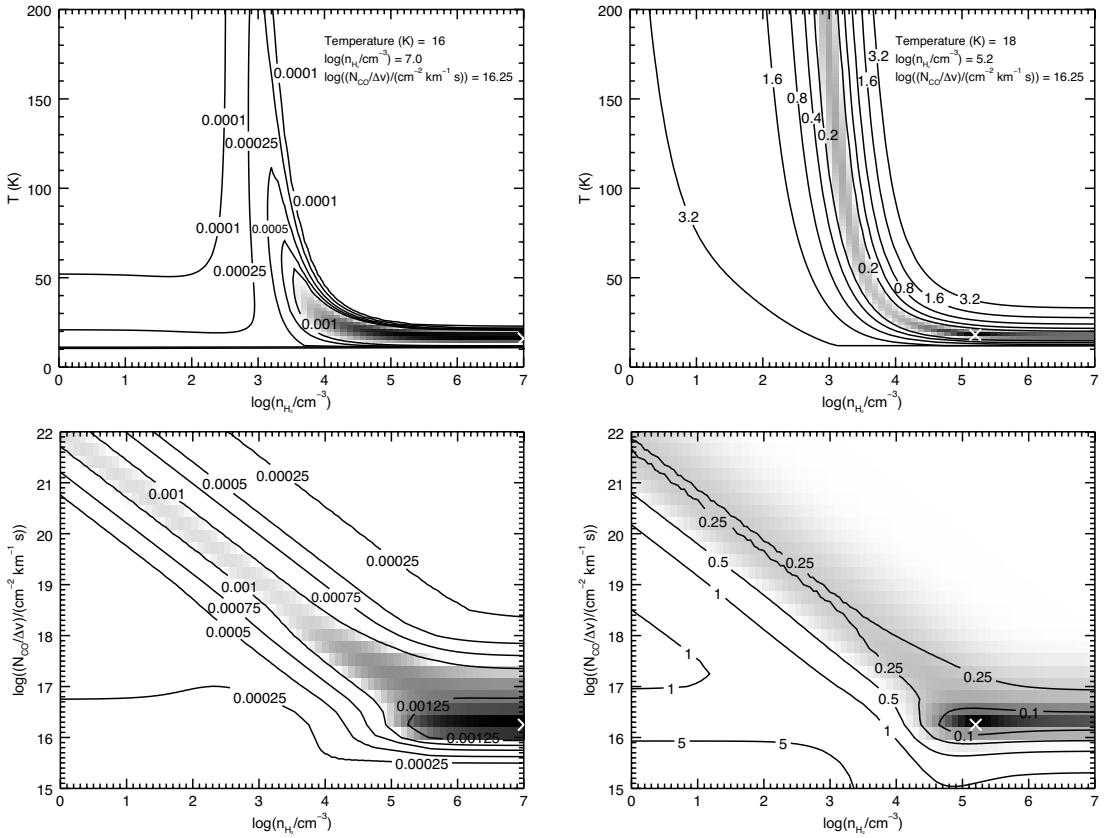

Figure 2.11 Probability contours (left column) and χ^2 contours (right column) for two slices through the best-fit models for the blue component: fixing the best-fit $N_{\rm CO}/\Delta v$ value (top row) and the best-fit temperature (bottom row). The best-fit model values are marked with white crosses, and the values are given in the top panel for each. The shading for the lowest contours is logarithmic to illustrate the shape of the parameter space where contours become unclear.

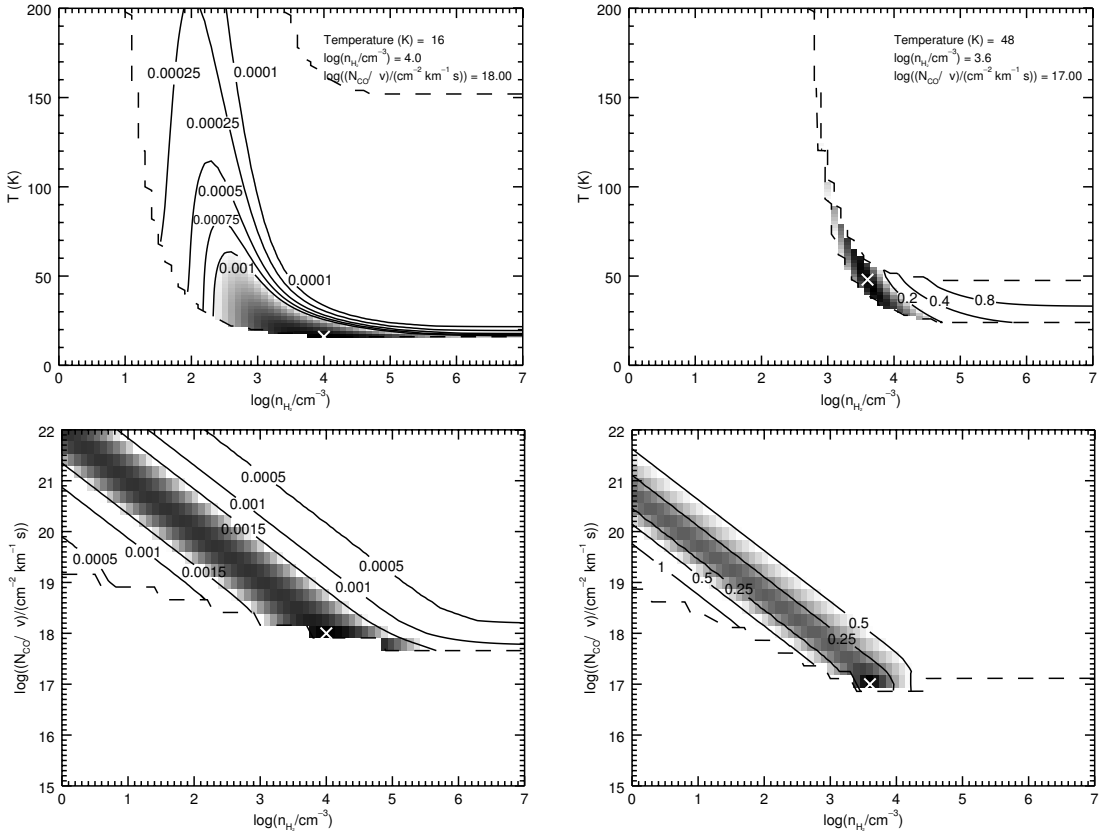

Figure 2.12 Probability contours (left column) and χ^2 contours (right column) for two slices through the best-fit models for the blue component, through the best-fit $N_{\rm CO}/\Delta v$ value (top row) and best-fit temperature (bottom row), after optically thin models have been removed. The best-fit model values are marked with white crosses, and the values are given in the top panel for each. The shading for the lowest contours is logarithmic to illustrate the shape of the parameter space where contours become unclear. Cuts imposed by the optical depth requirements are marked with the dashed line.

densities produce gas masses lower than the dynamical mass does not produce reasonable cuts on the H_2 density; the least stringent cut based on the blue component's dynamical mass and source size requires $n_{H_2} \lesssim 10^2\,\mathrm{cm}^{-3}$, lower than the observed density of molecular clouds in the Milky Way, which is likely not realistic. However, for the likely case that gas filling factor is not uniform (i.e., the blue component gas does not fill the volume we observe in projection), lower and more physically realistic gas masses are achievable. If the molecular gas in the blue component is virialized, then its cloud densities should produce $0.1 < K_{\mathrm{vir}} < 10$ (conservatively). Using the global velocity gradient defined by the line width and source size also limits the density to values below those of Milky Way-like clouds. Since both the priors on gas mass and virialization limit the H_2 density to unlikely regimes of parameter space, and both of these priors depend on the source size and velocity structure, we conclude that the assumed velocity gradient based on the *global* line measurements does not accurately describe the gas motions in the blue component, likely due to structure in the molecular gas that is below the resolutions of observations (Sharon et al. 2013a, similar to results for the SMG SMM J14011+0252 which also has $r_{3,1} \sim 1.0$;[).

The Red Component

The red component line ratios are very poorly fit by single-phase LVG models. The CO SLED for the minimum χ^2 model ($T = 12\,\mathrm{K}$, $n_{H_2} = 10^{5.4}\,\mathrm{cm}^{-3}$, and $N_{\mathrm{CO}}/\Delta v = 10^{17.25}\,\mathrm{cm}^{-2}\,\mathrm{km}^{-1}\,\mathrm{s}$) is shown in Figure 2.13; the single-phase model reasonably reproduces the CO(5–4)/CO(1–0) line ratio, but significantly overproduces CO(3–2) emission. The highest probability model from the Bayesian analysis has the same best-fit temperature and $N_{\mathrm{CO}}/\Delta v$, but prefers the highest allowed density, and produces a model SLED that is nearly identical to the minimum χ^2 model (Figure 2.13). As for the blue component, the best-fit models have $\tau > 1$ for the emission lines with $J_{\mathrm{upper}} \leq 5$, but optically thin emission for the CO(7–6) line ($\tau_{1-0} \sim 20$, $\tau_{3-2} \sim 50$, $\tau_{5-4} \sim 5$, and $\tau_{7-6} < 0.05$). If we restrict the possible parameter space to only models that produce optically thick line emission for all transitions, including CO(7–6), the minimum χ^2 value and highest probabilities are reached for the same parameters: $T = 12\,\mathrm{K}$, $n_{H_2} = 10^{3.6}\,\mathrm{cm}^{-3}$, and $N_{\mathrm{CO}}/\Delta v = 10^{18.75}\,\mathrm{cm}^{-2}\,\mathrm{km}^{-1}\,\mathrm{s}$.

For these models, the optical depths of the emission lines increase by a factor of 30, although there is little change in the predicted line ratios (Figure 2.13), and the model still provides a poor fit to the observed values. Forcing the models to match the CO(3–2) emission better (by removing the CO(5–4) line from the analysis) retrieves densities around $n_{\rm H_2} \sim 10^2\,{\rm cm}^{-3}$ and $N_{\rm CO}/\Delta v \sim 10^{17}\,{\rm cm}^{-2}\,{\rm km}^{-1}\,{\rm s}$. However, no model is able to produce a sufficiently low CO(3–2)/CO(1–0) line ratio. This limitation is an effect of including the CMB radiation in the LVG models; the CMB sets a floor on the CO level populations as a Boltzmann distribution at $T_{\rm CMB}(z = 2.742) = 10.2\,{\rm K}$, leading to preferred models at the lowest allowed temperature of 12 K. The inability of the single-phase model to reproduce the measured line ratios is also illustrated in Figure 2.14. These slices through LVG model parameter space along the best fit models clearly show two large regions where the probability is maximized and χ^2 is minimized; one region corresponds to model parameters that match the CO(3–2)/CO(1–0) line ratio but not the CO(5–4)/CO(1–0) ratio, while the other reproduces the CO(5–4)/CO(1–0) line ratio but not the CO(3–2)/CO(1–0) ratio. As the parameter regions both have long tails towards low temperatures and high densities, the latter region ends up being selected as the best-fit model regardless of how unphysical it may be.

Given the disappointing results of the single-phase analysis, we also consider a two-phase LVG model for the red component of J00266. Given the small number of line measurements relative to the number of parameters in the two-phase LVG analysis, and the number of degeneracies between model parameters, we can only constrain likely ranges of physical conditions as opposed to determining a single best-fit model. For the red component of J00266, we have also made use of several priors to restrict the allowed parameter space. For these models, in addition to the standard logarithmic prior for each parameter and the requirement $T > T_{\rm CMB} = 10.2\,{\rm K}$, we also require the emission to be optically thick for transitions with $J_{\rm upper} \leq 7$, the line brightness temperatures to be greater than $T_{\rm CMB}$, the CO column length to be less than the source diameter, and $K_{\rm vir} > 0.01$. For the cut on allowed column length, we conservatively use the major axis from the red component CO(3–2) detection and do not take into account the filling fraction for each component. This prior also requires assuming a value of the CO-to-H_2 abundance, for which we use

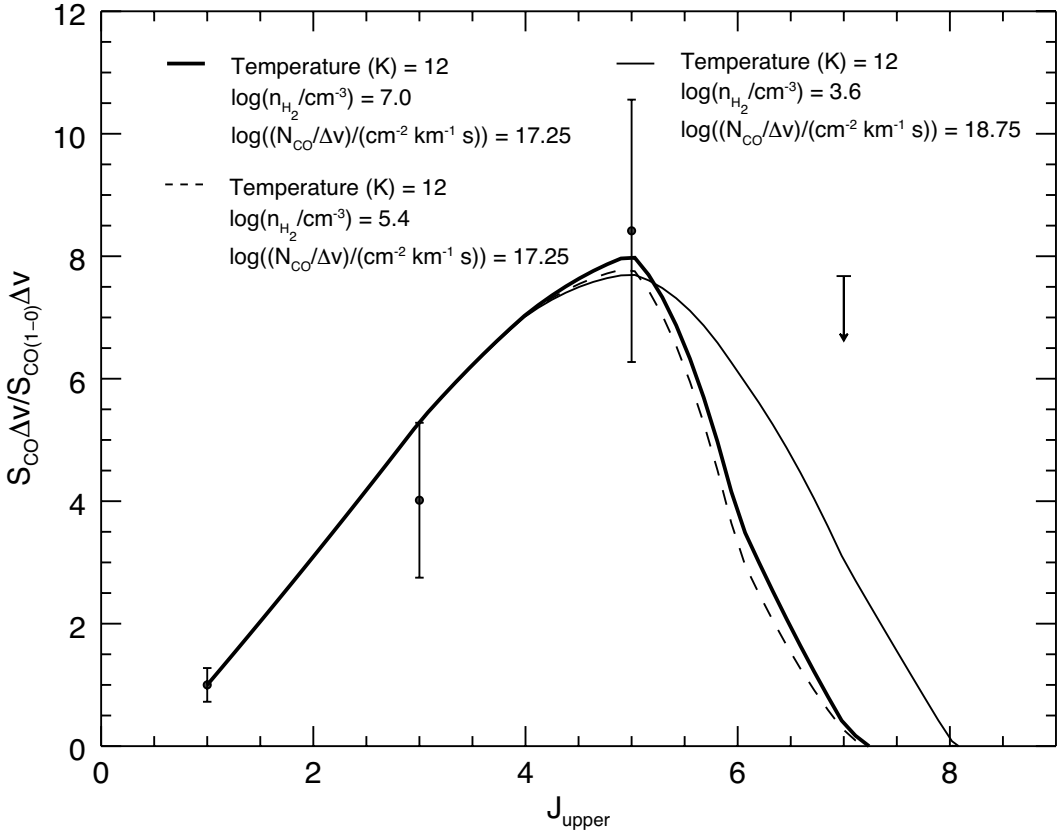

Figure 2.13 CO SLEDs for the best fitting single-phase models (lines) and the measured line ratios and 1σ errors (points) for the red component of J00266. The 3σ upper limit of the CO(7–6) line is given by the arrow. The thick solid line is for the highest probability model from the Bayesian analysis and the dashed line is for the minimum χ^2 model; in both cases the full parameter space of the LVG model is allowed except $T < T_{\rm CMB}$. The thin solid line is for the best-fit model (both maximum probability and minimum χ^2) when model parameters that produce optically thin emission are not allowed.

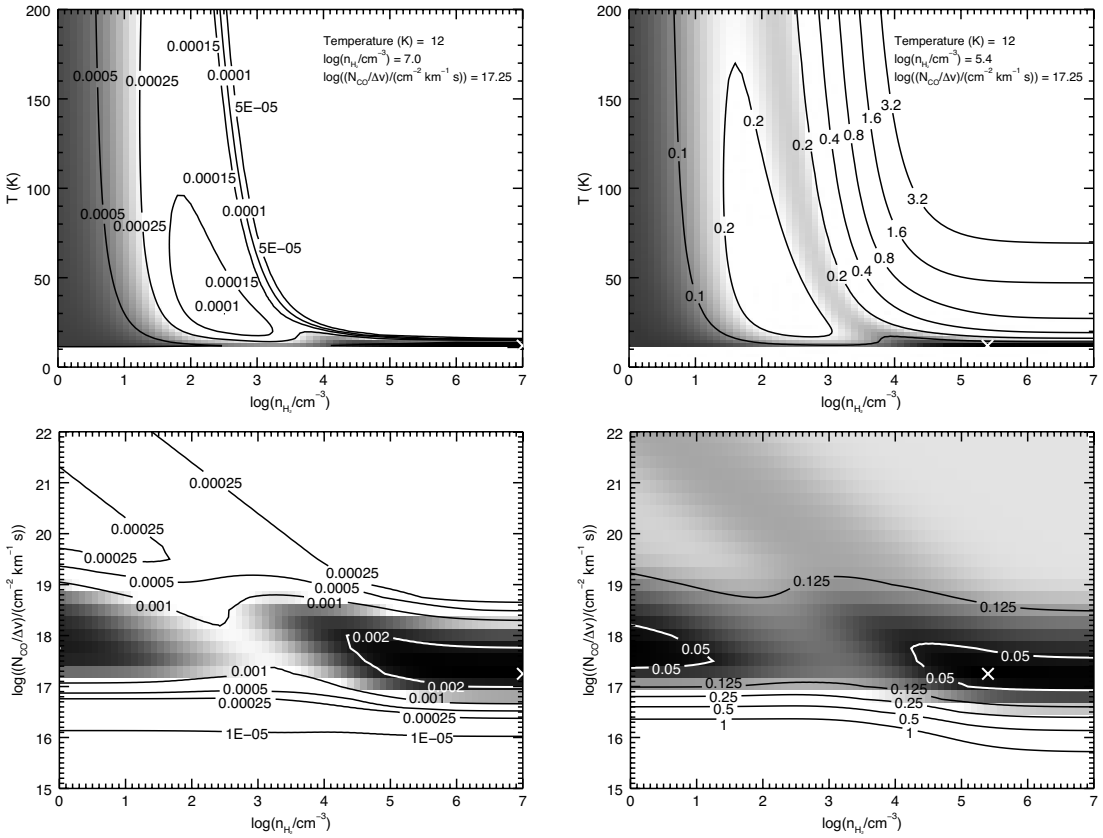

Figure 2.14 Probability contours (left column) and χ^2 contours (right column) for two slices through the best-fit single-phase models for the red component: fixing the best-fit $N_{\rm CO}/\Delta v$ value (top row) and the best-fit temperature (bottom row). The best-fit model values are marked with white crosses, and the values are given in the top panel for each. The shading for the lowest contours is logarithmic to illustrate the shape of the parameter space where contours become unclear.

$x_{\rm CO} = 10^{-4}$ as an upper limit. Using the measured FWHM of the red component, we find $N_{\rm CO}/\Delta v/n_{\rm H_2} < 10^{15.9}\,{\rm cm\,km^{-1}s}$ which does not eliminate any single value of the H_2 density or $N_{\rm CO}/\Delta v$ within the ranges probed, but does restrict combinations of those parameters. Similarly, we also choose a very conservative cut on the degree of virialization, $K_{\rm vir} > 0.01$ (since a diffuse phase does not have to be virialized, and stricter limits on $K_{\rm vir}$ tend to limit H_2 densities to unrealistic values) which eliminates $n_{\rm H_2} > 10^{4.54}\,{\rm cm^{-3}}$.

Since the requirement that defines the two phases, $T_{\rm c} < T_{\rm w}$, allows for *nearly* identical temperatures and the same ranges in density and $N_{\rm CO}/\Delta v$, there are significant degeneracies between the preferred parameters of the two phases, leading to favored models effectively consistent with a single phase. We therefore introduce an additional prior to help differentiate between the two phases. As the single-phase analysis produces two discrete regions of preferred parameter space depending on which of the two measured line ratios it best matches, one at low densities that matches the CO(3–2)/CO(1–0) line ratio and a second at high-densities that matches the CO(5–4)/CO(1–0) line ratio, we require that the cold phase H_2 density be less than the warm phase density. This prior is also motivated by the physical models proposed to explain the common $r_{3,1} \sim 0.6$ seen in other SMGs: small clouds of high density/excitation molecular gas are embedded within a larger volume filled with cold/low-density molecular gas (Harris et al. 2010; Ivison et al. 2011).

The results of the two-phase analysis are in Figures 2.15–2.18. Due to the large parameter space probed and the methods used, we are limited to analyzing marginalized distributions of LVG model parameters. The marginalized posterior probability distributions for the temperatures of the cold and warm phase molecular gas are shown in Figure 2.15. Both models are strongly peaked at the coldest temperatures, with the peak of the marginalized distribution of the cold phase at $T_{\rm c} = 14\,{\rm K}$ and the peak for the warm phase at $T_{\rm w} = 24\,{\rm K}$. Since the peak probability of the marginalized warm phase temperature distribution is lower than the probability at the same temperature for the cold phase, it is clear that the warm phase temperature is poorly constrained. It is most likely that the cold phase has $12\,{\rm K} < T_{\rm c} < 20\,{\rm K}$ and the warm phase has some higher temperature, albeit $< 100\,{\rm K}$. The cold and warm phase marginalized distributions for $n_{\rm H_2}$, the temperature vs. density plane, and the $N_{\rm CO}/\Delta v$ vs. density plane are shown in Figure 2.16. The

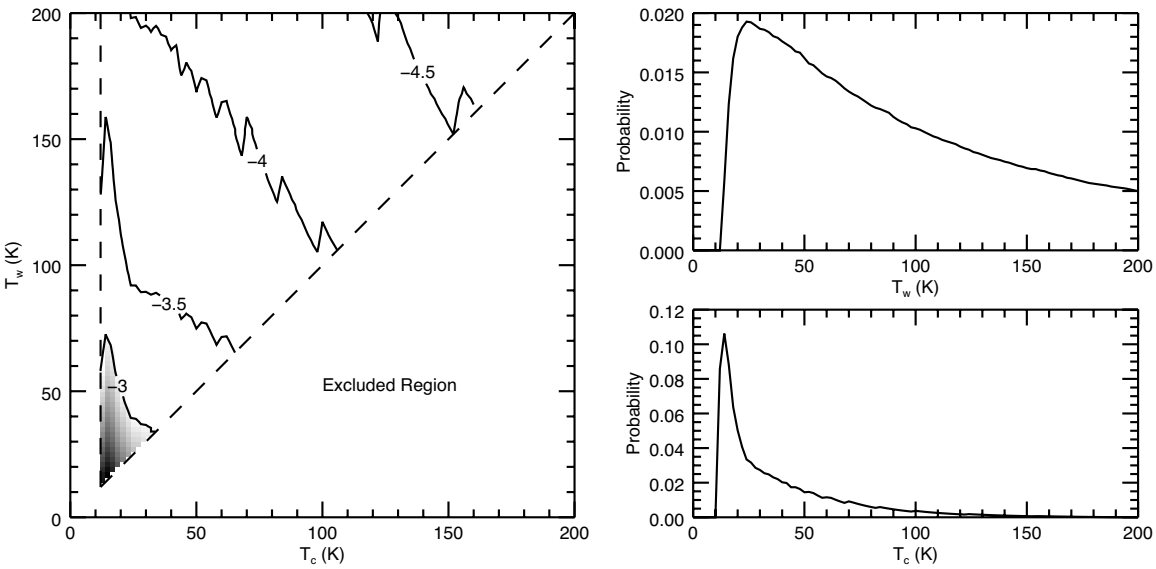

Figure 2.15 Marginalized posterior probability distributions for the temperatures of the cold and warm phase molecular gas in a two-phase model of the red component. The left panel show the marginalized distribution in the two-temperature plane with logarithmic shading/contours; the lower right half is eliminated by the requirement that $T_{\rm c} < T_{\rm w}$. The slight periodic jumps in the probability distribution are an artifact of the interpolation of the collision coefficients between temperatures.

marginalized posterior probabilities for the densities of the two phases appear choppy due to the coarse sampling of $N_{\rm CO}/\Delta v$; marginalizing over $N_{\rm CO}/\Delta v$ sums distributions in the temperature-density plane that have the characteristic "L"-shape seen in the single-phase models (Figure 2.12). Since the priors limit the H_2 density range to $\sim 10^2$–$10^4\,{\rm cm}^{-3}$, it is unsurprising that the additional prior of $n_{{\rm H}_2,\,{\rm c}} < n_{{\rm H}_2,\,{\rm w}}$ effectively divides this parameter range in half with $n_{{\rm H}_2,\,{\rm c}} \approx 10^2$–$10^3\,{\rm cm}^{-3}$ and $n_{{\rm H}_2,\,{\rm w}} \approx 10^3$–$10^4\,{\rm cm}^{-3}$. For $N_{\rm CO}/\Delta v$ (Figure 2.17), the cold phase probability peaks at $\sim 10^{18}\,{\rm cm}^{-2}\,{\rm km}^{-1}\,{\rm s}$ and the warm phase probability peaks at densities a factor of 5–10 higher, although with a broader probability distribution. The LVG model also constrains the ratio of the filling fractions (Figure 2.18). While the degeneracies still cause the probability distribution for the ratio of filling fractions to asymptote towards what is effectively a singe-phase model, we can estimate that $f_{\rm c}/f_{\rm w} \gtrsim 100$.

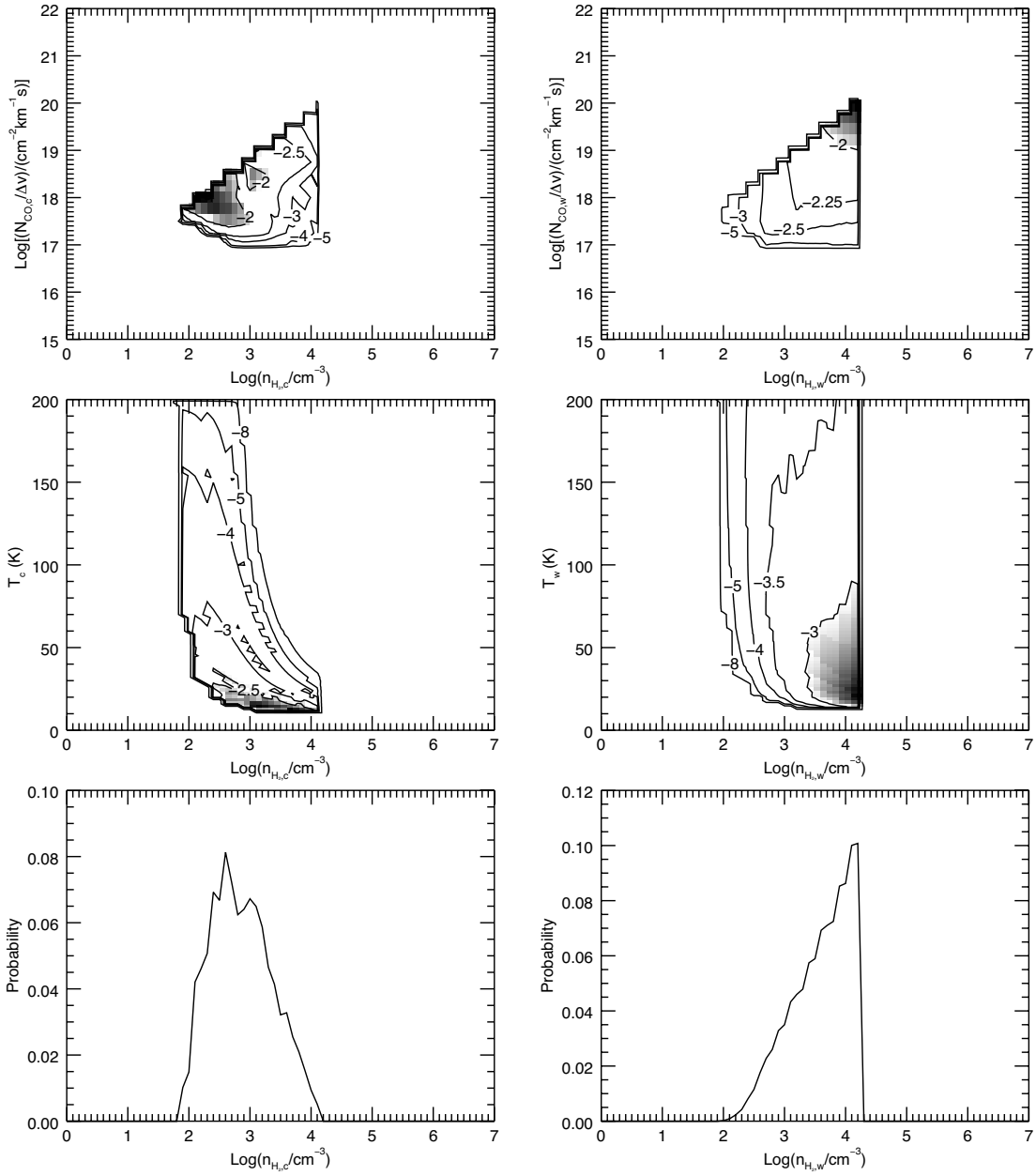

Figure 2.16 Marginalized posterior probability distributions for the densities of the cold phase (left column) and warm phase (right column) molecular gas in a two-phase model of the red component. The marginalized probability distributions of the $N_{\rm CO}/\Delta v$-density plane (top row) and temperature-density plane (middle row) have logarithmic shading and contours.

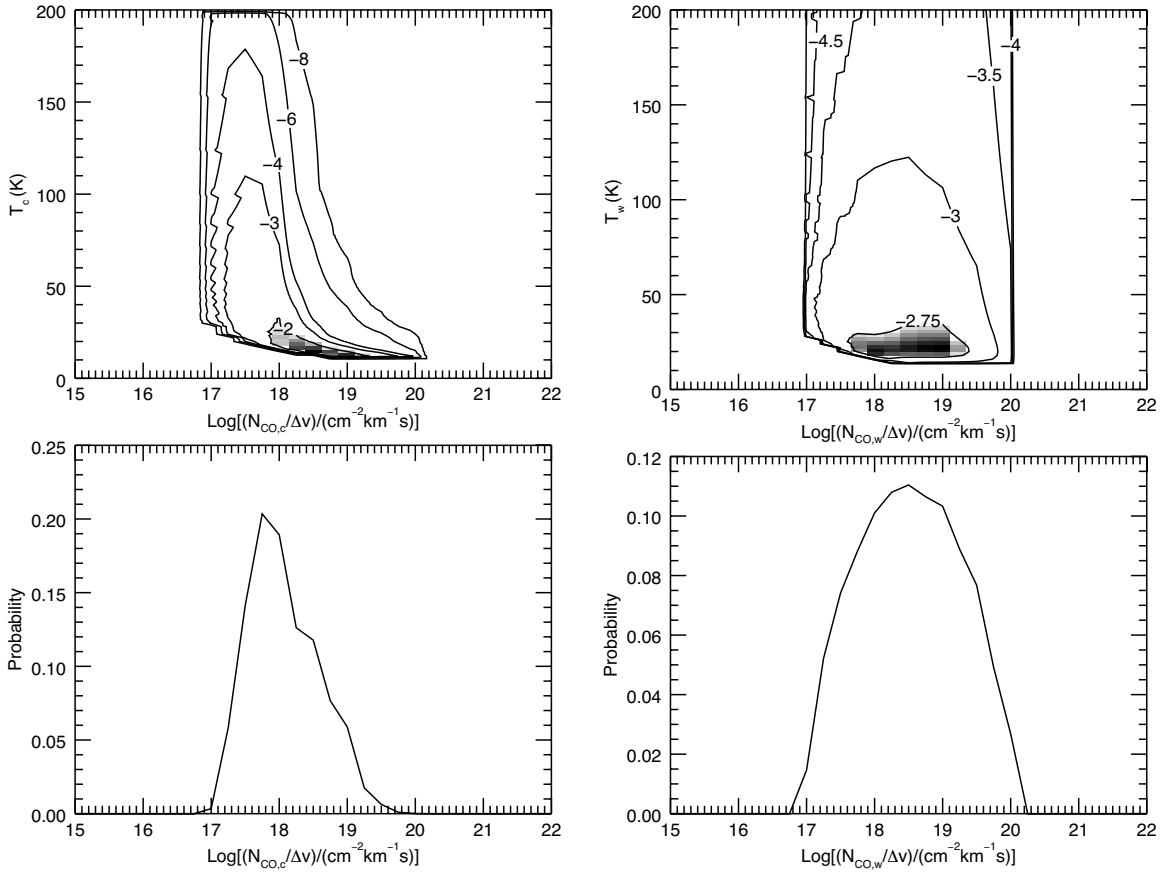

Figure 2.17 Marginalized posterior probability distributions for the cold phase $N_{\rm CO}/\Delta v$ (left column) and warm phase $N_{\rm CO}/\Delta v$ (right column) in a two-phase model of the red component. The marginalized probability distributions of the temperature-$N_{\rm CO}/\Delta v$ plane (top row) have logarithmic shading and contours.

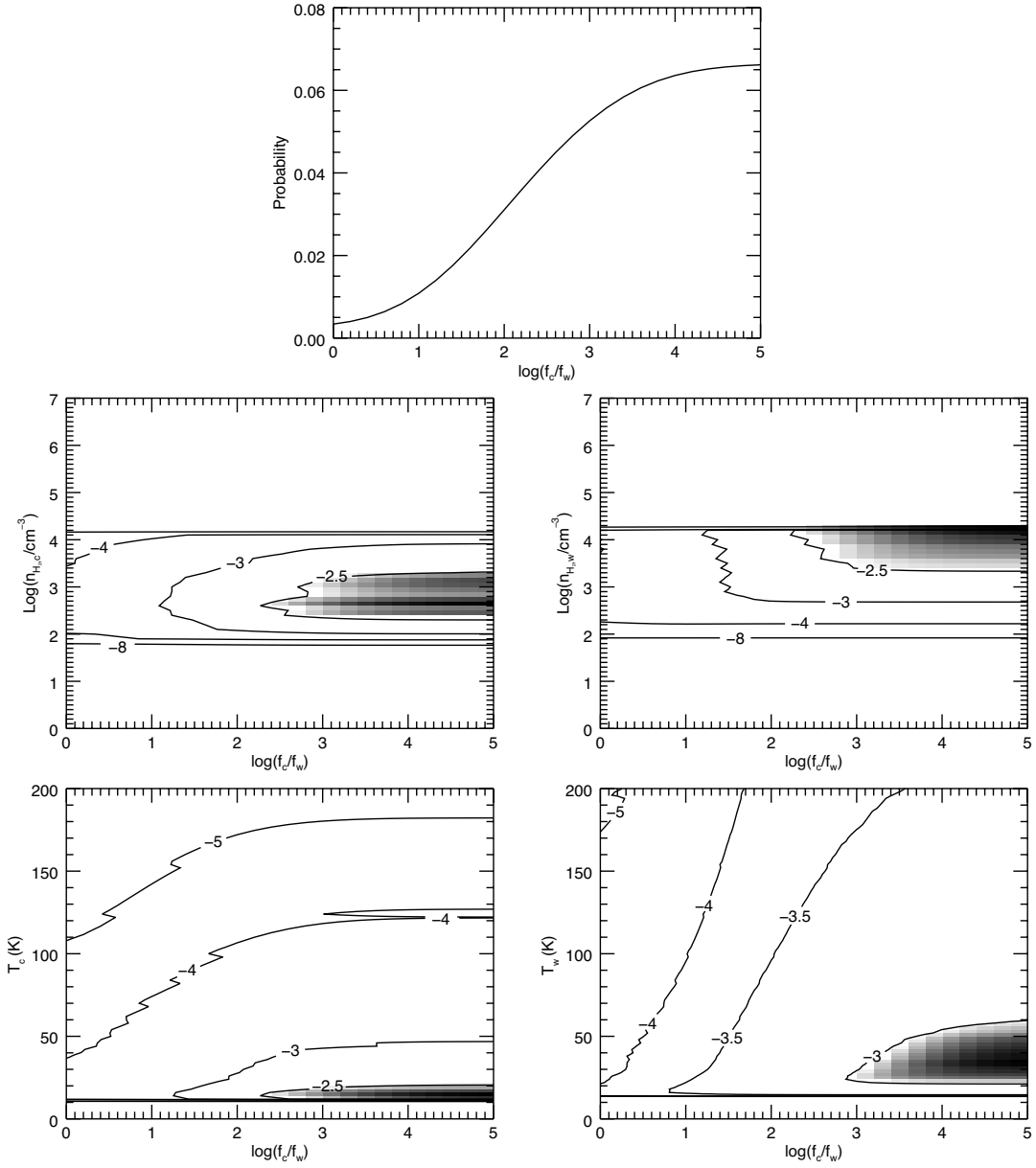

Figure 2.18 Marginalized posterior probability distributions for the ratio of the cold and warm phase filling fractions in a two-phase model of the red component. The marginalized probability distributions of the temperature-fraction plane (bottom row) and density-fraction plane (middle row) have logarithmic shading and contours.

2.4.3 CO to H_2 Abundance

Given the most likely parameter ranges for the molecular gas in J00266 implied by the LVG analysis, we can determine the CO abundance factor relative to H_2, $x_{CO} = (N_{CO}/\Delta v) \times (\Delta v/l)/n_{H_2}$, where l and Δv are the globally determined average column length through the source and line width as estimated from our observations. For the two-phase model, we can either treat each phase separately, thus allowing for variations in the CO abundance, or we can create a weighted average using the filling factors:

$$x_{CO} = \frac{f_c N_c/\Delta v + f_w N_w/\Delta v}{f_c n_c + f_w n_w} \left(\frac{\Delta v}{l}\right). \tag{2.2}$$

For the blue component, which is consistent with a single-phase model, the range of best-fit models (maximum probability or minimum χ^2, with or without the optical depth requirement) produce $x_{CO} \sim 10^{-11}$–10^{-7}. The single-phase red component models produce a similarly broad range, $x_{CO} \sim 10^{-10}$–10^{-5}. For both components, the models with the optical depth requirements tended to produce CO abundances on the lower end of these ranges. These abundances are also extremely low; typical assumptions elsewhere in the literature are $x_{CO} \sim 10^{-4}$. It is likely that the *global* velocity gradients of the two components do not accurately describe the kinematic structures within the system; this was already hinted by the unphysical restrictions on the blue component parameter space for priors that used the galaxy-wide value of the velocity gradient. The global velocity gradient may fail to describe the gas motions if the two components of J00266 posses smaller clouds that are not resolved by our PdBI observations. Unresolved velocity structure as implied by the unphysical results from analyzing LVG models with global velocity gradients has also been seen in another SMG, SMM J14011+0252 (Sharon et al. 2013a), which suggests that the failure of global velocity gradients to accurately describe the gas physical conditions may be common among SMGs. For the two-phase LVG analysis of the red component, it is difficult to estimate the CO abundance due to the broad range of parameters allowed by the LVG analysis. Using the mean values of the ranges given in Section 2.4.2, and the minimum value of $f_c/f_w \sim 100$, we estimate $x_{CO} \sim 4 \times 10^{-5}$, which is in line with expected abundances.

In many other LVG analyses, instead of using $N_{\rm CO}/\Delta v$ to quantify the crucial "large velocity gradient" that simplifies analysis of optically thick emission, authors use $x_{\rm CO}/(\Delta v/\Delta r)$. The CO abundance per unit velocity gradient, which we effectively calculate above if we leave off the factor of the (potentially problematic) measured velocity gradient, is often assumed to be $10^{-5}\,(\mathrm{km\,s^{-1}})^{-1}\,\mathrm{pc}$, since models that vary $x_{\rm CO}/(\Delta v/\Delta r)$ by an order of magnitude do not seem to produce very different line ratios. While this assumed value is within the ranges possible for the red and blue components, fixing $x_{\rm CO}/(\Delta v/\Delta r)$ ignores substantial degeneracies between the physical parameters used in the LVG model and can produce artificially accurate best-fit results. Higher resolution observations are necessary in order to accurately determine local velocity gradients in SMGs, which will allow LVG models to capture more realistic values and uncertainties for the physical conditions of the molecular gas.

2.4.4 Star formation properties

As most characterizations of J00266 made at other wavelengths have not resolved the source (spatially or spectrally), it is difficult to derive separate parameters for its two components. For example, the low resolution of the *Spitzer*/IRS spectrum Valiante et al. (2007) does not allow us to use the velocity offset in the two components to distinguish between their contributions to the 7.7 μm PAH feature. Likewise, Valiante et al. (2007) use an SED fit to determine $T_{\rm dust} = 35.3\,\mathrm{K}$, but we cannot say how the two components' dust temperatures may differ from this value because we do not know how much of each of the two components contributes to the continuum flux measurements. However, as the *Spitzer*/IRS spectrum contains both AGN signatures (continuum) and star formation signatures (PAH emission), the mid-IR is consistent with J00266 comprising a merger between two very different galaxies (based on the QSO-like and SMG-like line ratios of the blue and red components, respectively).

If we assume FIR luminosity traces star formation, and that the star formation rate is proportional to the gas mass with a power law index of $n \sim 1$–1.5, we can use the ratio of the CO(1–0) line fluxes to estimate the star formation rates (SFRs) in the two components. Assuming the Kennicutt (1998) conversion factor (corrected to the Calzetti

et al. (2007) initial mass function), and our new magnification factor, the SFRs of the blue and red components are 174 and 570 $M_\odot\,\mathrm{yr}^{-1}$, respectively (for $n = 1$), or 107 and 637 $M_\odot\,\mathrm{yr}^{-1}$ for $n = 1.5$. Using the source sizes and gas masses of the two components, we can place the two components of J00266 on the Schmidt-Kennicutt relation (Schmidt 1959; Kennicutt 1998) using average values of the SFR surface density and molecular gas surface density. For the both components we assume the de-lensed source sizes given by the Gaussian fits to the CO(3–2) emission. The blue component average SFR surface density is 5.6 $M_\odot\,\mathrm{km\,s^{-1}\,kpc^{-2}}$ ($n = 1$) or 3.4 $M_\odot\,\mathrm{km\,s^{-1}\,kpc^{-2}}$ ($n = 1.5$), and the gas mass surface density is $10^{2.8}(\alpha_{\mathrm{CO}}/0.8)\,M_\odot\mathrm{pc}^{-2}$. The red component SFR surface density is approximately a factor of ten larger: 14–16 $M_\odot\,\mathrm{km\,s^{-1}\,kpc^{-2}}$ for $n = 1.0$–1.5. The average gas mass surface density for the red component is $10^{3.2}(\alpha_{\mathrm{CO}}/0.8)\,M_\odot\mathrm{pc}^{-2}$. Both the blue and red components of J00266 fall among the starburst galaxies of Kennicutt (1998), regardless of our choice in star-formation index. The components remain among the starburst galaxies for different choices of α_{CO} as well. The apparent division between the "starburst sequence" and the "disk galaxy sequence" in the Schmidt-Kennicutt relation (e.g., Daddi et al. 2010; Genzel et al. 2010) has been argued to be an artificial product of the bi-modal choice in α_{CO} for those two populations (e.g., Narayanan et al. 2012), however the position of the two components of J00266 appears to be robust to the choice in conversion factor.

2.5 Discussion

In the growing sample of well-studied SMGs, close examination of galaxies with peculiar gas conditions may help us understand the origin of the average populations characteristics and possibly the evolutionary connection between SMGs and other high-redshift galaxies (which have different gas conditions). The difference in kinematics and line ratios in the two velocity-offset components of J00266 makes it a clear member of the population of SMGs that are ongoing mergers (e.g. Tacconi et al. 2008; Engel et al. 2010; Riechers et al. 2011c; Karim et al. 2012; Riechers 2013). J00266 is (so far) a unique merger inasmuch as the excitation conditions differ between the two merging components. Riechers et al. (2011c) also report CO(1–0) observations of a merging SMG. As for J00266, the two components of SMM J123707+6214 differ in terms of line width and velocity structure. However, the line

ratios of the two components are similar, with CO(3–2)/CO(1–0) line ratios significantly below the SMG average ($r_{3,1} = 0.39 \pm 0.09$ and 0.37 ± 0.10, more in line with $z \sim 1.5$ BzK galaxies; e.g., Dannerbauer et al. 2009; Aravena et al. 2010). Riechers (2013) also reports a candidate "wet-dry" merger between an SMG and a quasar, where the molecular gas emission from the quasar host galaxy has not been detected and the galaxy pair are widely separated compared to the component separation in J00266 (41.5 kpc in projection and $700\,\mathrm{km\,s^{-1}}$ in velocity). J00266 also has extremely high obscuration being fainter in K band than all other IRAM CO-detected SMGs in Frayer et al. (2004). While high obscuration is generally consistent with U/LIRG-like FIR luminosities and simulations that indicate SMG are especially dust-bright during major mergers (and when viewed in the correct orientation; e.g., Narayanan et al. 2010), this distinction in obscuration for J00266 is not mirrored in other probes of its dust content (with a relatively moderate $L_{\mathrm{FIR}} = 5 \times 10^{12}\,L_{\odot}$ for a SMG; Valiante et al. 2007). While it is difficult to assess where J00266 falls on proposed evolutionary tracks for SMGs (e.g., Narayanan et al. 2010), the high obscuration and moderate L_{FIR} suggests that J00266 is in the early stages of merging, and that the dust screen geometry is playing a significant role in its observed properties (rather than peculiarly large dust mass, which would be expected to produce a large L_{FIR}). Since CO observations of many SMGs relied on optically determined spectroscopic redshifts (e.g., Chapman et al. 2005), it may be that the unique properties of J00266 are representative of a class of heavily obscured objects that would not have been detected in studies that rely on optical counterpart identification, biasing our conclusions about the SMG population characteristics. Testing this hypothesis requires followup CO observations of submillimeter-bright objects that have not relied and on radio and optical counterparts for their redshift measurements (e.g., Harris et al. 2012; Vieira et al. 2013) or more deliberate followup of SMGs where optical spectroscopy failed to measure the redshift (e.g., Chapman et al. 2005).

The correspondence of the different kinematics with different ISM conditions in J00266 is suggestive; disk galaxies at other redshifts seem to have a multi-phase molecular ISM, while quasar host galaxies might be expected to have funneled all their gas into a compact central region (making velocity gradients difficult to resolve) that is well-described by a single phase. However, galaxies with ordered motion and $r_{3,1} \sim 1$ that lack an AGN component have been

observed among local U/LIRGs, making a strict gas excitation-dynamics connection unlikely without some fundamental difference between low- and high-redshift U/LIRGs. At high-redshift, the SMG SMM J14011+0252 appears to be an exception to many SMG trends, including a potential excitation-dynamics connection since it contains a velocity gradient (albeit a weak one), $r_{3,1} \sim 1$, and no AGN (Sharon et al. 2013a).

Interpretation of the kinematics from often low-resolution observations of CO has made answering the question of SMGs' structure (i.e., merger-driven starbursts or star-forming disks) difficult; velocity gradients and double-peaked line profiles could arise from either ordered rotation or a merger. Hayward et al. (2013) propose that submillimeter-bright galaxies are a heterogeneous sample containing disks, galaxy pairs (coincidently caught within the large beams of most single dish submillimeter telescopes), and mergers (see also Karim et al. 2012). They find that the relative contribution of each population to the number counts varies with the millimeter and submillimeter flux, where mergers and galaxy pairs dominate at the high flux end. J00266, a merging system with $S_{850\,\mu\mathrm{m}} = 10.6 \pm 1.4\,\mathrm{mJy}$ (magnification corrected), is in line with these predictions. However, the SMG GN20 has a significantly larger submillimeter flux ($20.3 \pm 2.1\,\mathrm{mJy}$; Pope et al. 2006), well into the regime where mergers are expected to dominate the population, and is a massive ($M_{\mathrm{H_2}} = 1.3 \pm 0.4 \times 10^{11} (\alpha_{\mathrm{CO}}/0.8)\,M_{\odot}$) $z = 4.05$ disk galaxy (Hodge et al. 2012). The contrasting structures of J00266 and GN20 certainly highlight the heterogeneity of the SMG population, but muddy evolutionary explanations of large FIR luminosities.

2.6 Summary

We present CO observations of the SMG SMM J00266+1708 and provide the first spectroscopic measurement of its redshift ($z = 2.742$). Based on CO(3–2) and CO(5–4) observations from the PdBI, we find that J00266 has two distinct components separated by $\sim 500\,\mathrm{km\,s^{-1}}$ and closely aligned along our line of sight. The two components of J00266 appear to have different kinematics, with the blue-shifted component (relative to the line center) having dispersion-dominated kinematics and the red-shifted component showing a clear velocity gradient. The CO line ratios also vary between the two components, indicating that the gas physical conditions are not alike. Based on the components' differing kinematics and line

ratios, we conclude that J00266 is a merger with a mass ratio of $(7.7 \pm 3.9)/\sin^2(i)$. The internal variation of excitation conditions in a two-component SMG has not been observed in other objects so far. J00266 serves as an example of the diversity of galaxy types that comprise submillimeter-selected sources, and is a clear example of an ongoing merger in a SMG.

We have performed LVG analyses of the CO line ratios in order to constrain the physical conditions of the two components. We find that the line ratios of the blue component are consistent with a single-phase molecular ISM with $T_{\rm kin} = 15 - 50\,{\rm K}$, $n_{\rm H_2} \lesssim 10^4\,{\rm cm^{-3}}$, and $N_{\rm CO}/\Delta v \gtrsim 10^{17}\,{\rm cm^{-2}\,km^{-1}\,s}$. The red component is *not* consistent with a single-phase molecular ISM; similar to many other SMGs, it appears to have a substantial cold gas reservoir. We attempt a two-phase LVG model for the red component, but with a limited number of line measurements (three plus an additional upper limit) relative to the number of free parameters (seven), the results are highly degenerate. We constrain the cold phase temperature to be between 12–20 K and the warm phase at some higher temperature $< 100\,{\rm K}$. We find that the H_2 density of the cold phase is $n_{\rm H_2,\,c} \approx 10^2$–$10^3\,{\rm cm^{-3}}$ and the warm phase has $n_{\rm H_2,\,w} \approx 10^3$–$10^4\,{\rm cm^{-3}}$. We also find $N_{\rm CO,\,c}/\Delta v \sim 10^{18}\,{\rm cm^{-2}\,km^{-1}\,s}$, while the warm phase probability peaks at columns a factor of 5–10 greater. The ratio of the cold-to-warm phase filling factors is constrained to be $f_{\rm c}/f_{\rm w} \gtrsim 100$.

Chapter 3

SMM J14011+0252

3.1 Background

We have obtained high-resolution VLA mapping of the CO(1–0) line in SMM J14011+0252 (J14011 hereafter), which we compare to previous mid-J and rest-frame mid-IR observations. J14011 ($z_{\rm opt} = 2.55$; Barger et al. 1999) was discovered as part of the SCUBA Lens Survey (Smail et al. 1998, 2002); it consists of two optical/near-IR components in the source plane (J1 and J2) that are weakly gravitationally lensed by the cluster A1835 ($z = 0.25$) and one of its members (J1c; Motohara et al. 2005), with a median magnification factor of $\mu \sim 3.5 \pm 0.5$ (Smail et al. 2005). Since its discovery, J14011 has been followed up extensively with optical and near-IR observations (Barger et al. 1999; Ivison et al. 2000, 2001; Tecza et al. 2004; Frayer et al. 2004; Swinbank et al. 2004; Motohara et al. 2005; Nesvadba et al. 2007), and it was only the second SMG to be successfully detected in any CO transition (CO(3–2); Frayer et al. 1999). Further CO(3–2) observations were made by Ivison et al. (2001), as were CO(3–2) and CO(7–6) observations by Downes & Solomon (2003). Strong upper limits on its X-ray flux (Ivison et al. 2000; Fabian et al. 2000; Rigby et al. 2008) and ratios of the 7.7 μm polycyclic aromatic hydrocarbon (PAH) feature to mid-infrared flux (Rigby et al. 2008) indicate that J14011 is a pure starburst, lacking a significant contribution to its dust luminosity from an active galactic nucleus (AGN). It is similar in its far-infrared luminosity ($L_{\rm FIR} \sim 4 \times 10^{12}\,L_{\odot}$; Smail et al. 2005) and its clumpy morphology within and between optical/near-IR components (Ivison et al. 2000; Tecza et al. 2004; Swinbank et al. 2004) to low-redshift ultra/luminous infrared galaxies (U/LIRGs) such as Arp 220 (Frayer et al. 1999; Ivison et al. 2000; Downes & Solomon 2003; Motohara et al. 2005; Nesvadba et al. 2007; Rigby et al. 2008). Initial single-dish observations of the CO(1–0) line indicated $r_{3,1} = 0.76 \pm 0.12$ (Harris et al. 2010), similar to the values seen for other SMGs.

3.2 Observations

We observed J14011 (α(J2000) = $14^{\rm h}01^{\rm m}4.^{\rm s}93$, δ(J2000) = $+02°52'24.1''$; CO(3–2) position from Downes & Solomon 2003) at the VLA on 2010 October 1 and 3 in the DnC configuration (maximum baseline 1.868 km) and 2011 January 22, 25, and 28–31 in the CnB configuration (maximum baseline 6.903 km). During the DnC observations, 23 antennas were functioning and equipped with Ka-band receivers, and the weather conditions were mixed (< 70% sky coverage by cumuliform clouds). During the CnB observations, 26 Ka-band-equipped antennas were available, and the weather conditions were excellent. We observed with the WIDAR correlator in the "OSRO Full Polarization" mode using the lowest available spectral resolution (64 channels × 2 MHz resolution). The intermediate frequency (IF) channel pairs A/C and B/D were tuned to overlap by 10 channels, creating a full bandwidth of 236 MHz centered at 32.3703 GHz (chosen to keep the line away from IF pair edges). At the beginning of each track we observed 3C286 as a flux calibrator, adopting S_ν = 1.9455 Jy as the CASA package's default "Perley-Butler 2010" flux density. Phase and amplitude fluctuations were tracked by alternating between the source and a nearby quasar, J1354–0206, with a cycle time of 6 minutes; this quasar was also used for passband calibration. A total of 18.7 hr was spent on source.

Calibration and mapping were carried out in CASA. After the tracks had been corrected for Doppler shifts relative to the local kinematic (radio) standard of rest using the CASA routine cvel, the original channels were smoothed by a factor of two, resulting in 4 MHz (37 km s^{-1} rest frame) spectral resolution. The naturally weighted channel maps have a synthesized beam of $0.''68 \times 0.''52$ at position angle $119^{\circ}.02$ and an average rms noise of 53.2 μJy beam^{-1}. Analysis of the resulting data cube was performed using a custom set of IDL scripts.

3.3 Results

Our spectrum (Figure 3.1) successfully detects the CO(1–0) line at the 8σ level. A Gaussian fit to our line profile gives a peak flux density of 2.08 ± 0.22 mJy and an FWHM of 151 ± 19 km s^{-1}. The FWHM is consistent with the CO(7–6) line width of 170 ± 30 km s^{-1},

and marginally narrower than the CO(3–2) line width of $190 \pm 11\,\mathrm{km\,s^{-1}}$ from Downes & Solomon (2003). The integrated CO(1–0) line flux (using the seven channels around the line peak) is $0.32 \pm 0.03(\pm 0.03)\,\mathrm{Jy\,km\,s^{-1}}$, where the latter 10% uncertainty is associated with the flux calibration. While our measured integrated line flux appears to be lower than the $\sim 0.40 \pm 0.05\,\mathrm{Jy\,km\,s^{-1}}$ of Harris et al. (2010), the two values are consistent within their 1σ errors. The slight discrepancy is likely because the Zpectrometer-measured value is from a Gaussian fit in which the line width is only an upper limit (the narrow line was marginally spectrally resolved by the Zpectrometer). Convolution of the VLA spectrum with the 20 MHz FWHM sinc(x) response function of the Zpectrometer reproduces the Gaussian fit integrated line flux given in Harris et al. (2010), indicating that our measurements are in good agreement when we account for spectral resolution differences. Using the Milky Way conversion factor $\alpha_{\mathrm{CO}} = 4.6\,M_{\odot}\,(\mathrm{K\,km\,s^{-1}\,pc^2})^{-1}$ (Solomon & Barrett 1991) suggested by our large velocity gradient (LVG) analysis (Section 3.4.1) and correcting for lensing magnification and helium, the molecular gas mass is $(1.9 \pm 0.3) \times 10^{11}\,M_{\odot}$. The redshift as determined by our CO(1–0) measurement is $z = 2.5653 \pm 0.0001$, which is consistent with the previous optical (e.g., Barger et al. 1999; Ivison et al. 2000) and CO (e.g., Downes & Solomon 2003; Harris et al. 2010) redshifts.

The integrated intensity map (Figure 3.2) shows that the CO(1–0) emission is spatially extended in a northeast/southwest direction, parallel to the lensing shear (Smail et al. 2005), and contains two peaks embedded within more extended emission, similar to those seen in Hα (Tecza et al. 2004). The center of the CO(1–0) line emission is consistent with the peak positions of the CO(3–2) and CO(7–6) lines previously detected by Downes & Solomon (2003) (Figure 3.3), with $\sigma_{1-0} = 0.''05$ based on an elliptical Gaussian fit in the image plane and the intrinsic uncertainty of the phase calibrator position. The Gaussian fit gives a major axis FWHM of $2.''6 \pm 0.''1$ at position angle $18^{\circ}.7 \pm 1^{\circ}.3$ and a minor axis FWHM of $0''.8 \pm 0.''1$ when accounting for the beam size. As J14011 is lensed, these dimensions do not easily translate into rest-frame physical dimensions. While the line FWHM is quite narrow, the CO(1–0) emission does show a velocity gradient. In Figure 3.4, we plot overlaid channel maps of the red and blue halves of the central $200\,\mathrm{km\,s^{-1}}$ of CO(1–0) line as well as the same velocity ranges for the Hα integral field data presented in Tecza et al. (2004).

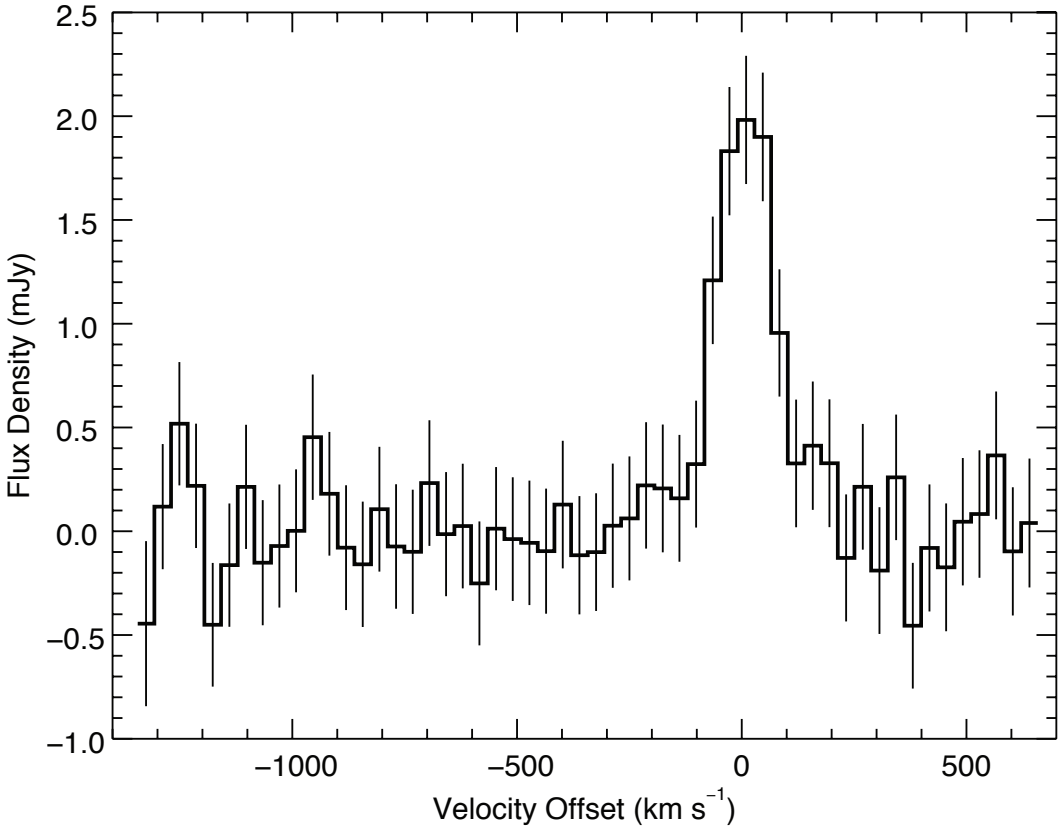

Figure 3.1 37 km s^{-1} resolution VLA spectrum plotted relative to the $z = 2.5652$ CO(1–0) systemic redshift from the GBT/Zpectrometer observations (Harris et al. 2010). Vertical lines indicate 1σ statistical uncertainties.

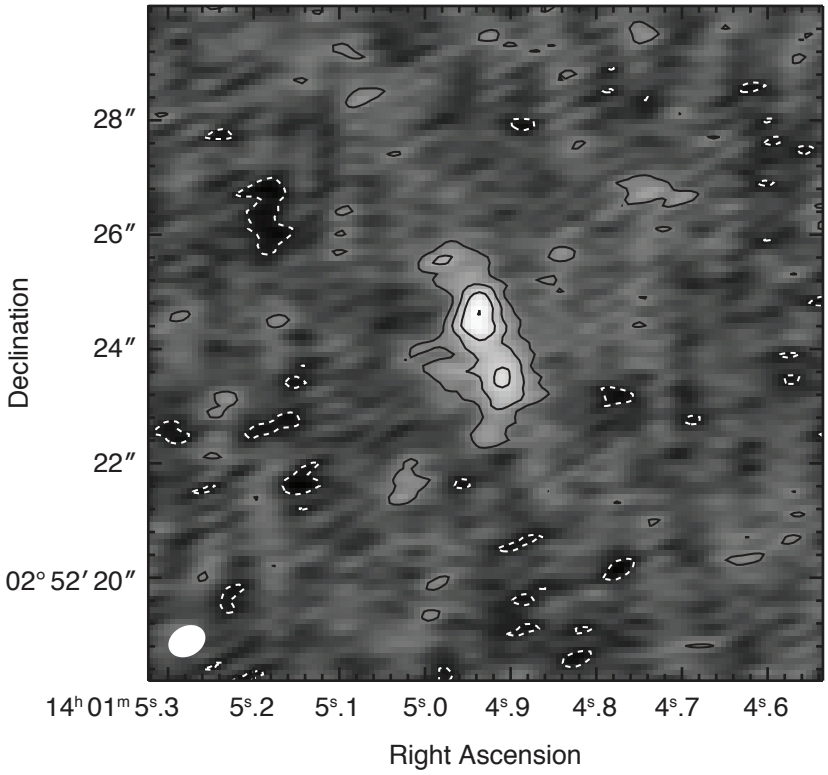

Figure 3.2 Integrated CO(1–0) intensity map. Contours are multiples of $\pm 2\sigma$ (σ = 0.16 mJy beam^{-1}), where negative contours are dotted; synthesized beam is shown at lower left.

The red and blue halves of both lines are slightly offset in similar directions, with the two peaks in the integrated line maps apparently dominated by emission at different velocities. In Figure 3.5, we show a CO(1–0) position-velocity diagram for J14011 for a position angle of $75^\circ \pm 5^\circ$ that maximizes the velocity gradient.

We do not detect any significant continuum emission from J14011 in the (rest-frame) 2.6 mm continuum map produced from the line-free channels. We estimate a 3σ upper limit for the continuum emission of 26.7 μJy for a point-like source, or 157 μJy when scaled to the dimensions of the CO(1–0) emission.

In order to compare the CO(1–0) emission to existing optical and infrared data, we have taken care in aligning images. Based on the source sizes and structures in the two sets of maps in Figure 3.4, and the fact that Hα emission from HII regions is expected to follow molecular gas at this linear resolution, we can use the positions of the northern and southern

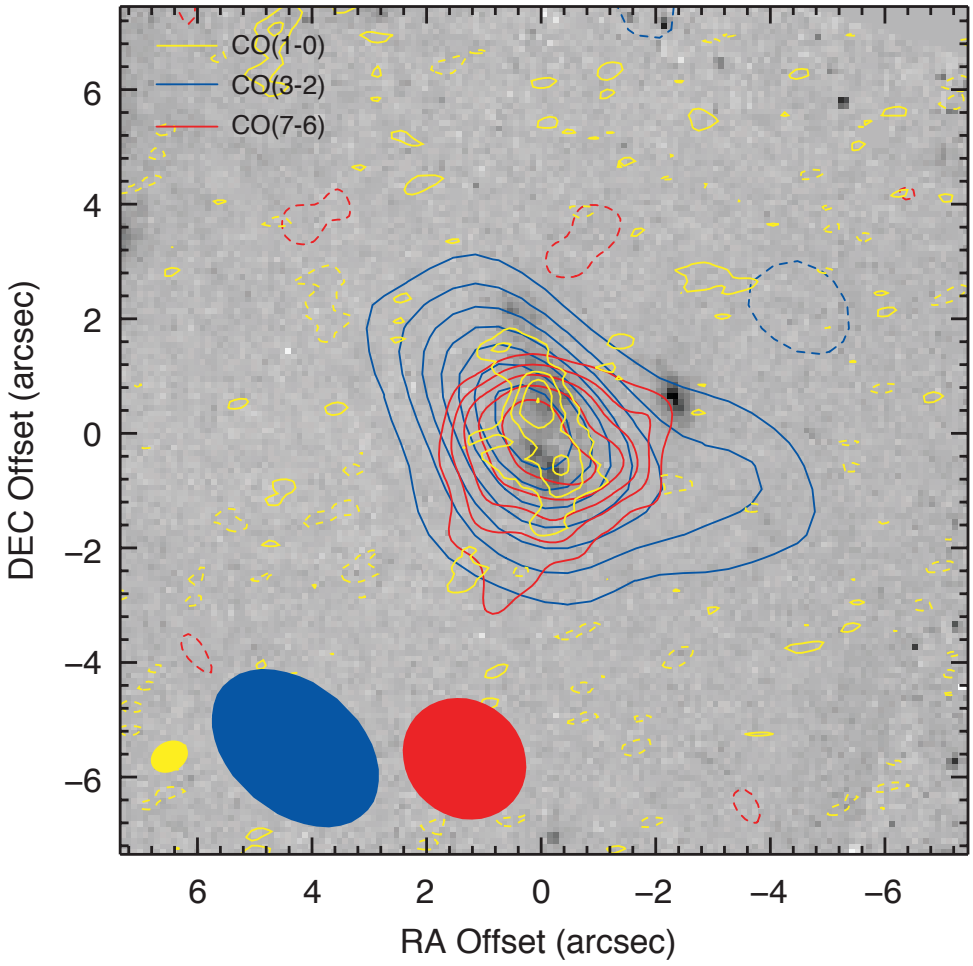

Figure 3.3 Overlaid contours of all published CO maps of J14011 and the Aguirre et al. (2013) *HST* F160W image (with the foreground interloper, J1c, removed), centered at α(J2000) = $14^{\rm h}01^{\rm m}04.^{\rm s}93$ and δ(J2000) = $+02°52'24.''1$. The CO(1–0), CO(3–2), and CO(7–6) maps are in yellow, blue, and red respectively; the synthesized beam for each map is shown by the filled ellipse of the corresponding color in the lower left corner. The CO(1–0) line contours are as described in Figure 3.2. The CO(3–2) and CO(7–6) observations are taken from Downes & Solomon (2003). The CO(3–2) contours are multiples of $\pm 2\sigma$, where $\sigma = 0.41\,{\rm mJy\,beam^{-1}}$. The CO(7–6) contours are in steps of $\pm 1\sigma$, starting at $\pm 2\sigma$, where $\sigma = 1.3\,{\rm mJy\,beam^{-1}}$.

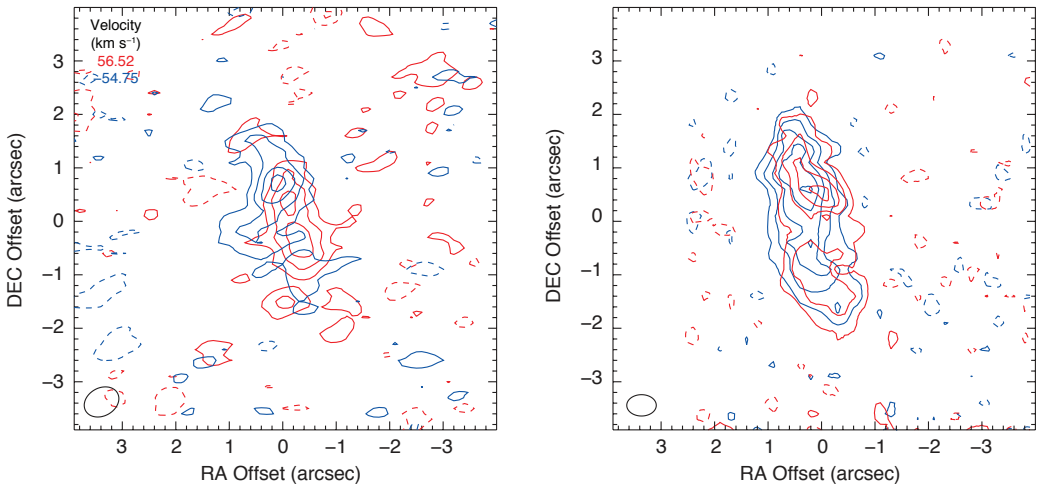

Figure 3.4 Overlaid contours of two 10 MHz ($\sim$ 110 km s^{-1}) channels centered at 56.52 km s^{-1} (red lines) and -54.75 km s^{-1} (blue lines) for the CO(1–0) line (left) and the Hα line (center). Contours are multiples of $\pm 2\sigma$ ($\sigma_{1-0} = 0.17$ mJy beam^{-1}; $\sigma_{\mathrm{H}\alpha} = 1.18 \times 10^{-18}$ W μm^{-1} m^{-2}), where negative contours are dotted; synthesized beam/point spread function is shown at lower left.

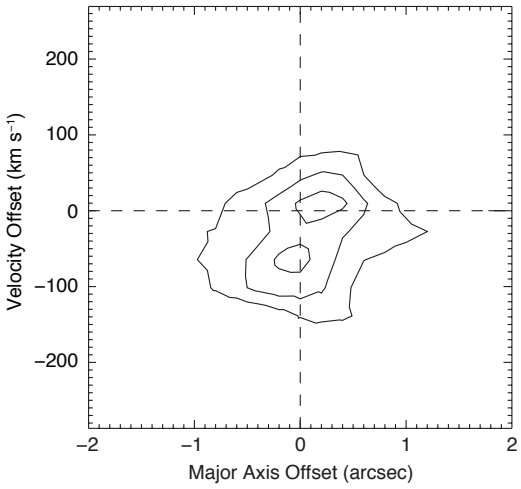

Figure 3.5 Position velocity diagram of the integrated line where the major axis (along the velocity gradient) is at a position angle of 75° that maximizes the velocity gradient. Contours are multiples of 1.75 mJy beam^{-1}.

peaks to better align the datasets. The average offset between the peaks was applied as a shift to align the SPIFFI Hα data cube with the radio observations. The measured offset is $0.''82$, which corresponds to roughly $\lesssim 2\times$ the SPIFFI point spread function (the astrometric uncertainty of the CO(1–0) map is $\sim 0.''09$, including both statistical uncertainty and uncertainty due to the phase calibrator position). Based on this alignment, we use the continuum emission from the line-free channels of the SPIFFI data-cube (at $\sim 2.2\,\mu$m) to extend the alignment to the *HST*/NICMOS F160W data of Aguirre et al. (2013). As we expect the continuum emission at both wavelengths to come from the same physical regions in the source, we use the continuum from the foreground interloper (J1c) and the UV-bright companion galaxy (J2) to determine the shift to apply to the *HST* image to align it with the Hα and thus CO(1–0) maps (Figure 3.3). We measure an offset of $0.''49$ between the F160W and $2.2\,\mu$m maps, making the offset between the CO(1–0) and *HST* maps $< 0.''5$.

3.4 Analysis

3.4.1 LVG Modeling

J14011 has integrated brightness temperature ratios $r_{3,1} = 0.97\pm0.16$ and $r_{7,1} = 0.20\pm0.04$. Comparisons between the higher-J and CO(1–0) emission (convolved to the resolutions of the higher-J maps) do not show evidence for spatial variation of CO excitation. This value of $r_{3,1}$ is larger than the typical $r_{3,1} \sim 0.6$ for SMGs and more similar to the $r_{3,1} \sim 1$ seen in high-z quasar host galaxies. The strong upper limits on X-ray emission and observations of mid-IR PAH features indicate that J14011 likely does not contain an AGN of sufficient strength to influence the global gas conditions, making its near-unity $r_{3,1}$ unusual for its class. However, among low-z U/LIRGs (which also have an average $r_{3,1} \sim 0.6$), there are a small number of starbursts that globally or locally have $r_{3,1} \sim 1$ but lack AGNs, such as NGC 3690 (Iono et al. 2009), UGC 8739 (Yao et al. 2003), the inner region of NGC 253 (e.g., Bayet et al. 2004), and the northeast lobe of M82 (e.g., Ward et al. 2003). While the high $r_{3,1}$ of J14011 is rare for a pure starburst, it is not unique. Yao et al. (2003) propose that high CO excitation in U/LIRGs can be caused by a very high concentration of star formation, consistent with the finding of Iono et al. (2009) that the peak central $r_{3,1}$ is

greater than or equal to the global $r_{3,1}$ in spatially resolved maps. If the duration of highly concentrated star formation (such that the global and "peak" CO excitation are identical) is short-lived, then it is sensible that only a small number of pure-starburst SMGs (or local U/LIRGs) will exhibit high $r_{3,1}$. Gas distributions that are compact relative to heating sources may be the trait that such systems share with quasar host galaxies.

In order to investigate the physical conditions of the gas that produces these ratios, we have undertaken an excitation analysis using an LVG model. The details of the LVG modeling and analysis are described in Chapter 2.4.2 and Appendix B. In short, the model follows the method of Ward (2002), assumes a spherical cloud geometry, and is modified to include the effects of the cosmic microwave background. With observed CO transitions equal in number to the model parameters (kinetic temperature, H_2 density, and CO column density per unity velocity gradient) and substantial uncertainties in the measured line ratios, we expect significant degeneracies between the allowed model parameters. We therefore use both a minimum χ^2 and a Bayesian analysis (the latter better capturing our uncertainties; Ward et al. 2003) to determine which model parameters best reproduce our measured line ratios. For the Bayesian analysis, we have applied logarithmic priors to the LVG model parameters to compensate for the large logarithmically-sampled parameter space, as opposed to the usual agnostic prior equal to unity.

The parameters of the minimum χ^2 model are $T = 136\,\mathrm{K}$, $n_{\mathrm{H_2}} = 10^{3.2}\,\mathrm{cm^{-3}}$, and $N_{\mathrm{CO}}/\Delta v = 10^{17.25}\,\mathrm{cm^{-2}\,km^{-1}\,s}$. However, there are significant degeneracies in all three parameters. For example, the Bayesian maximum probability model favors the opposite extreme in temperature-density parameter space: $T = 24\,\mathrm{K}$, $n_{\mathrm{H_2}} = 10^{5.6}\,\mathrm{cm^{-3}}$, and $N_{\mathrm{CO}}/\Delta v = 10^{16.75}\,\mathrm{cm^{-2}\,km^{-1}\,s}$. Similarly well-fitting models are produced for $20\,\mathrm{K} \lesssim T \lesssim 150\,\mathrm{K}$ at comparable CO columns per velocity gradient ($10^{17\pm0.25}\,\mathrm{cm^{-2}\,km^{-1}\,s}$), where lower temperature models favor higher H_2 densities ($\sim 10^5\,\mathrm{cm^{-3}}$) and higher temperature models favor lower H_2 densities ($\sim 10^3\,\mathrm{cm^{-3}}$). The optical depths produced by these two models are very different from one another. The minimum χ^2 model produces optically thick emission for the CO(3–2) and CO(7–6) transitions ($\tau_{3\text{–}2} = 13.4$, $\tau_{7\text{–}6} = 11.4$), and optically thin emission for the CO(1–0) transition ($\tau_{1\text{–}0} = 0.7$). The cooler and more dense maximum probability model has the optical depths of the CO(1–0) and CO(7–6) lines reversed with

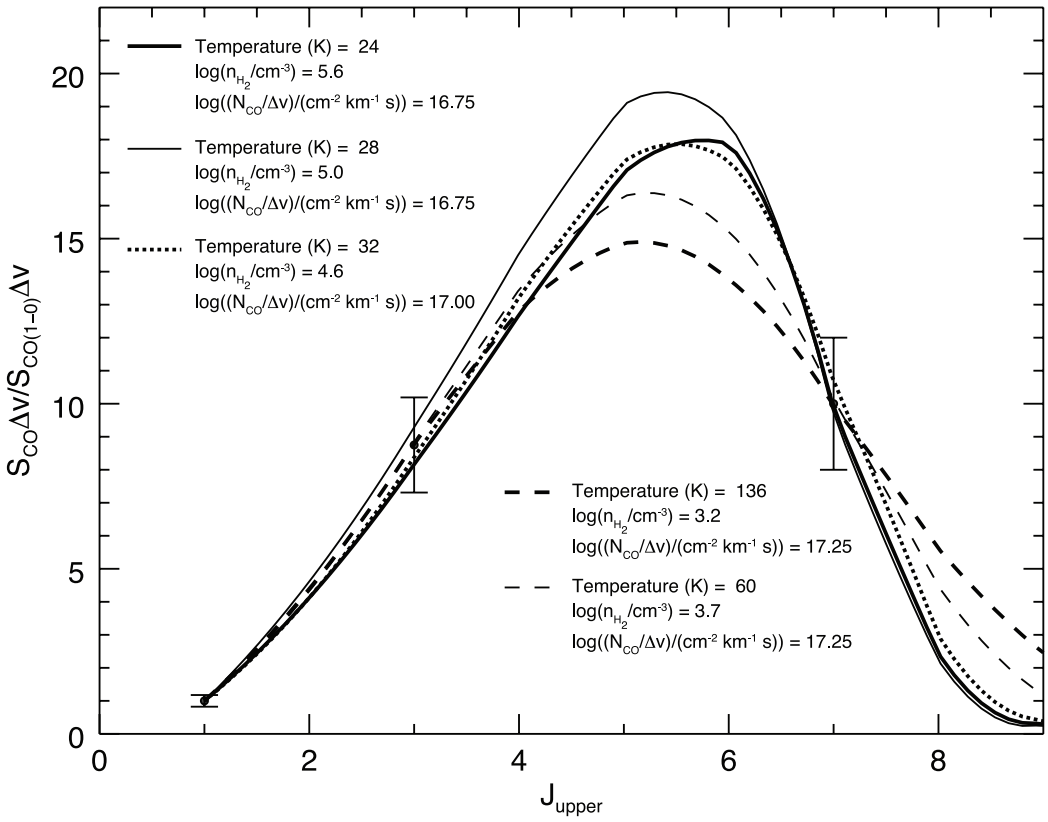

Figure 3.6 Measured line ratios (points; in flux units) and CO SLEDs for the maximum probability model (thick solid line), maximum probability model requiring $\tau > 1$ (thin solid line), minimum χ^2 model (thick dashed line), minimum χ^2 model with $\tau > 1$ (thin dashed line), and the maximum probability/minimum χ^2 model at fixed $T_{\rm C\,I}$ (thick dotted line). The LVG model parameters that produce these SLEDs are as labeled.

$\tau_{1\text{–}0} = 2.0$, $\tau_{3\text{–}2} = 11.8$, and $\tau_{7\text{–}6} = 0.7$. We also consider a restricted parameter space for the LVG models in which *all* of the measured lines must be produced by optically thick emission. The minimum χ^2 model with $\tau_{J_{\rm upper}\leq 7} > 1$ has a significantly lower temperature, $T = 60\,{\rm K}$, $n_{\rm H_2} = 10^{3.7}\,{\rm cm^{-3}}$, and $N_{\rm CO}/\Delta v = 10^{17.25}\,{\rm cm^{-2}\,km^{-1}\,s}$, while the maximum probability model only slightly increases in temperature (relative to the previous maximum probability model), with $T = 28\,{\rm K}$, $n_{\rm H_2} = 10^{5.0}\,{\rm cm^{-3}}$, and $N_{\rm CO}/\Delta v = 10^{16.75}\,{\rm cm^{-2}\,km^{-1}\,s}$. In these models, the optical depths of the CO(1–0) and CO(3–2) emission are comparable ($\tau_{1\text{–}0} \approx 1.5$, $\tau_{3\text{–}2} \sim 10$–$15$), but the CO(7–6) line is only just optically thick in the colder model, while in the warmer model the optical depth is a factor of ~ 10 larger. The CO spectral line energy distributions (SLEDs) for these four models are shown in Figure 3.6.

Our cooler and optically thick models favor kinetic temperatures comparable to the

dust temperature, $T_{\rm dust} = 42\,{\rm K}$ (Wu et al. 2009), and are in line with the results of other LVG analyses of SMGs (e.g., Weiß et al. 2007; Carilli et al. 2010; Riechers et al. 2010; Danielson et al. 2011; Riechers et al. 2011c). Observations of different molecular or atomic species can be useful for breaking temperature degeneracies in CO LVG models. Walter et al. (2011) make an independent estimate of the kinetic temperature in J14011 using their C I($^3P_2 \rightarrow {}^3P_1$) line measurement in conjunction with the previously-measured C I($^3P_1 \rightarrow {}^3P_0$) line (Weiß et al. 2005a), deriving $T_{\rm C\,I} = 32.4 \pm 5.2\,{\rm K}$. At fixed $T_{\rm kin} = T_{\rm C\,I}$, the minimum χ^2 model (which is indistinguishable from the maximum probability model due to similar probability and χ^2 distributions in the $n_{\rm H_2}$–$N_{\rm CO}/\Delta v$ plane) has $n_{\rm H_2} = 10^{4.6}\,{\rm cm^{-3}}$ and $N_{\rm CO}/\Delta v = 10^{17.00}\,{\rm cm^{-2}\,km^{-1}\,s}$ (Figure 3.6) and produces optically thick emission for all three transitions ($\tau_{1-0} = 2.1$, $\tau_{3-2} = 16.0$, $\tau_{7-6} = 2.7$). While a prior LVG analysis performed by Bayet et al. (2009) preferred higher temperatures ($T = 205\,{\rm K}$) and lower densities ($n_{\rm H_2} = 10^{1.4}\,{\rm cm^{-3}}$) than any of our well-fitting models, due to the different goals of their work (predicting line strengths for a statistical sample rather than accurate determination of individual galaxy properties), given their use of only the CO(3–2) and CO(7–6) line measurements and our consistency with other estimates of the gas temperature, we view our results as more robust.

Besides the degeneracies between the best-fit models noted above, it is worth considering what degeneracies exist *within* each model (e.g., degeneracies between $n_{\rm H_2}$ and $N_{\rm CO}/\Delta v$ for a specific choice of temperature, or between $T_{\rm kin}$ and $n_{\rm H_2}$ for a specific value of $N_{\rm CO}/\Delta v$). In Figure 3.7 we have plotted curves of constant probability (or χ^2) on the temperature-density plane for the best-fit values of $N_{\rm CO}/\Delta v$. For a specific value of $N_{\rm CO}/\Delta v$, there is generally an "L"-shaped region with nearly constant probability/χ^2 that will reasonably reproduce a given CO line ratio. With multiple line ratios, the locus where the two "L"-shaped regions overlap produces the best-fit models. For multiple line ratios, these "L"-shaped regions overlap more for emission lines with similar optical depth ratios. The $\tau > 1$ regions are marked with dashed lines in Figure 3.7 and are also "L"-shaped. As optical depth is proportional to $N_{\rm CO}/\Delta v$, larger regions satisfy the $\tau > 1$ criterion for larger values of $N_{\rm CO}/\Delta v$.

For a specific temperature, there are also degeneracies between the H_2 density and CO

column density per velocity gradient. In Figure 3.8 we have plotted curves of constant χ^2 in the $n_{\rm H_2}$–$N_{\rm CO}/\Delta v$ plane for the optically thick model temperatures that give highest probability and minimum χ^2 (in this plane, the probability and χ^2 contours have the same shape, but are scaled differently since the probability is $\propto e^{-\chi^2}$). While slightly shifted between the panels for the two temperatures, there is a clear linear valley with low χ^2. This region corresponds to $N_{\rm CO}/\Delta v \propto n_{\rm H_2}^{-1}$, and it exists for all $T_{\rm kin} > 30\,{\rm K}$ models (for $T < 30\,{\rm K}$, the valley of low χ^2 values asymptotes to a single value of $N_{\rm CO}/\Delta v$ for higher $\rm H_2$ densities). This linear feature corresponds to a constant optical depth ratio for the emission lines that best reproduce the measured line ratios.

With these substantial degeneracies it is worth considering priors in addition to optical depth that might limit the allowed parameter ranges for the LVG models (see also Appendix C). Since the most dense molecular gas in the Galaxy is found in star-forming virialized clouds, we can place limits on the density by considering the dynamical state of the gas. The degree of virialization can be estimated by the ratio of J14011's velocity gradient to the expected velocity gradient for virialized gas with physical conditions described by the best-fit LVG model, which is given by

$$K_{\rm vir} = \frac{\Delta v/\Delta r}{(\Delta v/\Delta r)_{\rm vir}} \sim \frac{1.54}{\sqrt{a}} \frac{\Delta v}{\Delta r} \left[\frac{\langle n_{\rm H_2}\rangle}{10^3\,{\rm cm^{-3}}}\right]^{-1/2} \tag{3.1}$$

where $a \sim 1$–2.5 is a constant that depends on the cloud geometry (e.g., Papadopoulos & Seaquist 1999; Greve et al. 2009; Ivison et al. 2011). Since virialization is the most dynamically relaxed state of the gas kinematics, in this parameterization, $K_{\rm vir} \ll 1$ is dynamically unobtainable and $K_{\rm vir} \gg 1$ represents unbound gas motions. For J14011, the velocity gradient could be a value determined by global parameters (given by the $\sim 150\,{\rm km\,s^{-1}}$ CO(1–0) FWHM and approximate delensed optical source size of $\sim 10\,{\rm kpc}$ from Smail et al. (2005)) if the line luminosity is tracing the total gravitational potential of the galaxy (e.g., Downes et al. 1993), or a different value if the molecular gas is in individual star-forming clouds. For the global velocity gradient, requiring that $K_{\rm vir} > 0.1$ means that $n_{\rm H_2} > 10^{1.5}\,{\rm cm^{-3}}$ is not allowed, excluding all of the well-fitting models discussed above. In general, low χ^2 models with low densities that meet the $K_{\rm vir} > 0.1$ criterion under-predict

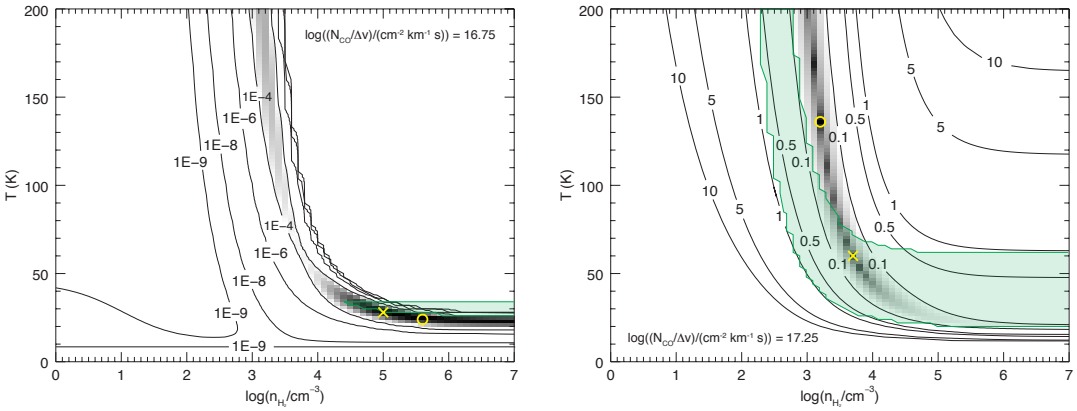

Figure 3.7 Contours of constant probability (left) and χ^2 (right) in the temperature-density plane for the best-fit values of $N_{\rm CO}/\Delta v$. Models with higher probability than the highest contour (or lower χ^2 than the lowest contour) have been logarithmically shaded in gray scale. Models with parameters outside of the green-shaded region produce optically thin emission in at least one line. The best-fit models with and without the optical depth cut have been marked with yellow crosses and circles respectively.

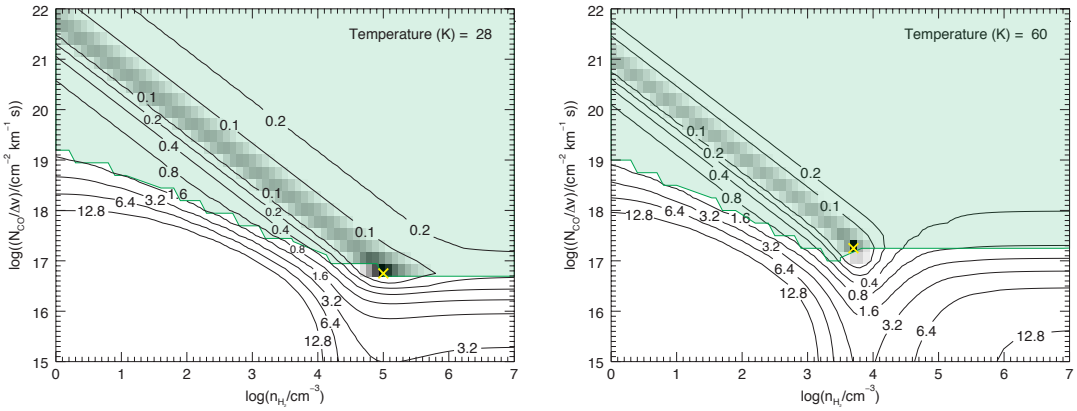

Figure 3.8 Contours of constant χ^2 in the $n_{\rm H_2}$–$N_{\rm CO}/\Delta v$ plane for highest probability optically thick model (28 K; left) and minimum χ^2 optically thick model (60 K; right). Models with $\chi^2 < 0.1$ have been logarithmically shaded in gray scale. Models with parameters that fall below the green-shaded region produce optically thin emission. The highest probability/minimum χ^2 models in each plane are marked by the yellow crosses.

the CO(3–2)/CO(1–0) line ratio by $\gtrsim 1\sigma_{3,1}$. Velocity gradients larger than the global value would allow the higher densities of our best-fit LVG models to satisfy the virialization requirement. In order to allow densities as high as $10^4\,\mathrm{cm}^{-3}$ ($10^5\,\mathrm{cm}^{-3}$) with $K_{\mathrm{vir}} > 0.1$, the velocity gradient would need to be $> 0.27\,\mathrm{km\,s^{-1}\,pc^{-1}}$ ($> 0.86\,\mathrm{km\,s^{-1}\,pc^{-1}}$.) If the individual clouds are virialized ($K_{\mathrm{vir}} = 1$), these H_2 densities require velocity gradients of $\sim 3\,\mathrm{km\,s^{-1}\,pc^{-1}}$ ($\sim 9\,\mathrm{km\,s^{-1}\,pc^{-1}}$).

Models with low n_{H_2} and high $N_{CO}/\Delta v$ can be eliminated by requiring the CO column length to be less than the maximum source size. However, this prior requires the assumption of an upper limit for $[CO/H_2]$. Conservative limits (i.e., $[CO/H_2] < 5 \times 10^{-4}$; Ward et al. 2003) exclude clouds with densities comparable to or less than that seen in the Milky Way ($\sim 10^2\,\mathrm{cm}^{-3}$) along the low-$\chi^2$ degeneracy valley in the n_{H_2}–$N_{CO}/\Delta v$ plane. While this prior is not useful for distinguishing among the best-fit models for J14011, it does support the higher H_2 densities preferred by the LVG analysis.

While it is unlikely that a simple LVG model will accurately capture the full range of temperatures and densities that exist in real molecular clouds, considering the degeneracies discussed above, we conclude that the bulk of the molecular gas likely has, on average, $T_{\mathrm{kin}} = 20$–$60\,\mathrm{K}$, $n_{H_2} \sim 10^4$–$10^5\,\mathrm{cm}^{-3}$, and $N_{CO}/\Delta v = 10^{17.00\pm0.25}\,\mathrm{cm^{-2}\,km^{-1}\,s}$. The maximum likelihood for the thermal pressure peaks at $\sim 10^2\,\mathrm{K\,cm^{-3}}$, but has a significant tail up to $10^6\,\mathrm{K\,cm^{-3}}$. Measurements of other mid-J CO lines, like CO(5–4), would help to better constrain these models. Using our best estimates for the LVG model parameters, we constrain $[CO/H_2]/(\Delta v/\Delta r) = 10^{-6.7}$–$10^{-5.2}\,\mathrm{pc\,km^{-1}\,s}$, which is close to the standard assumption of $10^{-5}\,\mathrm{pc\,km^{-1}\,s}$ used in other LVG analyses. While the measured line ratios in J14011 appear consistent with a single phase molecular ISM, analysis of other SMGs (e.g., Harris et al. 2010; Ivison et al. 2011; Danielson et al. 2011; Bothwell et al. 2013) and observations of local galaxies (e.g., Yao et al. 2003) indicate that gas in star-forming galaxies is multi-phase; i.e., it is unlikely that the gas responsible for the bulk of the CO(1–0) emission is the same gas that is emitting the CO(7–6) line, which is effectively what we are requiring by considering only single-phase models. With only three measured lines, the results of a multi-phase LVG analysis would be far too degenerate to draw meaningful conclusions about the state of molecular gas. Higher resolution observations would be helpful in establishing

whether the CO lines are or are not being emitted from the same physical volumes of gas. Based on the agreement of the global line profiles for the existing CO measurements it is unlikely that excitation differences exist on large scales across J14011, but local variations with broadly similar kinematics could exist on scales below our current resolution limit.

Based on the CO abundance per unit velocity gradient of the best-fit LVG models, we can determine the CO-to-H_2 abundance for an assumed velocity gradient. Using the global velocity gradient from our measured line width and the Smail et al. (2005) source size, we estimate the CO-to-H_2 abundance to be $[CO/H_2] = 10^{-8.6}$–$10^{-7.1}$, which is very low. Alternatively, if we assume more standard values of $[CO/H_2] = 10^{-5}$–10^{-4}, the best-fit model densities return higher velocity gradients of ~ 1–$30\,\mathrm{km\,s^{-1}\,pc^{-1}}$, a range that includes the necessary gradients for our best-fit models to meet the virialization criteria.

Since LVG modeling produces reasonable physical conditions for J14011, and it is only the introduction of the global velocity gradient that produces very low CO-to-H_2 abundance and unphysical virialization parameters, we conclude that J14011 likely has large local velocity gradients. Higher velocity gradients are possible if J14011 has a face-on orientation and contains numerous small clouds below our resolution limit that have turbulent velocities and/or bulk motions summing to the measured $\mathrm{FWHM}_{1\text{–}0} \approx 150\,\mathrm{km\,s^{-1}}$. If the individual clouds are virialized, their velocity gradients are large enough to produce more reasonable values of the CO-to-H_2 abundance for our best-fit densities. Although such velocity gradients would cause J14011's molecular clouds to fall above the Galactic line-width vs. size relation (Larson 1981), such behavior has been seen in another $z \sim 2$ SMG, SMM J2135-0102, which has a mean internal velocity gradient of $\sim 0.5\,\mathrm{km\,s^{-1}\,pc^{-1}}$ for individual clumps (Swinbank et al. 2011). Swinbank et al. (2011) also find similarly high densities, and thus infer LVGs under the assumption of virialization, for the molecular gas in SMM J2135-0102.

3.4.2 Resolved Star Formation Law

Using the aligned Hα and CO(1–0) maps, we plot a spatially resolved Schmidt-Kennicutt relation (Schmidt 1959; Kennicutt 1998) for J14011 in Figure 3.9. We have smoothed the integrated line maps to the same spatial resolution ($0.''70 \times 0.''65$), resampled to the pixel size from the SPIFFI data ($0.''25$), and excluded pixels that do not have at least 2σ

significance in both maps. In order to convert the Hα surface luminosity to a SFR surface density, we use the $L_{\mathrm{H}\alpha}$-SFR conversion factor given in Kennicutt (1998) scaled to match the Calzetti et al. (2007) initial mass function (IMF) used in Bigiel et al. (2008, 2010). We have also applied an additional correction to reflect the fact that the observed Hα luminosity underestimates the galaxy's total SFR: based on the Kennicutt (1998) calibration rescaled to the Calzetti et al. (2007) IMF, J14011's total FIR-determined SFR is $400\,M_{\odot}\,\mathrm{yr}^{-1}$, exceeding its H$\alpha$-determined SFR by a factor of 15. Given that J14011 does not contain a strong AGN (Rigby et al. 2008), that there is good agreement between the CO and the Hα morphologies (unlikely if the FIR vs. Hα discrepancy were determined by *large-scale* patchiness in obscuration), and that the correction for the Balmer decrement as in Tecza et al. (2004) would already account for a factor of 1.5 (of the factor of 15 difference), we have simply scaled the Hα surface brightness of each pixel by the *global* ratio $\mathrm{SFR}_{\mathrm{FIR}}/\mathrm{SFR}_{\mathrm{H}\alpha}$ before plotting in Figure 3.9.

Converting CO(1–0) luminosity to molecular gas mass requires the assumption of a conversion factor α_{CO}. Based on the results of our LVG analysis above, which produces more self-consistent molecular gas properties if the molecular ISM in J14011 is composed of multiple unresolved clouds rather than a single large gas reservoir, we use a fiducial Milky Way disk value of $\alpha_{\mathrm{CO}} = 4.6\,M_{\odot}\,(\mathrm{K\,km\,s^{-1}\,pc^{2}})^{-1}$ (Solomon & Barrett 1991). This choice is consistent with the proposed continuous form of α_{CO} of Narayanan et al. (2012) for the measured metallicity of component J1 from Tecza et al. (2004) of $12+\log(\mathrm{O/H}) = 8.96^{+0.06}_{-0.10}$. In Figure 3.9, the gas mass surface densities for both J14011 and the low-redshift galaxies have been scaled to account for helium. Since gravitational lensing conserves surface brightness, magnification corrections are to first order unnecessary for evaluating the resolved Schmidt-Kennicutt relation for J14011.

The resolved star formation law for J14011, as probed by the FIR-corrected Hα map, is not consistent with that of the local disk galaxies from Bigiel et al. (2008) despite our use of a Milky Way gas mass conversion factor. While Bigiel et al. (2008) use a sub-Milky Way value of $\alpha_{\mathrm{CO}} = 3.2\,M_{\odot}\,(\mathrm{K\,km\,s^{-1}\,pc^{2}})^{-1}$, any value of $\alpha_{\mathrm{CO}} < 4.6$ moves J14011 further above the local relation, and $\alpha_{\mathrm{CO}} = 0.8$ moves it far above. Our result supports the conclusions of Genzel et al. (2010), indicating that SMGs' position above the local star

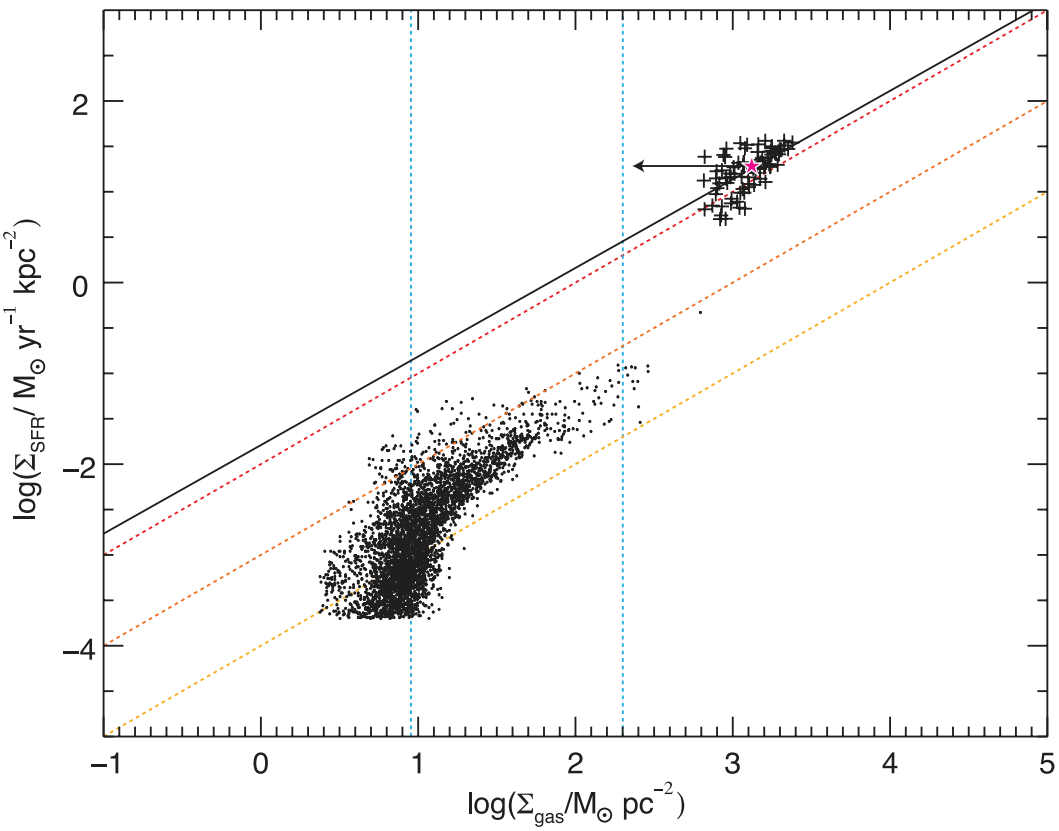

Figure 3.9 Star formation rate surface density as measured by Hα surface brightness (rescaled by the global $\mathrm{SFR_{FIR}/SFR_{H\alpha}}$) vs. molecular gas mass surface density for J14011 (crosses) and total gas mass surface density for local disk galaxies from Bigiel et al. (2010) (dots; clipped at $2 \times 10^{-4}\,M_\odot\,\mathrm{yr}^{-1}\,\mathrm{kpc}^{-2}$). The average value for J14011 is given by the star, and a power law fit to the resolved surface density points is given by the solid line. The arrow pointing to the left shows where J14011's locus of points (centered at the average value) would move if the molecular gas mass were calculated using the "starburst" value of α_{CO} instead of the "disk" value. Dotted lines are the same as in Bigiel et al. (2008), where the diagonal lines represent the constant star formation efficiencies required to consume 1% (yellow), 10% (orange), and 100% (red) of the gas in 10^8 years, the left vertical line shows the HI surface density saturation, and the right vertical line marks the proposed transition between star formation laws at $200\,M_\odot\,\mathrm{pc}^{-2}$.

formation relation is not simply due to the choice of CO-to-H_2 conversion factor. Correcting for different IMFs while respecting the differing choices in α_{CO}, the star formation law for J14011 is consistent with both the SMGs in Genzel et al. (2010) (who use $\alpha_{CO} = 1.0$) and the local starbursts from Kennicutt (1998) (who uses $\alpha_{CO} = 0.8$), and is not consistent with the high-z "normal" star-forming galaxies from Daddi et al. (2010) (who use $\alpha_{CO} = 3.6$). Rescaling J14011 to the lower α_{CO} used in Genzel et al. (2010) or Kennicutt (1998) would move J14011 far above the star formation relation for SMGs and low-z starbursts, further supporting our choice of a Galactic CO-to-H_2 conversion factor for this system.

To allow comparisons to other work, we fit the star formation and molecular gas surface densities to a power law and formally retrieve a near-unity index of 0.98 ± 0.14 (albeit with $\chi^2 = 2.48$), consistent with indices measured in local spirals (Bigiel et al. 2008). Our application of the scaling factor to account for dust-obscured star formation does not affect our measured index, as appropriate if Hα traces the location of J14011's star-forming regions, even if it does not capture the total SFR. We note that in our pixel-to-pixel comparison, the data points are not all independent due to our oversampling of the beam/point spread function; the points in Figure 3.9 are drawn from a total area of ~ 10 resolution elements.

3.5 Summary

We present high-resolution CO(1–0) mapping of the SMG SMM J14011+0252. Based on a spectrally resolved detection, we find a revised near-unity value for the CO(3–2)/CO(1–0) line ratio ($r_{3,1} = 0.97 \pm 0.16$). Although $r_{3,1}$ is closer to the average value seen in quasar host galaxies than in SMGs, given that similar values are seen in some low-z ULIRGs that lack AGNs, $r_{3,1} \sim 1$ is not inconsistent with previous observational limits on the AGN strength in J14011. J14011 may be experiencing a short period of highly-concentrated star formation affecting the gas excitation (e.g., Yao et al. 2003; Iono et al. 2009), indicating that $r_{3,1} \sim 1$ is not a perfect discriminant between starbursts and quasar host galaxies at high redshift. We find that the position of the CO(1–0) emission agrees with those of previously detected mid-J lines (Downes & Solomon 2003). The CO(1–0) emission is spatially extended from the southeast to northwest, extending between the J1s and J1n

components previously identified at optical wavelengths, and showing two peaks that are slightly offset in velocity. A face-on interpretation is favored by our LVG models and is consistent with J14011's narrow line width.

Although the results of the LVG modeling are highly degenerate and we are restricted to a single-phase analysis, our determination of the gas kinetic temperature is consistent with the gas temperature measured using C I (Walter et al. 2011) and with the dust temperature (Wu et al. 2009). Our best-fit models give $n_{\mathrm{H_2}} \sim 10^4$–$10^5\,\mathrm{cm^{-3}}$ and $N_{\mathrm{CO}}/\Delta v = 10^{17.00\pm0.25}\,\mathrm{cm^{-2}\,km^{-1}\,s}$. These densities only produce reasonable [CO/H_2] values and satisfy dynamical constraints if the velocity gradient is larger than the galaxy wide-average, implying that J14011's molecular ISM comprises numerous unresolved molecular clouds.

Based on the agreement between the metallicity-dependent version of the CO-to-H_2 conversion factor from Narayanan et al. (2012) and the canonical "disk" value favored by our LVG analysis, we use $\alpha_{\mathrm{CO}} = 4.6\,M_\odot\,(\mathrm{K\,km\,s^{-1}\,pc^2})^{-1}$ to derive a molecular gas mass of $(1.9 \pm 0.3) \times 10^{11}\,M_\odot$ (corrected for $\mu = 3.5$; Smail et al. 2005). Using Hα data from Tecza et al. (2004), corrected by the SFR measured in the FIR, we are able to compare the spatially-resolved Schmidt-Kennicutt relation in J14011 to those of other galaxies. We find that J14011 falls above the SFR vs. molecular gas surface density relation seen in normal star-forming galaxies (e.g., Bigiel et al. 2008), even when we use the local "disk" value of the CO-to-H_2 conversion factor. This result indicates that the observed offset of starburst galaxies from the local universe Schmidt-Kennicutt law is not solely due to the use of two different gas mass conversion factors, in agreement with Genzel et al. (2010). J14011 is consistent in its star formation relation with other SMGs and starbursts when we respect different authors' choices of gas mass conversion factor. The near-unity index of the power law fit to J14011's points is comparable to indices measured in the local universe.

Chapter 4

SDSS J0901+1814

4.1 Background

SDSS J0901+1814 (J0901 hereafter) was discovered by Diehl et al. (2009) in a systematic search of the Sloan Digital Sky Survey (York et al. 2000) for strongly lensed galaxies (identified as blue arcs near known brightest cluster galaxies or luminous red galaxies). Followup observations at the Astrophysics Research Consortium (ARC) 3.5 m telescope at Apache Point Observatory confirmed that J0901 is a $z = 2.26$ (Diehl et al. 2009; Hainline et al. 2009) galaxy that is multiply imaged (made up two bright arcs in the north and south that nearly connect along the eastern side, and a small dim western component) by a $z = 0.35$ luminous red galaxy. Single-slit spectroscopy at rest frame optical wavelengths made using Keck II/NIRSPEC showed large [N II] ($\lambda = 6583$ Å)/Hα ratios in the two brightest images (Hainline et al. 2009), indicating the presence of a narrow-line AGN in J0901 (since there is a maximum ionization level that starbursts can achieve; e.g., Baldwin et al. 1981; Kauffmann et al. 2003). However, the strong PAH features detected in *Spitzer*/IRS spectra and weak continuum features in the (observed frame) mid-IR suggest that the AGN contribution to the IR luminosity of J0901 is negligible (Fadely et al. 2010). Further observations obtained from the SMA revealed that J0901 is one of the brightest high-redshift UV-selected galaxies in terms of its dust emission (e.g., Baker et al. 2001; Coppin et al. 2007). Saintonge et al. (2013) estimate a total IR luminosity (magnification corrected) of $L_{\rm IR} \sim 7.1 \times 10^{12}\, L_{\odot}$ using *Herschel*/SPIRE photometry. The substantial dust content implied by the IR luminosity makes it a natural target for molecular gas observations; only a small number UV-selected galaxies have been successfully detected in CO (e.g., Baker et al. 2004; Coppin et al. 2007; Riechers et al. 2010). In addition the gravitational lensing provides additional spatial resolution, allowing us to make more detailed observation of gas and star formation

conditions within J0901.

For the following analysis, we assume a magnification factor of $\mathcal{M} = 11.2 \pm 2.2$ from the preliminary lensing reconstruction by A. Tagore. The CO(3–2) data (from the PdBI) and Hα data (from the VLT/SINFONI) are part of a work in preparation where the data reduction has been performed by A. Baker and J. Rivera, respectively.

4.2 Observations

We observed J0901 at the VLA in three different configurations; the configurations, maximum baselines, observation dates, number of antennas used, and weather conditions are summarized in Table 4.1. The minimum uv-radius of the full dataset is $3.67\,\mathrm{k}\lambda$. We observed with the WIDAR correlator in the "OSRO Dual Polarization" mode using the lowest spectral resolution (256 channels $\times$ 500 kHz resolution) and only a single IF pair (B/D). The total bandwidth of 128 MHz was centered at the observed frequency of CO(1–0) for $z = 2.2586$ (35.363 GHz). Observations were centered at $\alpha(\mathrm{J2000}) = 09^{\mathrm{h}}01^{\mathrm{m}}23.^{\mathrm{s}}00$, $\delta(\mathrm{J2000}) = +18°14'24.0''$, the position of the southernmost and brightest (at optical wavelengths) of the three lensed images (Diehl et al. 2009), to be consistent with the existing PdBI observations. At the beginning of each track, we observed 3C 138 as both passband and flux calibrator, adopting $S_\nu = 1.1786$ Jy using the CASA package's default "Perley-Butler 2010" flux standard. Phase and amplitude fluctuations were tracked by alternating between the source and the nearby quasar J0854+2006 with a cycle time of 6 minutes. A total of 16 hours was spent on source.

Calibration and mapping were carried out in CASA. A Hogbom cleaning algorithm was used to construct the image model; model components were restricted to an arc-shaped region that encompassed the northern and southern images, and a circle at the position of the western image. Due to the strong velocity structure in J0901, even our fairly restrictive clean boxes contained sufficient area that the clean algorithm rarely achieved the threshold 1σ depth in a reasonable number of iterations (< 5000). Instead we chose a maximum number of iterations (500) after which the identification of further model components yielded

Table 4.1. J0901 VLA Observations

Configuration Max. Baseline	Date	$N_{\rm Ant}$	Weather
D	3 April 2010	17	Clear
1.031 km	15 April 2010	20	Clear
	4 May 2010	19	Clear
	8 May 2010	19	Average sky cover 25%; mixed clouds
	15 May 2010	20	Sky cover 20%; cumuliform clouds
B	14 February 2011	26	Sky cover $< 30\%$; stratiform clouds
10.306 km			
C	29 January 2012	26	Clear
3.289 km	30 January 2012	25	Clear
	31 January 2012	25	Clear
	26 March 2012	25	Sky cover 90%; stratiform clouds
	30 March 2012	27	Sky cover 20%; stratiform clouds

negligible additional flux. Each track was corrected to the local kinematic (radio) standard of rest using the CASA routine cvel. The final data cube was created to match the channelization of the CO(3–2) data (rest frame spectral resolution of $14.129\,{\rm km\,s^{-1}}$). The naturally weighted channel maps have a synthesized beam of $0.''79 \times 0.''68$ at a position angle of -70.76°. Since the spatial extent of J0901 is a substantial fraction of the VLA antenna primary beam FWHM, we apply a primary beam correction in order to retrieve the correct flux from the source (a $\sim 10\%$ correction for the northern image). The average rms noise for each channel is $0.136\,{\rm mJy\,beam^{-1}}$ (prior to correcting for the primary beam).

The supporting data used in this analysis are CO(3–2) mapping from the PdBI and near-IR ($2\,\mu$m) integral field spectroscopy (which includes the Hα and [N II] lines for J0901) from the VLT/SINFONI. The CO(3–2) data have a synthesized beam FWHM of $1.''33 \times 0.''98$ at a position angle of 41.1°. The average noise per channel is $0.579\,{\rm mJy\,beam^{-1}}$, prior to correcting for PdBI primary beam sensitivity. The PdBI observations have a minimum uv-radius of $5.28\,{\rm k}\lambda$. Since J0901 is large compared to the SINFONI field of view, the three images were observed on separate nights, which resulted in slightly different point spread functions (PSFs) for each image ($\Delta{\rm FWHM} = 0.''1$). The Hα observations are smoothed to the largest PSF of the three images (the western image; $0.''85 \times 0.''76$ at 14.4°) or to the

CO beam size (for comparisons) if it was larger than the Hα PSF. The spectral resolution of SINFONI is $\lambda/\Delta\lambda \sim 9000$, which corresponds to channel widths of $36.75\,\mathrm{km\,s^{-1}}$ for the Hα line. A $\sim 100\,\mathrm{km\,s^{-1}}$ velocity offset was applied to align the centroid of the Hα line to that of the CO lines. The alignment for the Hα map relative to the CO maps was determined using an imaging cross-correlation algorithm by Adam Ginsburg[1], which led to an astrometric correction of $1.''32$ for the near-IR data. The NIRSPEC data are not fully flux calibrated, however, as they are only used in the following analyses when scaled to match the total FIR luminosity, their absolute flux calibration is unimportant.

4.3 Results

We successfully detect the three images of J0901 in both the CO(1–0) and CO(3–2) maps (Figure 4.1). In order to make a fair comparison between the two maps, we also analyze a version of the CO(1–0) datacube that has been constructed to match the CO(3–2) synthesized beam and inner *uv*-radius. The *uv*-clipping ensures that flux distributed on large spatial scales that cannot be detected at the PdBI also gets excluded from the CO(1–0) maps. We refer to the two sets of CO(1–0) maps as the "natural" and "clipped" maps throughout. The measured line fluxes are summarized in Table 4.2 and are extracted over identical image areas between the three maps; the uncertainties include an assumed 10% flux calibration error. We find that the *uv*-clipping removes a significant fraction, $\sim 35\%$, of the CO(1–0) flux. For the spectra in Figure 4.2, we only present the results for natural CO(1–0) map, extracted over slightly smaller regions to better capture the line shapes[2]. We find that the spectra of the two lines have a consistent FWZI $\approx 350\,\mathrm{km\,s^{-1}}$ centered at the Hα-determined systemic redshift from Hainline et al. (2009), but that the shapes of the two CO line profiles differ for the same image. The different relative line profiles for the three images suggest that differential lensing is occurring; i.e., the spatial variation of the magnification factor across J0901 is amplifying the light in regions with different CO(3–2)/CO(1–0) line ratios (e.g., Blain 1999; Serjeant 2012). In Figure 4.3 we show the

[1] "pixshift": http://casa.colorado.edu/∼ginsbura/corrfit.htm

[2] Due to the velocity structure of J0901 and the small synthesized beam in the natural CO(1–0) maps, the larger regions used in the rest of the analysis include a larger number of signal-free pixels, which increases the noise per channel significantly for the extracted spectrum.

overlaid channel maps of the natural CO(1–0) and CO(3–2) lines, rebinned by a factor of two; there is a clear velocity gradient across the three images, suggesting J0901 is either a disk-like or merging galaxy.

In order to estimate a gas mass for J0901, we use the natural CO(1–0) line flux from all three images and the global average magnification, obtaining $M_{\rm gas} = (7.6 \pm 1.7) \times 10^{10} (\alpha_{\rm CO}/0.8)\, M_{\odot}$ (where we have chosen the U/LIRG CO-to-H_2 conversion factor to effectively give a lower limit on the gas mass). We note that the gas mass of J0901 is comparable to that of other galaxies selected at submillimeter wavelengths, but larger than that of other UV-selected high-redshift galaxies (e.g., Riechers et al. 2010). The preliminary lens modeling also yields an approximate source size of $\sim 1.5''$ along the velocity gradient, which corresponds to a physical radius of 6.3 kpc at $z = 2.259$. Assuming the velocity gradient of J0901 is due to rotation, we estimate the dynamical mass to be $M_{\rm dyn} \sin^2(i) = 1.9 \times 10^{10}\, M_{\odot}$, where we have used half of the FWHM $= 225 \pm 21\,{\rm km\,s^{-1}}$ from the sum of the higher S/N CO(3–2) spectra as the component of the circular velocity along our line of sight. In order for the dynamical mass to be larger than the gas mass, J0901 must be have an inclination angle of $\lesssim 30^{\circ} \pm 5^{\circ}$ (i.e., if J0901 is a disk galaxy, it is not edge on).

4.4 Analysis

4.4.1 Spatial Variation in CO Excitation

In order to understand the gas conditions in J0901, we examine the CO(3–2)/CO(1–0) line ratio in units of brightness temperature, Table 4.2. We find that the global line ratios of the three images do not differ significantly. Using the *uv*-clipped CO(1–0) map, we find that J0901 has a global average $r_{3,1} = 0.79 \pm 0.12$. This value is slightly larger than the $r_{3,1}$ found for SMGs, comparable to the $r_{3,1}$ found for LBGs (Riechers et al. 2010; although the sample size is small), and larger than the value implied from the excitation analysis of $z \sim 1.5$ *BzK*-selected galaxies (Dannerbauer et al. 2009). We note that the $r_{3,1}$ values from the natural CO(1–0) maps is significantly lower, with a global average value of $r_{3,1} = 0.52 \pm 0.08$, closer to that of SMGs than LBGs. This value of $r_{3,1}$ can be considered a lower limit for J0901, corresponding to the case that the extended gas producing the CO(1–0) emission in the

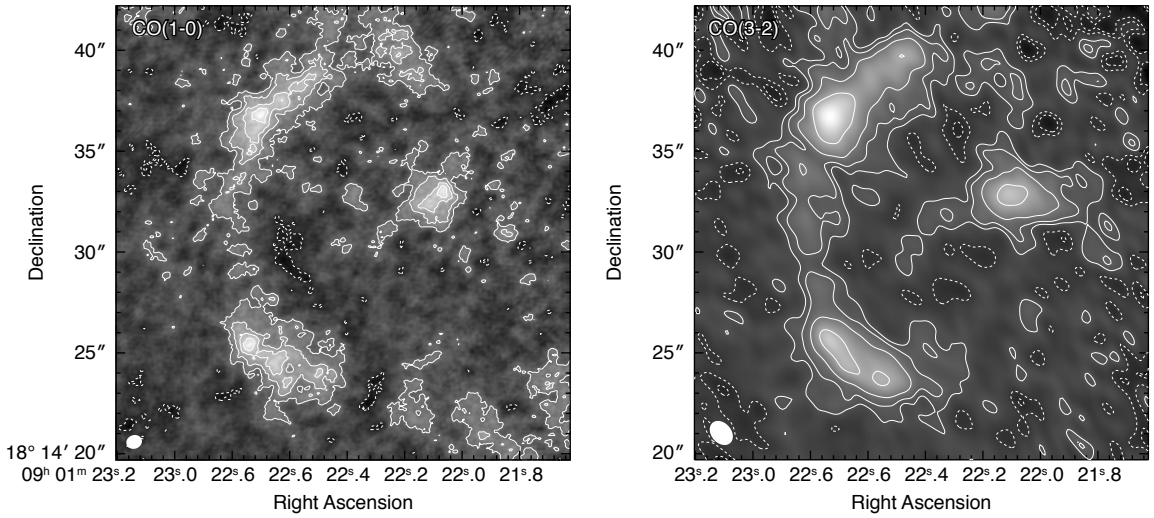

Figure 4.1 Integrated CO(1–0) (left) and CO(3–2) (right) intensity maps (with primary beam correction applied); the CO(1–0) map is the "natural" map that has not been *uv*-clipped to match the CO(3–2) map. Contours are multiples of $\pm 2\sigma_{1-0}$ for the CO(1–0) map and are power of $2 \times \pm\sigma_{3-2}$ for the CO(3–2) map ($\sigma_{1-0} = 0.68\,\mathrm{mJy\,beam^{-1}}$; $\sigma_{3-2} = 2.89\,\mathrm{mJy\,beam^{-1}}$). Negative contours are dotted and the synthesized beams are shown at lower left.

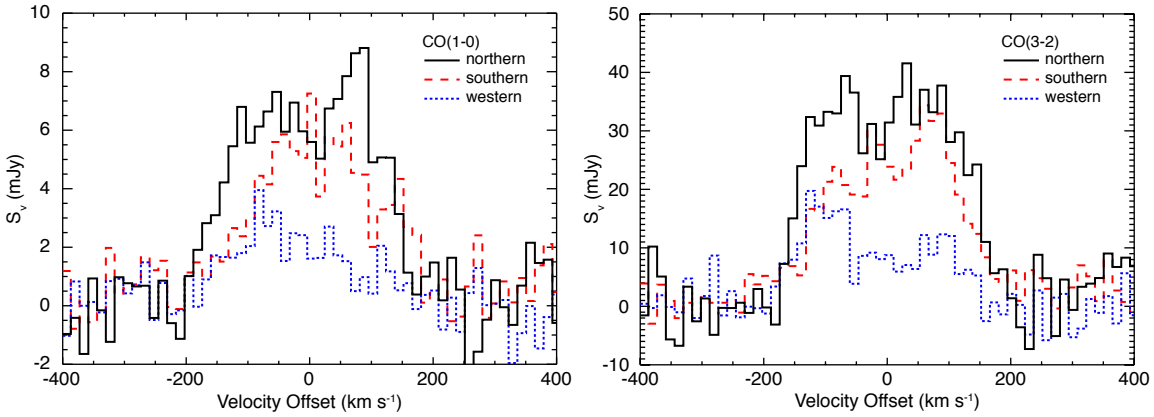

Figure 4.2 VLA CO(1–0) spectra extracted from the natural map (left) and PdBI CO(3–2) spectra (right) for the northern (black/solid), southern (red/dashed), and western (blue/dotted) images, plotted relative to the $z = 2.2586$ Hα systemic redshift from Hainline et al. (2009).

Table 4.2. J0901 Line Measurements

Line/Map	Parameter	North	South	West	Total
CO(1–0)	$S_{1-0}\Delta v$[a]	2.11 ± 0.24	1.32 ± 0.17	0.78 ± 0.11	4.21 ± 0.46
natural	$L'_{\mathrm{CO(1-0)}}$[b]	53.6 ± 6.2	33.5 ± 4.3	19.8 ± 2.9	9.54 ± 2.14[c]
	$r_{3,1}$	0.49 ± 0.08	0.59 ± 0.10	0.48 ± 0.09	0.52 ± 0.08
CO(1–0)	$S_{1-0}\Delta v$[a]	1.34 ± 0.15	0.91 ± 0.11	0.53 ± 0.7	2.78 ± 0.30
uv-clipped	$L'_{\mathrm{CO(1-0)}}$[b]	34.1 ± 3.9	23.0 ± 2.8	13.5 ± 1.9	6.30 ± 1.41[c]
	$r_{3,1}$	0.77 ± 0.12	0.87 ± 0.14	0.70 ± 0.13	0.79 ± 0.12
CO(3–2)	$S_{3-2}\Delta v$[a]	9.35 ± 1.00	7.10 ± 0.76	3.36 ± 0.41	19.8 ± 2.0
	$L'_{\mathrm{CO(3-2)}}$[b]	26.4 ± 2.8	20.0 ± 2.1	9.50 ± 1.16	4.99 ± 1.11[c]

[a]In units of $\mathrm{Jy\,km\,s^{-1}}$.

[b]In units of $10^{10}\,\mathrm{K\,km\,s^{-1}\,pc^2}$.

[c]The total line luminosities are magnification corrected assuming $\mathcal{M} = 11.2 \pm 2.2$, where the uncertainty in magnification has been folded into the quoted errors.

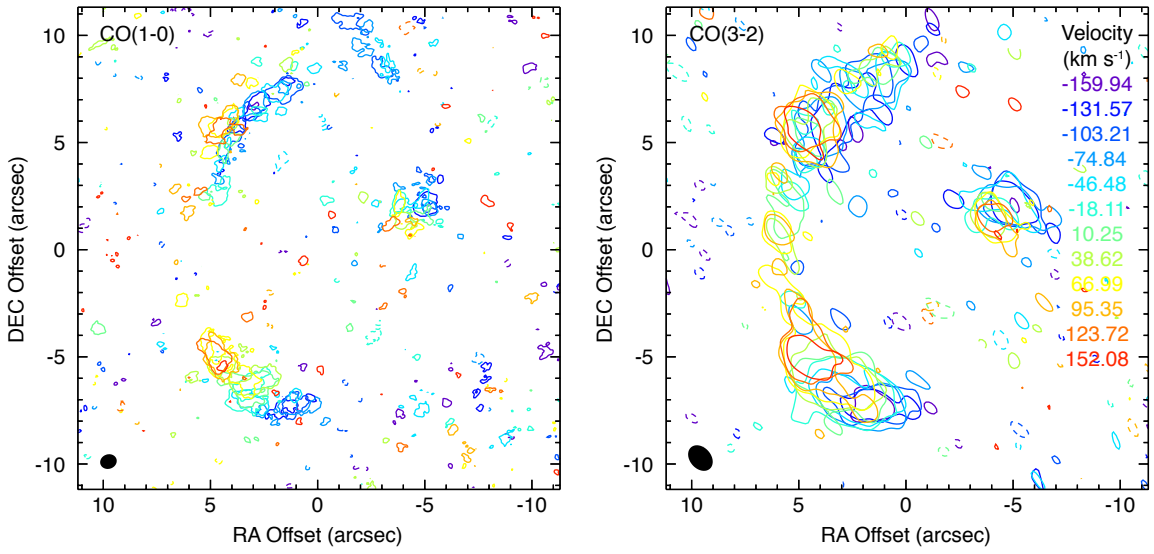

Figure 4.3 Overlaid $\pm 3\sigma$ contours of the natural CO(1–0) (left) and CO(3–2) (right) channel maps ($\sigma_{1-0} = 0.14\,\mathrm{mJy\,beam^{-1}}$, $\sigma_{3-2} = 0.82\,\mathrm{mJy\,beam^{-1}}$), colorized by their relative velocity and centered at α(J2000) = $09^{\mathrm{h}}01^{\mathrm{m}}22.^{\mathrm{s}}42$ and δ(J2000) = $+18°14'30.''9$. Channels have been rebinned by a factor of two to $28.37\,\mathrm{km\,s^{-1}}$ and negative contours are dotted. For clarity we do not use the primary beam-corrected data. Synthesized beams are shown at lower left.

natural map does not produce any additional CO(3–2) emission.

The strong gravitational lensing of J0901 yields additional angular resolution, which allows us to examine spatial variation in the CO excitation. For comparisons to the CO(3–2) map, we used the *uv*-clipped CO(1–0) map (which is also matched to the CO(3–2) map in terms of primary beam and pixel sizes). Figure 4.4 shows the integrated line ratio for J0901, and Figure 4.5 shows the line ratio maps as a function of velocity for five channels that span the line profiles. The average value of $r_{3,1}$ in the line ratio map is ~ 0.8, in line with the $r_{3,1}$ calculated from the integrated line flux of the *uv*-clipped CO(1–0) map. For the ratio map of the integrated lines, the lower-excitation gas (areas in the map with lower values of $r_{3,1}$) appears to be more spatially extended than the higher excitation gas, especially on the basis of the southern image. However, a careful source reconstruction is necessary to be confident in the relative spatial distribution of the emission from the two lines; for the northern image it is difficult to determine if the large $r_{3,1}$ values near the image's edge are caused by noise and weak emission or by genuine differences between the CO emission in the two maps (potentially caused by lensing). The values of the line ratio do not appear to change significantly as a function of velocity, with the exception of the reddest velocity channel which is dominated by large $r_{3,1}$ for the brighter northern and southern images. The spatial distribution of line ratios in J0901 is consistent with a picture of the multi-phase gas where the bulk of the molecular ISM is in an extended cool/low-density phase which contains smaller embedded regions of gas in a warm/high-density phase (e.g., Ivison et al. 2011; Thomson et al. 2012).

4.4.2 Resolved Star Formation Law

We examine the spatially resolved Schmidt-Kennicutt relation (Schmidt 1959; Kennicutt 1998) for J0901 using the aligned Hα (Figure 4.6) and matching inner *uv*-radii CO maps. We smoothed the integrated Hα map to have the same spatial resolution as the CO maps and excluded pixels that do not have at least 2σ significance in both maps (as the pixels for all three images were the same size, $0.''125$, no additional re-gridding was necessary). Since dust obscuration causes the Hα luminosity to underestimate the total SFR, we re-scale the Hα surface brightness so that the total integrated SFR from all three images matches

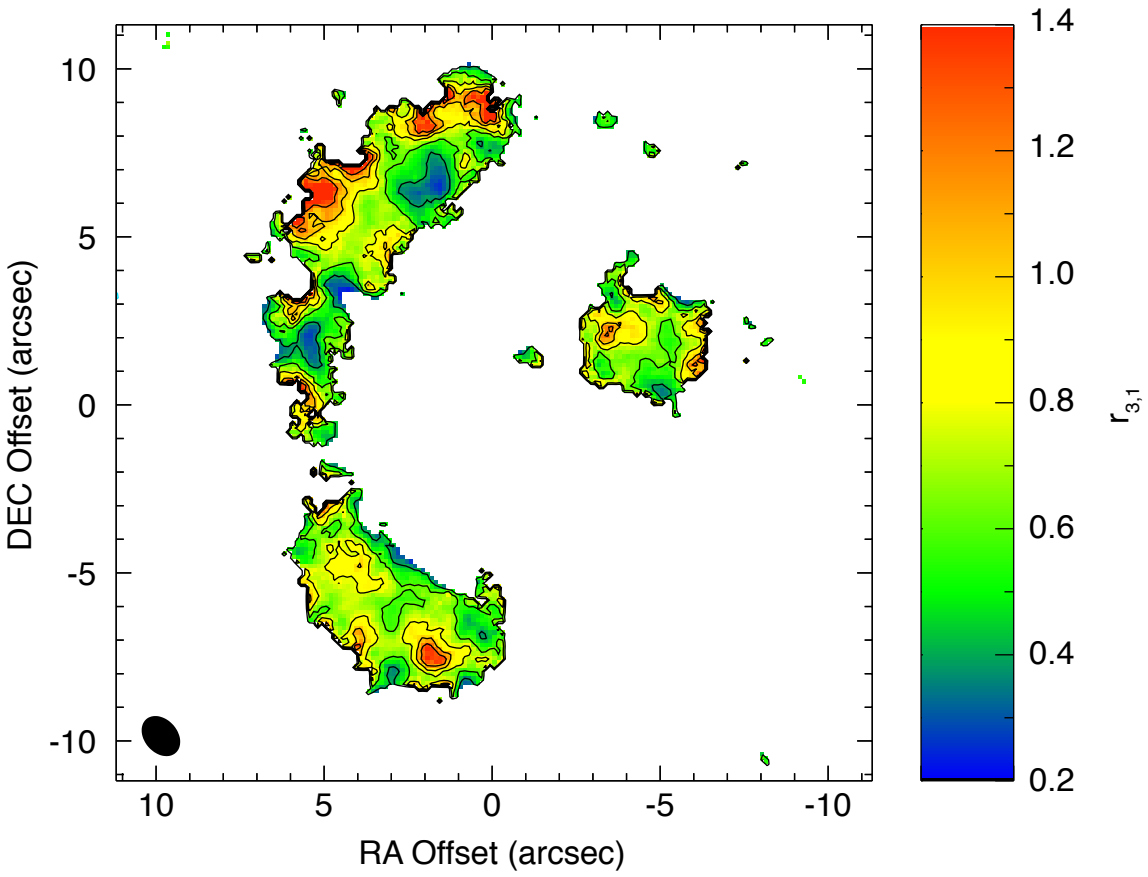

Figure 4.4 Map of the CO(3–2)/CO(1–0) line ratio in units of brightness temperature. The higher resolution CO(1–0) map was made using a Gaussian restoring beam that matched the CO(3–2) data (shown in lower left corner) and matched inner radius of the *uv*-coverage. Negative and $< 2\sigma$ significance pixels have been blanked out, contours are in steps of $\Delta r_{3,1} = 0.2$, and the color mapping is saturated at $r_{3,1} = 1.4$.

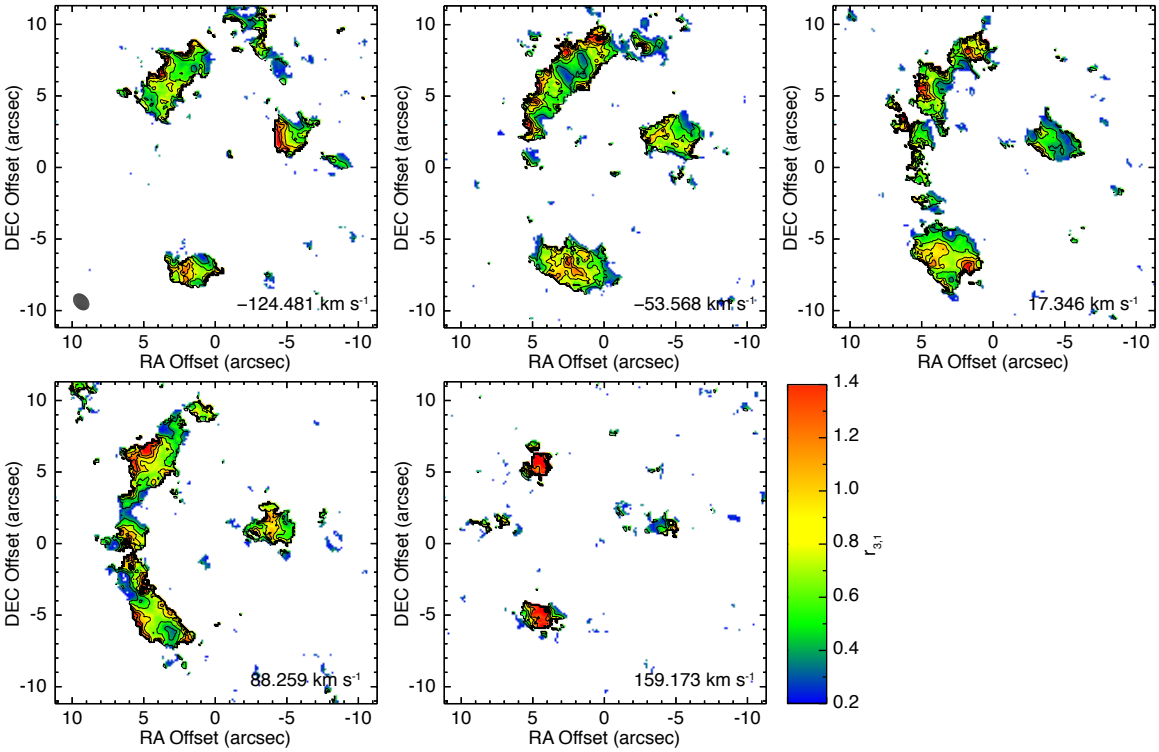

Figure 4.5 Maps of the CO(3–2)/CO(1–0) line ratio in units of brightness temperature for five velocity channels that span the line FWZI. The details of the map construction and color-mapping are the same as Figure 4.4, except pixels are included if they are significant at $> 1\sigma$ in both maps.

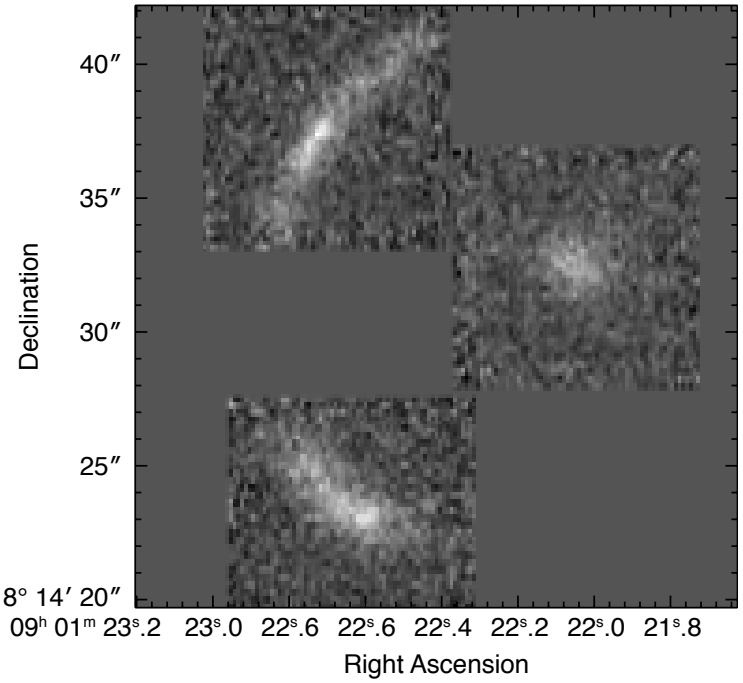

Figure 4.6 Integrated Hα intensity map of J0901. Due to SINFONI's small field of view, the three images of J0901 were observed separately.

the SFR calculated using the magnification-corrected $L_{\rm FIR}$ from Saintonge et al. (2013). The total star formation rate was calculated using the $L_{\rm FIR}$-SFR conversion factor given in Kennicutt (1998) scaled to match the Calzetti et al. (2007) initial mass function (IMF) in order to compare our results to those for local galaxies in Bigiel et al. (2008, 2010). Given that there is good agreement between the Hα and CO line morphologies (indicating that the obscuration is not patchy on large scales), and that Fadely et al. (2010) determined that the AGN in J0901 is not a significant contributor to its FIR luminosity, re-scaling the $\rm SFR_{FIR}$ accurately captures the global SFR properties while still capitalizing on the angular resolution of Hα observations. In Figure 4.7 and 4.8 we show the Schmidt-Kennicutt relation using the minimum uv-radius matched integrated CO(1–0) and CO(3–2) maps. The position of J0901 on the star formation relation depends strongly on the assumed value of the CO-to-H_2 conversion factor. For the disk-like $\alpha_{\rm CO} = 5.6\,M_\odot\,(\rm K\,km\,s^{-1}\,pc^2)^{-1}$, J0901 falls somewhere between the sequence of disks and the sequence of starbursts (e.g., Daddi et al. 2010; Genzel et al. 2010), while lower values of $\alpha_{\rm CO}$ move it further into the sequence of starbursts.

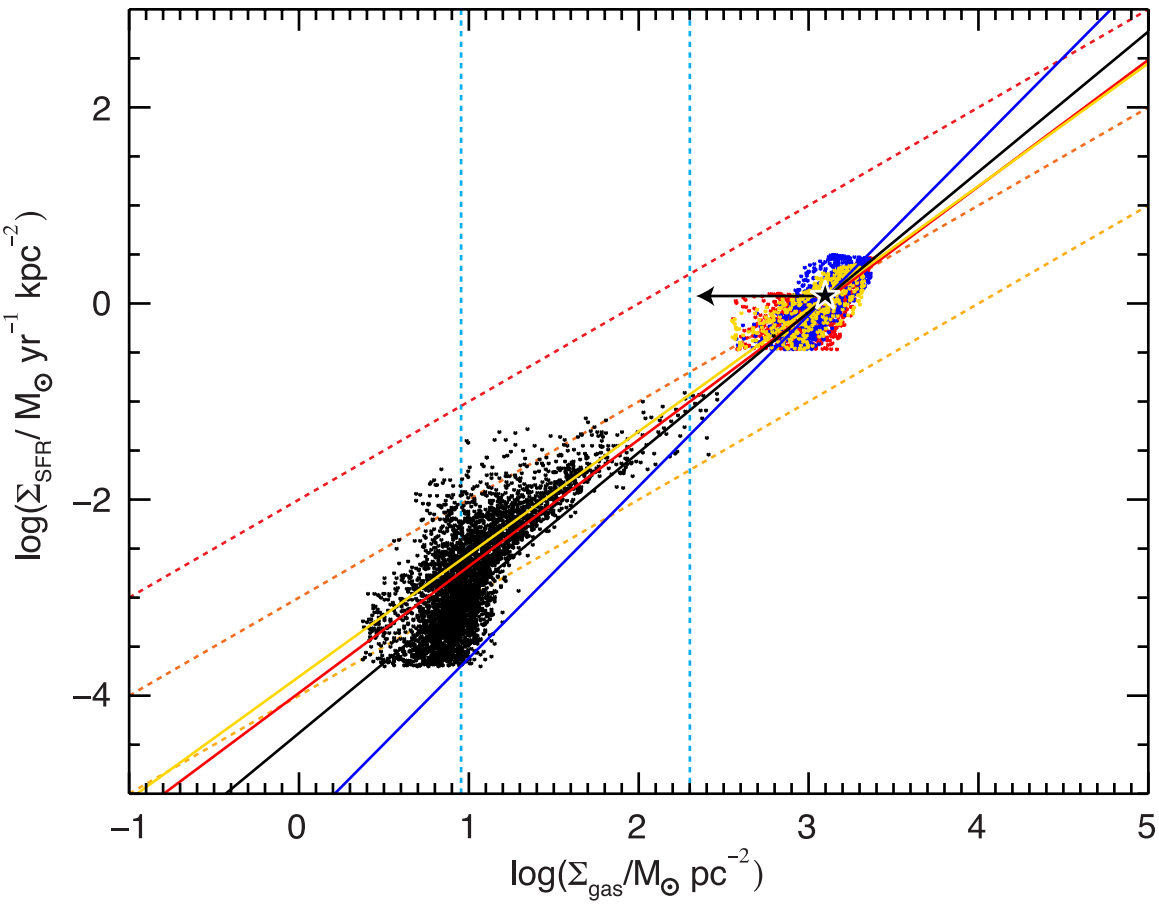

Figure 4.7 Star formation rate surface density as measured by Hα surface brightness (rescaled by the global $\mathrm{SFR_{FIR}/SFR_{H\alpha}}$) vs. CO(1–0)-determined molecular gas mass surface density for J0901 (colored points) and total gas mass surface density for local disk galaxies from Bigiel et al. (2010) (black points; clipped at $2 \times 10^{-4}\,M_\odot\,\mathrm{yr}^{-1}\,\mathrm{kpc}^{-2}$). The average value for J0901 is given by the star, and a power law fit to the resolved surface density points are given by the solid lines. The red, blue, and gold points and solid lines are for the northern, southern, and western images, respectively, while the black line fits the points from all three images. The star formation rate surface density and gas mass surface density have been clipped at the 2σ sensitivity limits. The arrow pointing to the left shows where J0901's locus of points (centered at the average value) would move if the molecular gas mass were calculated using the "starburst" value of α_{CO} instead of the "disk" value (which was assumed for calculating the gas mass). Dotted lines are the same as in Bigiel et al. (2008), where the diagonal lines represent the constant star formation efficiencies required to consume 1% (yellow), 10% (orange), and 100% (red) of the gas in 10^8 years, the left vertical line shows the HI surface density saturation, and the right vertical line marks the proposed transition between star formation laws at $200\,M_\odot\,\mathrm{pc}^{-2}$.

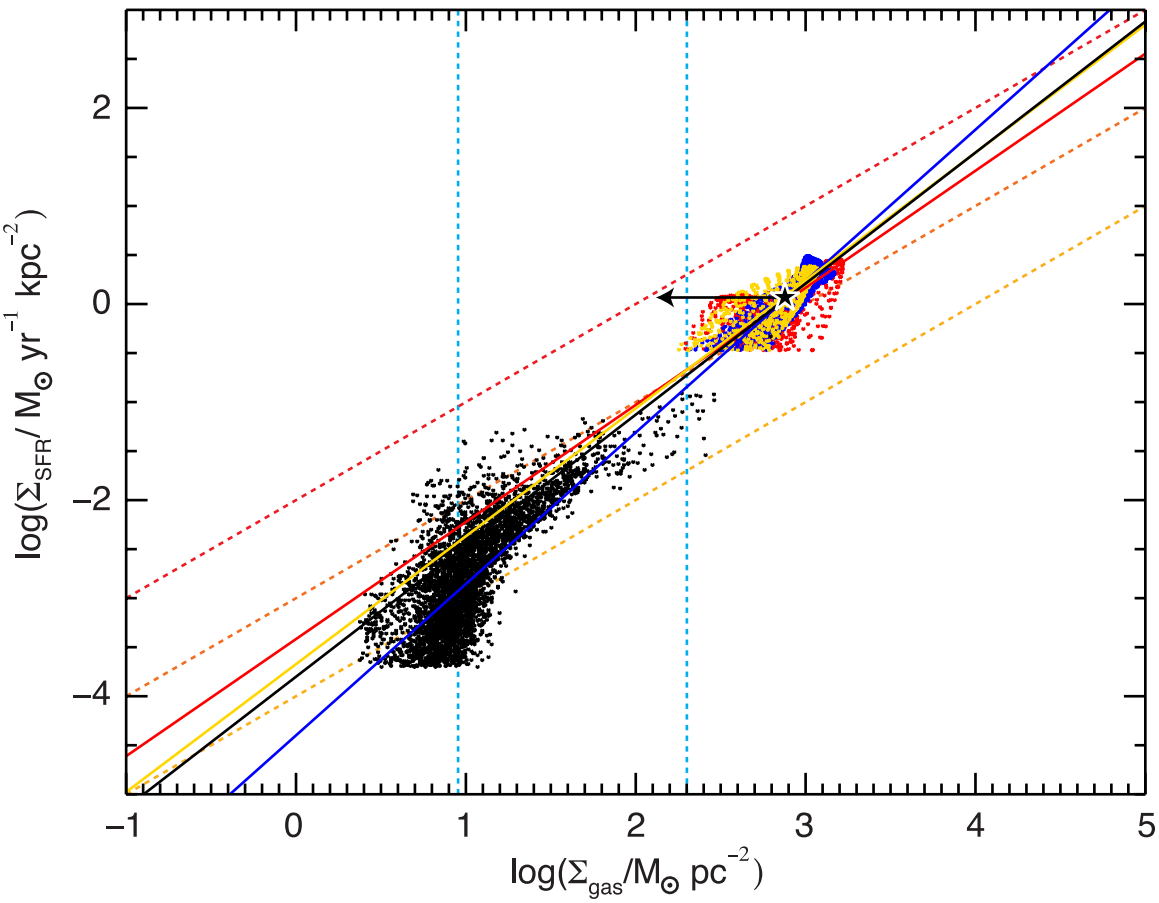

Figure 4.8 Star formation rate surface density as measured by Hα surface brightness (rescaled by the global $\mathrm{SFR_{FIR}/SFR_{H\alpha}}$) vs. CO(3–2)-determined molecular gas mass surface density for J0901. All lines and colors are as described in Figure 4.7.

We fit power laws to the SFR and gas mass surface densities from the combination of all three images of J0901, as well as the three images of J0901 individually. Table 4.3 lists the power law index fits and the one sigma uncertainty for an orthogonal least-squares regression (since the pixels are not independent, the uncertainty has been scaled by the square root of the number of pixels per resolution element). All of the best-fit lines have super-linear indices for both CO transitions, and there are no systematic differences in the best-fit indices between the two CO lines. We also report the best-fit power law indices when using the natural CO(1–0) integrated line map to verify that the additional resolved out flux does not affect our results. While the indices change, they do not do so in a systematic manner. As the plot of $\Sigma_{\rm SFR}$ relative to $\Sigma_{\rm gas}$ looks largely the same as for the *uv*-clipped data (just shifted to slightly larger gas masses), we do not show that plot here.

Narayanan et al. (2011) use hydrodynamic simulations with 3-D non-LTE radiative transfer modeling to predict that the index of the Schmidt-Kennicutt relation should be systematically lower for higher-excitation molecular gas tracers. They argue that the cold gas less directly involved in star formation would be under-luminous in higher-excitation emission lines; therefore, while the intrinsic star-formation relation using a cold gas tracer should have an index of $n = 1.5$, higher excitation emission lines would trace less mass per unit of star formation, resulting in indices closer to $n = 1$. This variation in power law index with molecular phase tracer has been seen observationally (e.g. Sanders et al. 1991; Yao et al. 2003; Gao & Solomon 2004; Narayanan et al. 2005; Bussmann et al. 2008; Graciá-Carpio et al. 2008; Bayet et al. 2009; Iono et al. 2009; Juneau et al. 2009), but these studies do not observe multiple tracers for the same galaxies, nor do they examine the spatially resolved star formation properties. Tacconi et al. (2012) compares the index of the Schmidt-Kennicutt relation using CO(1–0) and CO(3–2) as the gas mass tracers for a large sample of low and high redshift star forming galaxies. While the data for the two CO lines were not from the same galaxies, nor were the CO observations resolved, Tacconi et al. (2012) also found no difference in the power law index for the two CO lines (although their best-fit index is consistent with $n \sim 1$).

In Figure 4.9 we plot the FIR-scaled SFR surface density of each $\geq 2\sigma$ pixel relative to its $r_{3,1}$ value (determined from the *uv*-clipped CO(1–0) map) and find no clear trends,

Table 4.3. J0901 Schmidt-Kennicutt Indices

Image	n_{1-0} (natural)	n_{1-0} (uv-clipped)	n_{3-2}
North	1.05 ± 0.15	1.29 ± 0.22	1.19 ± 0.18
South	1.98 ± 0.24	1.75 ± 0.32	1.54 ± 0.22
West	1.17 ± 0.22	1.25 ± 0.29	1.30 ± 0.28
All	1.32 ± 0.13	1.43 ± 0.17	1.34 ± 0.14

indicating that the SFR surface density does not depend on the gas excitation for the physical scales probed in our images, which is consistent with the unchanged Schmidt-Kennicutt index for the different CO lines. Yao et al. (2003) examines $r_{3,1}$ for a population of infrared bright galaxies in the local universe. While they do not perform a spatially resolved analysis of their sample, they find no correlation in their analogous global values of $r_{3,1}$ and $L_{\rm FIR}$. Given that the Hα map (Figure 4.6) shows less extended emission than either of the CO lines (Figure 4.1), the star formation could be confined to regions where the molecular gas emission is thermalized (i.e., $r_{3,1} = 1$; although thermalized at higher temperatures and densities than found in the outskirts of J0901), or at least appears to be thermalized at the resolution probed by our observations.

4.5 Summary

We present high resolution CO(1–0) and CO(3–2) observations of the strongly lensed galaxy SDSS J0901+1814. The three images of J0901 show clear velocity gradients, indicative of a rotating disk or a merging galaxy. Using the preliminary lensing reconstruction from A. Tagore, we find $M_{\rm gas} = (7.6 \pm 1.7) \times 10^{10} (\alpha_{\rm CO}/0.8)\, M_\odot$ and $M_{\rm dyn} \sin^2(i) = 1.9 \times 10^{10}\, M_\odot$, which implies that J0901 has an inclination angle of $\lesssim 30^\circ \pm 5^\circ$. The integrated CO(3–2)/CO(1–0) line ratio for J0901 is $r_{3,1} = 0.79 \pm 0.12$, similar to the values found for the small number of LBGs that also have CO line measurements (Riechers et al. 2010). Examining the spatial structure of $r_{3,1}$ in J0901, we find that lower values of $r_{3,1}$ are more spatially extended than higher values, supporting the picture where smaller regions of higher excitation gas are embedded in an extended low excitation phase. However, we

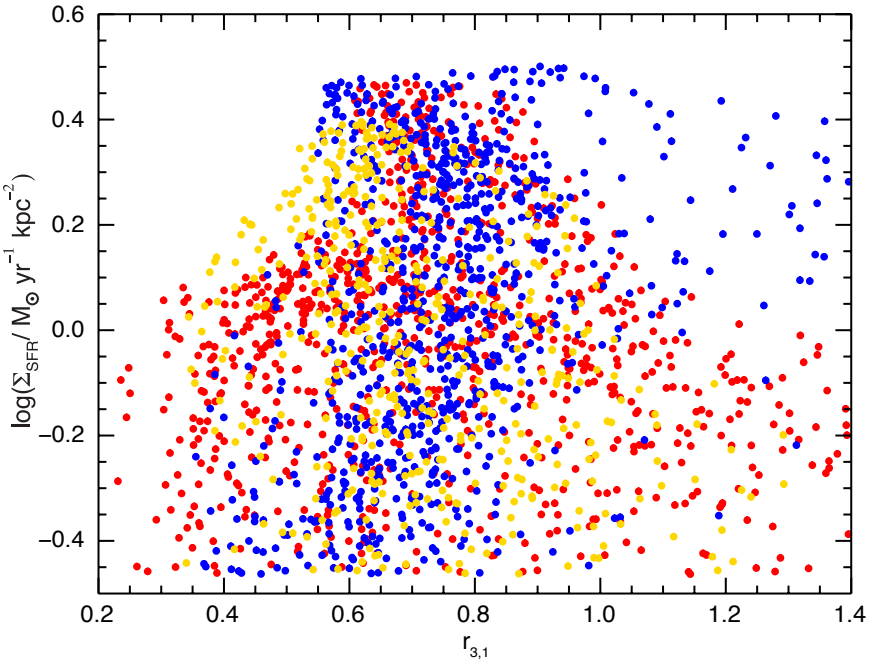

Figure 4.9 Star formation rate surface density as measured by Hα surface brightness (scaled to match the total SFR measured from $L_{\rm FIR}$) vs. $r_{3,1}$ for J0901. The red, blue, and gold points correspond to the northern, southern, and western images, respectively. Each plotted pixel (point) must have $> 2\sigma$ significance in all three maps and have $0.2 < r_{3,1} < 1.4$.

do not find evidence that the higher excitation gas more directly traces the star formation for J0901; the SFR surface density shows no systematic variation with the gas excitation as probed by $r_{3,1}$. We also find no difference in the index of the Schmidt-Kennicutt relation for the two CO lines, contradicting the predictions of Narayanan et al. (2011). The different relative shapes of the CO(1–0) and CO(3–2) lines among the three images imply that J0901 is being differentially lensed; therefore, to be confident in the properties of J0901, we require careful de-lensing to reconstruct the source.

Chapter 5

Conclusions

We present detailed CO observations of three dusty high-redshift star-forming galaxies: SMM J00266+1708 ($z = 2.742$), SMM J14011+0252 ($z = 2.526$), and SDSS J0901+1708 ($z = 2.2586$). In order to obtain the multiple CO lines and spatial resolution necessary to characterize the molecular gas that fuels their rapid star formation, we have carrie out observations using the Green Bank Telescope, the Very Large Array, the Plateau de Bure Interferometer, and the Submillimeter Array. For sources with more than two detected CO lines, we use radiative transfer modeling (assuming a large velocity gradient) to constrain the gas physical conditions. In addition, for galaxies with Hα mapping (a tracer of a galaxy's star formation rate), we examine where sources fall in the resolved Schmidt-Kennicutt relation (i.e., the SFR surface density as a function of the gas mass surface density).

GBT/Zpectrometer observations of the CO(1–0) line allow us to make the first precise redshift measurement for J00266, yielding $z = 2.742$ and validating constraints from *Spitzer*/IRS spectra of PAH features (Valiante et al. 2007). Our followup mapping at the PdBI reveals a second kinematic component in the mid-J lines that was undetected in CO(1–0). Since the two components have different gas excitations (as probed by their different CO line ratios) and have different kinematics (the red component's velocity gradient implies rotational motion, while the blue component does not have resolved bulk gas motions), we conclude that J00266 is likely a merger with a total mass ratio of $(7.7 \pm 3.9)/\sin^2(i)$. The best-fit LVG models of the blue component line ratios (including $r_{3,1} = 1.05 \pm 0.49$) are consistent with a single-phase molecular ISM. For the red component, single-phase LVG models fail to reproduce the measured line ratios (including $r_{3,1} = 0.45 \pm 0.14$), and we conclude that the red component has a multi-phase molecular ISM.

For J14011, we have obtained high-resolution CO(1–0) mapping, which we compare to

existing (low-resolution) mid-J detections from the literature (Downes & Solomon 2003), as well as Hα observations from the VLT/SPIFFI (Tecza et al. 2004). While most SMGs that lack AGN have CO(3–2)/CO(1–0) line ratios of $r_{3,1} \sim 0.6$, J14011 has $r_{3,1} \sim 1$, similar to a small number of local U/LIRGs. Our single-phase LVG model best-fit temperature, $T_{\rm kin} = 20$–$60\,{\rm K}$, is in line with the dust temperature (Wu et al. 2009) and C I-determined temperature (Walter et al. 2011). However, the best-fit densities ($n_{\rm H_2} \sim 10^4$–$10^5\,{\rm cm^{-3}}$, $N_{\rm CO}/\Delta v = 10^{17.00\pm0.25}\,{\rm cm^{-1}\,km^{-1}\,s}$) only produce reasonable CO/H_2 abundances for velocity gradients larger than the globally-determined value (given by the integrated CO line width and source size). We conclude that J14011 likely comprises individual molecular clouds that are unresolved by our observations, consistent with its narrow line width and weak velocity gradient. Based on these gas conditions, we use a Milky Way-like CO-to-H_2 conversion factor and a pixel-to-pixel comparison between the CO and Hα maps to examine the resolved Schmidt-Kennicutt relation for J14011. Even with this choice in gas mass conversion factor, J14011 falls among other SMGs and U/LIRGs, indicating that the offset of starburst galaxies from the local Schmidt-Kennicutt relation may not solely be due to different gas mass conversion factors (in line with the results of Daddi et al. 2010).

For J0901, a strongly-lensed galaxy initially selected on the basis of its rest-frame UV-colors (Diehl et al. 2009), we compare high-resolution CO(1–0), CO(3–2), and Hα mapping of its three images. We find that the global CO(3–2)/CO(1–0) line ratio is $r_{3,1} = 0.79\pm0.12$, consistent with that measured in LBGs (Riechers et al. 2010). Spatially resolved mapping of this line ratio reveals a range of $r_{3,1}$ values, where the lower-excitation gas (lower $r_{3,1}$ values) appears to be more spatially extended than the higher-excitation gas (higher $r_{3,1}$ values). While careful lens modeling is required to reconstruct the source-plane image of J0901 (the variation in the relative CO(1–0) and CO(3–2) line profiles between the three images is indicative of differential lensing), it is likely that J0901 contains a multi-phase molecular ISM with substantial regional variations in the gas physical conditions. Using a pixel-to-pixel comparison between the Hα and CO maps, we examine the spatially resolved Schmidt-Kennciutt relation in J0901. Power-law fits to SFR and gas mass surface densities for the three images of J0901 (fitted separately or combined) using both CO lines produce consistent super-linear indices of $n \sim 1.5$. In contrast to the predictions of Narayanan et al.

(2011), we do not find a systematic difference between the power-law indices of the two CO lines.

Our CO observations illustrate that dusty star-forming galaxies at high redshift have a diversity of physical properties. While submillimeter-selected galaxies are largely characterized as major merger driven starbursts, of the galaxies studied here, J00266 is the only confirmed merger. The kinematics and/or gas conditions of J14011 and J0901 (as well as one component of J00266) suggest rotating structures that could arise from either disks or late-stage mergers, indicating that large IR luminosities do not correspond to a single well-defined interaction state. While the large IR luminosities of these three galaxies suggest they have substantial dust components, their degrees of obscuration appear to differ. Previous attempts to identify an optical counterpart for J00266 produced mostly upper limits and a faint detection in K (Frayer et al. 2004), suggesting near-total obscuration, whereas both J0901 and J14011 are detected in Hα (the latter by Tecza et al. 2004), suggesting significantly less obscuration than that of J00266. In addition, our small sample of dusty starbursts has a wide range in measured CO(3–2)/CO(1–0) line ratios ($0.45 < r_{3,1} < 1.0$) compared to the previously observed distribution for SMGs ($r_{3,1} = 0.64 \pm 0.08$), including a wide range of $r_{3,1}$ values within a single source, J0901. These observations, coupled with those of additional dusty disks (e.g., Swinbank et al. 2011; Hodge et al. 2012) and theoretical studies (e.g., Hayward et al. 2013), suggest that galaxy samples selected simply on IR luminosity do not trace a homogenous population of merging galaxies, and instead encompass a wide range of dynamical and gas excitation states[1].

Characterizations of the molecular gas content and star formation properties of SMGs and other high-redshift galaxies are frequently complicated by the choice of CO-to-H_2 conversion factor, $\alpha_{\rm CO}$. Typically the $\alpha_{\rm CO}$ measured in local U/LIRGs is used in the analysis of SMGs. However, based on the LVG modeling and dynamics of J14011, we have found at least one SMG for which the U/LIRG-like conversion factor is strongly disfavored. This suggests that the bimodal choice in $\alpha_{\rm CO}$ may not be the sole cause of the offset between starbursts and disks in the Schmidt-Kennicutt relation. More detailed CO observations (or

[1]While J0901 was not *initially* selected on the basis of its IR luminosity, it is sufficiently bright to be considered a ULIRG.

observations of other gas tracer species) are necessary to accurately capture the molecular gas physical conditions and dynamics, which will help us better constrain the choice of $\alpha_{\rm CO}$ and evaluate models with continuous forms of $\alpha_{\rm CO}$ (e.g., Narayanan et al. 2012). LVG models need several CO line measurements to constrain the gas physical conditions, including CO(1–0) in order to trace the cold and low-density molecular gas; multi-J CO observations are especially necessary given the larger number of model parameters that need to be constrained for the multi-phase gas observed in many high-redshift starbursts (including J0901 and the red component of J00266). In addition, as illustrated by the LVG analyses of J00266 and J0901, using global average velocity gradients in the analysis of LVG models does not seem to produce realistic values of the CO-to-H_2 abundance (among other parameters). Therefore, in addition to multi-J mapping, high-resolution observations are necessary to better constrain the local velocity gradients in high-redshift galaxies.

In addition to the overall normalization uncertainties in the Schmidt-Kenicutt relation due to the choice of CO-to-H_2 conversion factor, the intrinsic slope of the star formation rate relative to gas mass surface density is an important parameter to constrain in order to test models of star formation. Many of the uncertainties in the Schmidt-Kennicutt relation arise from using globally averaged surface densities (or just the gas mass and SFR tracer luminosities without additional scaling factors) or from making comparisons between molecular species that may trace different regimes of gas excitation. The best way to test if the excitation of the gas tracer significantly affects the index of the star formation relation (e.g., Narayanan et al. 2011) is to make matched observations for the same galaxy, or same set of galaxies, using different excitation gas mass tracers. Our CO(1–0) and CO(3–2) observations of J0901 satisfy this criterion of well-matched observations; we find no systematic difference between the indices of the Schmidt-Kennicutt relation measured from these two CO lines. Additional observations of different excitation gas tracers in the same galaxy (or galaxy set) are important to determine if the lack of excitation dependence observed in J0901 is unique to this system. In addition, for J0901 in particular, we hope to add observations of the CO(7–6) line to help rule out the possibility that the CO(1–0) and CO(3–2) lines do not trace gas of different enough excitation.

In the near future, the increased sensitivity afforded by the powerful Atacama Large Millimeter/submillimeter Array (ALMA) will help make the necessary resolved multi-excitation observations more common, although the VLA will continue to play a significant role in observing high-redshift CO(1–0). In addition, using gravitational lensing to achieve increased spatial resolution and efficient detections of (intrinsically) fainter sources is an important technique for studying high-redshift galaxies. Targeting strongly-lensed galaxies will be especially important for enabling detailed analyses of gas and star formation conditions *within* individual galaxies, where detecting molecular-cloud scale features at high redshifts will be difficult even with ALMA. The tighter constraints on molecular gas excitation and parameters like $\alpha_{\rm CO}$ provided by the detailed analyses of small samples of high-redshift galaxies will be especially important for more accurate interpretations of upcoming large statistical surveys of the molecular gas content of high-redshift galaxies.

Appendix A

Basic Calculations

A.1 Integrated Line Flux

For a CO line with significant detections in multiple individual channels, the line flux is derived by integrating over the area of the source and the line width. In practice, this translates to

$$S\Delta v\,[\mathrm{Jy\,km\,s^{-1}}] = \sum_{\mathrm{Pixels}} \sum_{\mathrm{Channels}} S_\nu(x,y)\,[\mathrm{Jy\,beam^{-1}}]\Delta v_{\mathrm{chan}}\,[\mathrm{km\,s^{-1}}] \\ /N\,[\mathrm{pixels\,beam^{-1}}], \tag{A.1}$$

where the units are given in square brackets and $S_\nu(x,y)$ represents the line data cube. In the IDL code used in this thesis, the area over which to calculate the flux is chosen first and is held constant from channel to channel. That region is a rectangular box, selected by eye, which is large enough to encompass all the source emission (including low significance wings) in all channels. This first summation creates the spectrum:

$$S_\nu\,[\mathrm{Jy}] = \sum_{\mathrm{Pixels}} S_\nu(x,y)\,[\mathrm{Jy\,beam^{-1}}]/N\,[\mathrm{pixels\,beam^{-1}}]. \tag{A.2}$$

Then the flux in the spectrum is added over the channels that make up the line (also identified by eye and chosen to include line wings, but generally stopping when the flux is consistent with the noise).

In order to obtain upper limits for spectral lines that were not detected in the individual channel maps, integrated line maps were made using the multi-frequency synthesis method in CASA, and the channel ranges were selected based on the velocity ranges of the other

detected CO lines. The integrated line flux is then given by

$$S\Delta v\,[\mathrm{Jy\,km\,s^{-1}}] = \sum_{\mathrm{Pixels}} S(x,y)\,[\mathrm{Jy\,beam^{-1}}]\Delta v_{\mathrm{total}}\,[\mathrm{km\,s^{-1}}]/N\,[\mathrm{pixels\,beam^{-1}}], \quad (A.3)$$

where $\Delta v_{\mathrm{total}}$ is the total velocity width used in making the integrated line map. The use of multi-frequency synthesis in this manner is only recommended for sources that lack velocity structure on the angular scales probed by our observations. In the case that the source may have resolved velocity structure, Equation A.1 should be used. If the integrated line remains undetected, we report 3σ upper limits given by:

$$3\sigma_{S\Delta v}\,[\mathrm{Jy\,km\,s^{-1}}] = 3\sigma_{S(x,y)}\,[\mathrm{Jy\,beam^{-1}}]\Delta v_{\mathrm{total}}\,[\mathrm{km\,s^{-1}}], \quad (A.4)$$

where we assume a source size of one beam (in the case that we expect the source to be unresolved).

To convert from integrated line flux to line luminosity, we use the equation from Solomon & Vanden Bout (2005):

$$L'_{\mathrm{CO}}\,[\mathrm{K\,km\,s^{-1}\,pc^2}] = 3.25\times10^7 S\Delta v\,[\mathrm{Jy\,km\,s^{-1}}]\nu_{\mathrm{obs}}^{-2}\,[\mathrm{GHz}]D_{\mathrm{L}}^2\,[\mathrm{Mpc}](1+z)^{-3}. \quad (A.5)$$

A.2 Error Estimates

For the measured values in Equations A.1–A.3, and A.5, we also need to derive uncertainties. In Section A.6, I include a sample derivation of the statistical uncertainty for integrated line flux. For the integrated line flux given by Equation A.1, the statistical error is given by

$$\begin{aligned}\sigma_{S\Delta v}\,[\mathrm{Jy\,km\,s^{-1}}] &= \overline{\sigma_{S_\nu(x,y)}}\,[\mathrm{Jy\,beam^{-1}}]\Delta v_{\mathrm{chan}}\,[\mathrm{km\,s^{-1}}] \\ &\quad\times\sqrt{n_{\mathrm{pixels}}n_{\mathrm{chans}}/N\,[\mathrm{pixels\,beam^{-1}}]}, \end{aligned} \quad (A.6)$$

where $\overline{\sigma_{S_\nu(x,y)}}$ is the average noise of the channel maps in the data cube, $n_{\rm pixels}$ is the number of pixels summed over when calculating the flux in each channel, and $n_{\rm chans}$ is number of channels summed over. This equation is derived assuming that $\sigma_{S_\nu(x,y)}$ is the same for each channel and pixel in the cube, which is not necessarily true in reality. In practice, $\overline{\sigma_{S_\nu(x,y)}}$ is calculated by finding the RMS pixel value (in Jy beam^{-1}) for regions in the map that exclude the source (or any other bright sources in the field) for each channel, and then the mean RMS is used for $\overline{\sigma_{S_\nu(x,y)}}$. Typically the channel-to-channel variation in the noise is not very large (with the possible exception of bandpass edge channels, which are excluded), which justifies the use of the mean rather than median value.

Following the derivation for Equation A.6 (Section A.6), the statistical uncertainties for individual channels in the spectrum (Equation A.2) are given by

$$\sigma_{S_\nu}\,[\mathrm{Jy}] = \sigma_{S_\nu(x,y)}\,[\mathrm{Jy\,beam^{-1}}]\sqrt{n_{\rm pixels}/N\,[\mathrm{pixels\,beam^{-1}}]}, \tag{A.7}$$

where the uncertainty per channel is used rather than using the channel-averaged noise (assuming there is sufficient signal-free area in the map where the RMS variation can be measured). The statistical uncertainty for the alternative integrated line flux (where channels are combined at the cleaning stage within CASA; Equation A.3) is given by

$$\sigma_{S\Delta v}\,[\mathrm{Jy\,km\,s^{-1}}] = \sigma_{S(x,y)}\,[\mathrm{Jy\,beam^{-1}}]\Delta v_{\rm total}\,[\mathrm{km\,s^{-1}}]\sqrt{n_{\rm pixels}/N\,[\mathrm{pixels\,beam^{-1}}]}, \tag{A.8}$$

where $\sigma_{S(x,y)}$ is computed from the RMS of the integrated line map (excluding regions with obvious sources).

While the above equations provide the statistical uncertainties for these line measurements, it is important to include other sources of uncertainty as well. These are typically dominated by the flux calibration uncertainty, which is assumed to be some percentage of the measured flux. The exact percentage chosen is informed by prior experience observing in a given band. For the 1 mm band at the SMA, the flux calibration is accurate to $\sim 20\%$ (found in assorted literature papers). For the PdBI, the flux calibration errors are expected to be $\sim 15\%$ for the 2 mm band and $\sim 10\%$ for the 3 mm band (recommended

by A. Baker). For the VLA, in the high-frequency bands (1 cm/ Ka in my case), the flux calibration is accurate to $\sim 10\%$ (found in the online VLA documentation about special issues for high-frequency observations). The final reported uncertainties are the statistical uncertainties and flux calibration uncertainties added in quadrature.

The errors in $L'_{\rm CO}$ and $r_{J,J'}$ come from the standard propagation of errors formula:

$$\sigma^2_{f(x)} = \sum_i \sigma^2_{x_i} \left(\frac{\partial f}{\partial x_i}\right)^2. \tag{A.9}$$

As $L'_{\rm CO}$ is simply proportional to the integrated line flux, the errors just need to be carried through Equation A.5.

A.3 Dynamical Mass

The dynamical mass is calculated in one of two ways depending on whether the kinematics of the galaxy of interest are dispersion-dominated or disk-like. For dispersion-dominated kinematics, virialization is assumed, giving

$$\left(\frac{M_{\rm dyn}}{M_\odot}\right) = \frac{5\sigma^2 r}{G} = 1.2\times10^{10}\left(\frac{\sigma}{100\,{\rm km\,s^{-1}}}\right)^2\left(\frac{r}{\rm kpc}\right) \tag{A.10}$$

where σ is the velocity dispersion (given by the integrated line FWHM$/2\sqrt{2\ln(2)}$) and r is the source radius (given by the Gaussian fit to the image). If the source is a rotating disk, then the dynamical mass is given by

$$\left(\frac{M_{\rm dyn}\sin^2(i)}{M_\odot}\right) = \frac{r v^2_{\rm circ}}{G} = 233.5\left(\frac{r}{\rm pc}\right)\left(\frac{v_{\rm circ}}{\rm km\,s^{-1}}\right)^2 \tag{A.11}$$

where i is the inclination angle of the disk, r is the radius of the disk, and $v_{\rm circ}$ is the component of the galaxy's circular velocity along our line of sight. For most observations, there is insufficient resolution to determine $v_{\rm circ}$. In practice, I use half of the line profile FWHM.

A.4 Gas Mass Surface Density

In order to calculate the gas mass surface density of each pixel, I scale the CO integrated line map using

$$\begin{aligned}\Sigma_{\rm gas}(x,y)\,[M_\odot\,{\rm pc}^{-2}] &= S(x,y)\,[{\rm Jy\,beam}^{-1}]\Delta v_{\rm chan}\,[{\rm km\,s}^{-1}] \\ &\times\frac{1\,{\rm beam}}{A_{\rm beam}\,[{\rm arcsec}^2]}\left(\frac{1''}{D_{\rm A}\,[{\rm pc}]}\right)^2 \\ &\times 3.25\times10^7(D_{\rm L}\,[{\rm Mpc}])^2(\nu_{\rm obs}\,[{\rm GHz}])^{-2}(1+z)^{-3} \\ &\times\alpha_{\rm CO}\,[{\rm M}_\odot\,({\rm K\,km\,s}^{-1}\,{\rm pc}^2)^{-1}]\times 1.36 \qquad \text{(A.12)}\end{aligned}$$

where $\Sigma_{\rm gas}(x,y)$ is the gas mass surface density for a pixel, $S(x,y)$ is a pixel value in the CO(1–0) map produced by suming over the line channels, and $A_{\rm beam}$ is the area of the beam in square arc seconds. The $1''/D_{\rm A}$ [pc] term is the physical angular diameter distance that corresponds to $1''$ at the appropriate redshift. The second line is to convert to line luminosity, and the last line is to convert to mass (including a factor of 1.36 to account for helium).

A.5 Star Formation Rate Surface Density

The SFR surface density, $\Sigma_{\rm SFR}$ is calculated from the integrated Hα maps as follows:

$$\begin{aligned}\Sigma_{\rm SFR}(x,y)\,[{\rm M}_\odot\,{\rm yr}^{-1}\,{\rm kpc}^{-2}] &= S(x,y)\,[{\rm W}\,\mu{\rm m}^{-1}\,{\rm m}^{-2}]\Delta\lambda_{\rm chan}\,[\mu{\rm m}]\times10^7\,[{\rm W\,erg}^{-1}\,{\rm s}] \\ &\times 4\pi(D_{\rm L}\,[{\rm m}])^2 10^{(A_\lambda/2.5)}(\Delta_{\rm pix}\,[{\rm kpc}])^{-2} \\ &\times 7.9\times10^{-42}\,[{\rm M}_\odot\,{\rm yr}^{-1}\,{\rm erg}^{-1}\,{\rm s}]\times C_{\rm IMF}\cos(i). \qquad \text{(A.13)}\end{aligned}$$

$S(x,y)$ is a pixel value in the integrated Hα data cube, before we multiply by the channel width. The second line integrates over the surface of the sphere define the luminosity distance between us and the source, corrects for extinction, and factors in the pixel size converted from arcseconds to kiloparsecs using the appropriate angular diameter distance.

The last line contains the Kennicutt (1998) conversion factor from Hα luminosity to solar masses per year, a correction factor for changing from the Salpeter IMF Kennicutt (1998) assumed to a different IMF (for a Kroupa IMF, appropriate for matching the Bigiel et al. 2008 plots, this factor is 0.63), and a correction for the galaxy inclination. In practice, the sources I use are of unknown inclination, so no correction is applied for viewing angle. In addition, since the objects I study are dusty, I expect the Hα-determined SFR to underestimate the actual SFR, so rather than correct for extinction, I re-scale by the ratio of the ratio of the total $\mathrm{SFR_{FIR}}/\mathrm{SFR_{H\alpha}}$. The extinction value, if necessary, can be determined from the extinction curves in Howarth (1983) for the measured color excess, $E(B-V)$ (as implied by the Balmer decrement, for example). In addition, this equation assumes no magnification by gravitational lensing; pixel sizes and flux scales would need to be corrected appropriately if the source is lensed. However, when using the $\mathrm{SFR_{FIR}}/\mathrm{SFR_{H\alpha}}$ re-scaling, as long as the FIR luminosity was corrected for magnification, the other normalization factors in this equation do not matter.

A.6 Example Uncertainty Derivation

As deriving the uncertainties of measured line fluxes from radio maps can be slightly tricky due the nonintuitive units of flux per unit beam area in the map, below is an example for how to derive the integrated line flux and integrated line flux uncertainty (Equations A.1 and A.6).

$$
\begin{aligned}
S\Delta v\,[\mathrm{Jy\,km\,s^{-1}}] &= \int\int S_\nu(x,y)\,[\mathrm{Jy\,beam^{-1}}]d\Omega\,[\mathrm{beam}]dv_{\mathrm{chan}}\,[\mathrm{km\,s^{-1}}] && \text{(A.14)}\\
&= \sum_{\mathrm{Beams}}\sum_{\mathrm{Chans}} S_\nu(x,y)\,[\mathrm{Jy\,beam^{-1}}]\Delta v_{\mathrm{chan}}\,[\mathrm{km\,s^{-1}}] && \text{(A.15)}\\
&= \sum_{\mathrm{Pix}}\sum_{\mathrm{Chans}} S_\nu(x,y)\,[\mathrm{Jy\,beam^{-1}}]\Delta v_{\mathrm{chan}}\,[\mathrm{km\,s^{-1}}] && \text{(A.16)}\\
&\quad /N\,[\mathrm{pixels\,beam^{-1}}]
\end{aligned}
$$

Using the propagation of errors formula starting at the *second* of that equation set:

$$\sigma^2_{S\Delta v}\,[\mathrm{Jy\,km\,s^{-1}}]^2 = \sum_{\mathrm{Beams}}\sum_{\mathrm{Channels}} \sigma^2_{S_\nu(x,y)}\,[\mathrm{Jy\,beam^{-1}}]^2 \Delta v^2_{\mathrm{chan}}\,[\mathrm{km\,s^{-1}}]^2 \quad \text{(A.17)}$$

$$= n_{\mathrm{beams}} n_{\mathrm{chans}} \sigma^2_{S_\nu(x,y)}\,[\mathrm{Jy\,beam^{-1}}]^2 \Delta v^2_{\mathrm{chan}}\,[\mathrm{km\,s^{-1}}]^2. \quad \text{(A.18)}$$

Taking the square root of this equation, and using the fact that $n_{\mathrm{beams}} = n_{\mathrm{pixels}}/N\,[\mathrm{pixels\,beam^{-1}}]$, we get:

$$\sigma_{S\Delta v}\,[\mathrm{Jy\,km\,s^{-1}}] = \sigma_{S_\nu(x,y)}\,[\mathrm{Jy\,beam^{-1}}] \Delta v_{\mathrm{chan}}\,[\mathrm{km\,s^{-1}}] \sqrt{n_{\mathrm{pix}} n_{\mathrm{chans}}/N\,[\mathrm{pixels\,beam^{-1}}]}. \quad \text{(A.19)}$$

Appendix B

LVG Analysis

B.1 Comparing to Measurements

Since the number of parameters necessary to create a two-phase LVG model outnumbers our measurements for J00266, and these measurements have significant uncertainties, finding a single solution for the physical conditions of the two phases is unrealistic. We therefore take a Bayesian approach with the aim of computing likelihood densities for the parameter space, similar to what is described in Ward et al. (2003), but for line ratios instead of individual line measurements. If the measured line ratios are given by the vector $\boldsymbol{R}$ and their corresponding errors by $\boldsymbol{\sigma}$, while the model line ratio is given by $\boldsymbol{M}$, and we assume our measurements are well-described by Gaussian errors, then (reproducing Equation 3 of Ward et al. 2003) the likelihood of measuring our line ratios for a two-phase system with parameter values $\boldsymbol{a}$ is given by

$$P(\boldsymbol{R}|\boldsymbol{\sigma},\boldsymbol{a}) = \prod_i \frac{1}{\sqrt{2\pi}\sigma_i} \exp\left[-\frac{1}{2}\left(\frac{R_i - M_i(\boldsymbol{a})}{\sigma_i}\right)^2\right]. \tag{B.1}$$

This formalism allows us to calculate the posterior probability, the likelihood of the system's being described by particular parameter values given our measured line ratios and errors, by

$$P(\boldsymbol{a}|\boldsymbol{R},\boldsymbol{\sigma}) = \frac{P(\boldsymbol{a})P(\boldsymbol{R}|\boldsymbol{\sigma},\boldsymbol{a})}{\int d\boldsymbol{a} P(\boldsymbol{a})P(\boldsymbol{R}|\boldsymbol{\sigma},\boldsymbol{a})}, \tag{B.2}$$

where $P(\boldsymbol{a})$ is the prior, and the bottom integral is for normalization. In our case, we choose a uniform prior in the *log* of input model parameters to compensate for their logarithmic sampling of parameter space, except for temperature where we have linear sampling and

therefore set the prior to unity. We also use the prior to enforce the simple two-phase model by setting $P(\boldsymbol{a}) = 0$ where $T_c \geq T_w$.

Given the posterior probabilities, we can then calculate the likelihood density of any one parameter (or the likelihood density distribution of a pair of parameters) by integrating the posterior over the uninteresting parameters:

$$P_{a_i}(x) = \int d\boldsymbol{a} P(\boldsymbol{a}|\boldsymbol{R}, \boldsymbol{\sigma}) \delta(a_i - x). \tag{B.3}$$

B.2 Computational Method

The single-phase LVG line luminosity libraries are read into IDL as a series of three-dimensional arrays, one for each measured CO line, where each dimension corresponds to a different assumed value of T, $n_{\mathrm{H_2}}$, and $N_{\mathrm{CO}}/\Delta v$. The fractional filling factors are calculated on the fly during the course of the calculation.

Once the parameter(s) of interest is (are) chosen, an empty array is generated with the same dimension as for that (those) parameter(s) in the single-phase model array. The integrands of Equations B.2 and B.3 are then calculated inside of a nested loop, iterating over T, $n_{\mathrm{H_2}}$, $N_{\mathrm{CO}}/\Delta v$, and f for the molecular gas phase of interest (either cold or warm). These loops select their corresponding model values of the line luminosity from the single-phase model cubes, and compute Equation B.1 for the entire array of parameter choices for the second phase simultaneously (an additional loop iterating over the measured line ratios is necessary to compute the product in Equation B.1, which has the benefit of making the code useful for an arbitrary number of line measurements). This method allows us to reduce the number of nested loops by three, drastically speeding up the program run time. This new array of probability densities is then multiplied by the appropriate spacing in each of the seven parameters (recalling that some are evenly sampled in their *logarithm*, which makes the step sizes, $d\boldsymbol{a}$, variable across the array), and then non-physical models are set to zero (this is effectively multiplying by the prior). This array is then totaled, and its value is added to the likelihood array of our parameter(s) of interest at the correct position. Once this series of loops has been completed, the resulting array is divided by the sum of its

components (which is the normalization given in the denominator of Equation B.2). The resulting normalized likelihood distribution can then be plotted.

B.3 LVG Modeling Derivation for Including the CMB

While radiation from CMB can be safely ignored at low redshift, at high redshift the CMB temperature becomes comparable to excitation temperatures of low and mid-J CO lines and must be included in the radiative transfer analysis. Using the escape probability formalism, the average radiation field at a specific frequency, ν, is given by

$$J_\nu = (1 - \beta_\nu)S_\nu + \beta_\nu S_\nu(T_{\rm CMB}), \tag{B.4}$$

where $S_\nu(T_{CMB})$ is the blackbody radiation at frequency of interest for the CMB at the appropriate redshift ($T_{CMB} = 2.735(1+z)$ K), and S_ν is the radiation caused by the CO line emission ($S_{u,l} = \chi_u A_{u,l}/(\chi_l B_{l,u} - \chi_u B_{u,l})$). Adopting the notation of the J. Ward thesis, we can substitute Equation B.4 into the steady-state rate balance equation (Equation E.4 of the J. Ward thesis—sans typo), and arrive at a new version of Equation E.17:

$$\begin{aligned}
&\sum_i \chi_i C_{i,j} - \chi_J \sum_k C_{j,k} + \chi_{J+1}[A_{J+1,J}\beta_{J+1,J} + B_{J+1J}\beta_{J+1,J}S_{J+1,J}(T_{CMB})] \\
&\quad - \chi_J[B_{J,J+1}\beta_{J+1,J}S_{J+1,J}(T_{CMB}) + A_{J,J-1}\beta_{J,J-1} + B_{J,J-1}\beta_{J,J-1}S_{J,J-1}(T_{CMB})] \\
&\quad + \chi_{J-1}B_{J-1,J}\beta_{J,J-1}S_{J,J-1}(T_{CMB}) = 0.
\end{aligned} \tag{B.5}$$

Equation B.5 can also be expressed as the matrix equation $\boldsymbol{F}(\boldsymbol{\beta}, T_{kin}, T_{CMB}) \cdot \boldsymbol{\chi} = \boldsymbol{I}$, where $\boldsymbol{I}$ is the identity matrix. Following J. Ward's derivation, we perform a first order Taylor expansion of β about a reasonable guess for χ, substituting equations E.22 through E.24 into Equation B.5, keeping only first order terms in $\delta\chi$. After a bit of work, our new rate balance equation becomes

$$
\begin{aligned}
&\boldsymbol{F}(\boldsymbol{\beta}, T_{kin}, T_{CMB}) \cdot (\boldsymbol{\chi} + \delta\boldsymbol{\chi}) \\
&+ \delta\chi_{J-1}[\chi_{J-1}B_{J-1,J}S_{J,J-1}(T_{CMB})\alpha_J - \chi_J A_{J,J-1}\alpha_J - \chi_J B_{J,J-1}S_{J,J-1}(T_{CMB})\alpha_J] \\
&+ \delta\chi_J[\chi_{J-1}B_{J-1,J}S_{J,J-1}(T_{CMB})\eta_J - \chi_J A_{J,J-1}\eta_J - \chi_J B_{J,J+1}S_{J+1,J}(T_{CMB})\alpha_{J+1} \\
&- \chi_J B_{J,J-1}S_{J,J-1}(T_{CMB})\eta_J + \chi_{J+1}A_{J+1,J}\alpha_{J+1} + \chi_{J+1}B_{J+1,J}S_{J+1,J}(T_{CMB})\alpha_{J+1}] \\
&+ \delta\chi_{J,J+1}[\chi_{J+1}B_{J+1,J}S_{J+1,J}(T_{CMB})\eta_{J+1} + \chi_{J+1}A_{J+1,J}\eta_{J+1} \\
&- \chi_J B_{J,J+1}S_{J+1,J}(T_{CMB})\eta_{J+1}] = 0. \qquad \text{(B.6)}
\end{aligned}
$$

The long part of Equation B.6 can also be re-written in matrix form as $\boldsymbol{G}(\boldsymbol{\chi}, \boldsymbol{\alpha}, \boldsymbol{\eta}, T_{CMB}) \cdot \delta\boldsymbol{\chi}$. These new LVG matrices can be solved in the same manor as before: require the sum of $\delta\chi_J$ to be equal to zero to preserve the normalization of the level populations, break the row degeneracy by setting the last row of $\boldsymbol{F}$ and $\boldsymbol{G}$ to 0 and 1 respectively, and iteratively add $\delta\boldsymbol{\chi}$ to $\boldsymbol{\chi}$ until the level populations converge. Once the level populations have been determined, the escape probability can be calculated, and those values can be substituted into $\Lambda_{J,J-1} = h\nu_{J,J-1}A_{J,J-1}n_{\mathrm{H_2}}f_{\mathrm{CO}}\chi_J\beta_{J,J-1}$ to give us the resulting line luminosities for our chosen set of physical conditions.

Appendix C

Priors for the LVG Analysis

C.1 Brightness Temperature

One physically motivated prior is a cut on the CO line brightness temperature; if the brightness temperature is low compared to the kinetic temperature of the molecular gas we would not observe the line. Our prior would then be given by $T_{\rm B} > \alpha T_{\rm kin}$ for all detected lines, where we must choose some value of α (we use $\alpha = 1$).

However, the LVG code does not output model line brightness temperatures. It outputs the line luminosity density, Λ, divided by the CO to H_2 ratio, $X_{\rm CO}$ (which I will define as Λ'). We must therefore convert our brightness temperature cut into units of Λ'.

The brightness temperature is defined by

$$T_{\rm B} = \frac{c^2}{2k\nu^2} I_\nu, \tag{C.1}$$

where $T_{\rm B}$ is in units of Kelvin and I_ν is in units of $\mathrm{ergs\,cm^{-2}\,s^{-1}\,Hz^{-2}\,steradian^{-1}}$. To convert between I_ν and Λ' (by unit analysis)

$$\begin{aligned} I_\nu\,[\mathrm{ergs\,cm^{-2}\,s^{-1}\,Hz^{-2}\,steradian^{-1}}] &= \Lambda'\,[\mathrm{ergs\,cm^{-3}\,s^{-1}\,X_{CO}^{-1}}] X_{\rm CO} \\ &\quad \times \frac{l\,[\mathrm{cm}]}{\Delta\nu\,[\mathrm{Hz}]} \frac{1}{\Delta\Omega\,[\mathrm{steradians}]}, \end{aligned} \tag{C.2}$$

where l is the source size along the line of sight, $\Delta\nu$ is the line width, and $\Delta\Omega$ is the source size in the plane of the sky. The $X_{\rm CO} l/\Delta\nu$ term is effectively the CO abundance per unit velocity gradient if we convert the line width in Hz to $\mathrm{km\,s^{-1}}$ using $\Delta v/c = \Delta\nu/\nu$. The CO abundance per unit velocity gradient is related to two of the LVG input parameters, the

CO column density per unit velocity and the H_2 density, by

$$X_{\rm CO}/(dv/dr) = \frac{N_{\rm CO}/\Delta v}{n_{\rm H_2}}. \tag{C.3}$$

Substituting these equations into the expression for I_ν and plugging that into the brightness temperature relation, we now have an equation that lets us relate our model parameters to the brightness temperature,

$$\begin{aligned} T_{\rm B}[{\rm K}] &= \frac{c^3[{\rm cm\,s^{-1}}]^3 \times 10^{-5}[{\rm km\,cm^{-1}}]}{2\,k[{\rm ergs\,K^{-1}}]\,\nu^3[{\rm Hz}]^3} \\ &\quad \times \frac{\Lambda'[{\rm ergs\,cm^{-3}\,s^{-1}\,X_{CO}^{-1}}]\,N_{\rm CO}/\Delta v[{\rm cm^{-2}\,(km/s)^{-1}}]}{n_{\rm H_2}[{\rm cm^{-3}}]\,\Delta\Omega[{\rm ster}]}, \end{aligned} \tag{C.4}$$

where the factor of 10^{-5} comes from the need for one of the factors of c to be in units of $\rm km\,s^{-1}$. Plugging in constants, and converting some terms into more useful units, this equation becomes:

$$T_{\rm B}[{\rm K}] = 4.15149 \times 10^{25} \frac{\Lambda'[{\rm ergs\,cm^{-3}\,s^{-1}\,X_{CO}^{-1}}]\,N_{\rm CO}/\Delta v[{\rm cm^{-2}\,(km/s)^{-1}}]}{\nu^3[{\rm GHz}]^3\,n_{\rm H_2}[{\rm cm^{-3}}]\,\Delta\Omega[{\rm arcsec^2}]}. \tag{C.5}$$

Using this equation for the brightness temperature, we can transform our cut on $T_{\rm B}$ to one on Λ':

$$\begin{aligned} \Lambda'[{\rm ergs\,cm^{-3}\,s^{-1}\,X_{CO}^{-1}}] &> \alpha\,\Delta\Omega[{\rm arcsec^2}]\,\nu^3[{\rm GHz}]^3 \\ &\quad \times \frac{T_{\rm kin}[{\rm K}]\,n_{\rm H_2}[{\rm cm^{-3}}]}{4.15149 \times 10^{25}\,N_{\rm CO}/\Delta v[{\rm cm^{-2}\,(km/s)^{-1}}]}. \end{aligned} \tag{C.6}$$

Therefore, for a cut in line brightness temperature, we need to choose a sensible source size as well as how high above the kinetic temperature we want the brightness temperature to be. Output values of Λ' for J00266 range from 7.68×10^{-30} to $3.48\times10^{-13}\,{\rm ergs\,cm^{-3}\,s^{-1}\,X_{CO}^{-1}}$ with a median value of $3.33\times10^{-18}\,{\rm ergs\,cm^{-3}\,s^{-1}\,X_{CO}^{-1}}$. For the CO(1–0) line, the right side of Equation C.6 (not including the $\alpha\Delta\Omega$ terms) ranges beween $2.66\times10^{-35} - 2.66\times10^{-25}$

(excluding models with kinetic temperatures equal to zero, and using the standard ranges I've been using in model parameters). Based on these ranges, one can see that even for choices in source size solid angle that are an order of magnitude too high and values of $\alpha > 1$, not much of the parameter space will be excluded based on cuts in brightness temperature. In practice, the excluded regions all lie at temperatures less than that of the CMB at high redshift, which are already removed from the acceptable range of parameters.

C.2 Column Length

Another physically motivated prior is that column length predicted by the LVG model must be less than the source diameter, $l_{CO} \leq D$ (Ward et al. 2003). Translated into the parameters of the LVG analysis, this cut becomes:

$$\frac{N_{\rm CO}/\Delta v}{n_{\rm H_2}} \frac{\Delta v}{X_{\rm CO,max}} \leq D. \tag{C.7}$$

To implement this cut, we must have measured values of the source diameter and velocity width, as well as choose a maximum value of the CO-to-H_2 abundance. This effectively makes the column length prior a cut on the maximum value of $X_{\rm CO}/(dv/dr)$, a common parameter choice in the LVG modeling that can be used instead of $N_{\rm CO}/\Delta v$.

In the case of J00266, the velocity gradients for both components are approximately the same (assuming no correction for magnification). For the red component, the line FWHM is $\sim 340\,{\rm km\,s^{-1}}$ and major axis FWHM is 8.88 kpc in the rest frame. For the blue component, the line FWHM is $\sim 165\,{\rm km\,s^{-1}}$ and source size FWHM is 5.84 kpc in the rest frame. These correspond to velocity gradients of $0.04\,{\rm km\,s^{-1}\,pc^{-1}}$ and $0.03\,{\rm km\,s^{-1}\,pc^{-1}}$. Ward et al. (2003) conservatively assume that $X_{\rm CO,max} = 5 \times 10^{-4}$, based on measurements in Galactic star formation regions. For the moment, I will be even more conservative and assume $X_{\rm CO,max} = 1 \times 10^{-4}$, which effectively eliminates $\log((X_{\rm CO}/dv/dr)/({\rm km^{-1}\,s\,pc})) \gtrsim -2.5$, i.e., $\sim 40\%$ of the available LVG parameter space.

Implementing this cut in the two-phase modeling is somewhat trickier since the strongest forms of this prior would require factoring in the filling fractions of the two components. In addition, most of the stronger forms of this prior (such as requiring the cold phase column

length to be less than the source diameter × the cold filling fraction) require knowing *both* the cold *and* warm fractions (which is what Ward et al. (2003) do for their two-phase modeling); we only model the ratio of those factors and do not want to increase the number of free parameters further. Therefore, it is easiest to implement the weakest form of the prior, which is to require that the cold phase column length and warm phase column length both be independently shorter than the source diameter, without factoring in the filling fractions.

C.3 Virialized Gas

Constraints on the gas conditions can also be made by considering the gas dynamics. The degree of virialization can be calculated using the ratio of the source's velocity gradient (either a measured quantity or a quantity determined from the LVG models) to the expected velocity gradient for virialized gas with the best-fit model density:

$$K_{\rm vir} = \frac{\Delta v/\Delta r}{(\Delta v/\Delta r)_{\rm vir}} \sim \frac{1.54}{\sqrt{a}}\frac{\Delta v}{\Delta r}\left[\frac{\langle n_{\rm H_2}\rangle}{10^3\,{\rm cm^{-3}}}\right]^{-1/2} = 1.54\frac{[{\rm CO/H_2}]}{\sqrt{\alpha}\Lambda_{\rm CO}}\left[\frac{\langle n_{\rm H_2}\rangle}{10^3\,{\rm cm^{-3}}}\right]^{-1/2}. \quad \text{(C.8)}$$

In this equation, $\Lambda_{\rm CO} = [{\rm CO/H_2}]/(\Delta v/\Delta r)$ (i.e., what I call $X_{\rm CO}/(\Delta v/\Delta r)$) and $\alpha = 1$–2.5 depending on the cloud geometry (e.g., Papadopoulos & Seaquist 1999; Goldsmith 2001; Greve et al. 2009; Papadopoulos et al. 2010; Ivison et al. 2011); the middle expression is used in cases where the velocity gradient can be measured, and the last expression is used in alternative parameterizations of LVG models that use $\Lambda_{\rm CO}$ instead of $N_{\rm CO}/\Delta v$. For $K_{\rm vir} \sim 1$, the gas is self-gravitating, which is likely for most star-forming material. $K_{\rm vir} \gg 1$ would correspond to unbound gas motions, and $K_{\rm vir} \ll 1$ would be "dynamically unobtainable kinematic gas states" (Ivison et al. 2011). For an assumed value of α and a measured velocity gradient, any priors that are functions of $K_{\rm vir}$ are effectively just cuts on the H_2 density. For an average $\alpha = 1.75$ and J00266's red component velocity gradient, we probe $1.40951 < K_{\rm vir} < 0.00045$, which means we only probe ranges in the molecular gas density that are somewhere between gravitationally bound and unrealistic. Thus, if we choose to eliminate $K_{\rm vir} < 0.01$, we eliminate LVG models with $\log(n_{\rm H_2}/{\rm cm^{-3}}) \gtrsim 10^4$.

C.4 Optical Depth

Since emission lines with large optical depths are likely to overwhelm any emission from lower optical depth, we can eliminate LVG parameters giving $\tau < 1$. The optical depth is calculated for each parameter triplet in order to determine the escape probability in the LVG code, which is written out along with the line strength. In practice at the redshift of J00266, requiring $\tau < 1$ removes about 40% of the available parameter space, including nearly everything below $N_{\rm CO}/\Delta v = 10^{17}\,{\rm cm}^{-2}\,({\rm km/s})^{-1}$.

C.5 A Spatially Extended Low-density Cold Phase

Our current model of the multi-phase molecular ISM in SMGs is that the galaxy is effectively one giant molecular cloud; SMGs contain vast reservoirs of cold, low-density gas punctuated by smaller knots of actively star-forming material at higher temperatures and densities. This understanding can be implemented in terms of two obvious priors: (1) that the cold H_2 density be lower than the warm phase density, and (2) the cold phase filling fraction be larger than the warm phase filling fraction.

C.6 The Cold Phase Dominates the CO(1–0) Emission

Ward et al. (2003) introduce a prior that the dominant source of the low-J emission must be the cold phase gas (in their case 20% of the CO(2–1) line). I have implemented a similar prior such that 90% of the CO(1–0) line in the red component of J00266 must come from the cold phase material:

$$\frac{\Lambda'_{\rm c,1-0}}{\Lambda'_{\rm c,1-0} + \frac{f_{\rm w}}{f_{\rm c}}\Lambda'_{\rm w,1-0}} > 0.90. \tag{C.9}$$

Ward et al. (2003) use this prior to remove an unphysical spike in the probability at the lowest possible temperature. For J00266, unless the cut was increased to 90% of the CO(1–0) line coming from the cold phase, this prior had little effect.

C.7 Gas Mass

Another physically motivated prior is requiring the molecular gas mass to be less than the dynamical mass. This prior is used in the Ward et al. (2003) for their two-phase models, aalthough they require their gas mass to be less than half of the dynamical mass:

$$\Phi_{\rm w} N_{\rm w} + \Phi_{\rm c} N_{\rm c} < \frac{1}{2} \frac{M_{\rm dyn}}{m_{\rm H_2}} \frac{X_{\rm CO,max}}{A_{\rm beam}}. \tag{C.10}$$

Since we do not have independent values for the cold and warm filling fractions (their Φ in Equation C.10), we are restricted to using this prior in only single-phase models. Converting Equation C.10 into sensible units, and accounting for the fact that we use the column density per unit velocity gradient, this cut becomes

$$N_{\rm CO}/\Delta v[{\rm cm}^{-2}\,({\rm km/s})^{-1}] < 9.75 \times 10^{11} \frac{M_{\rm dyn}[M_\odot] X_{\rm CO,max}}{\Delta v[{\rm km\,s^{-1}}] \Delta\Omega[{\rm arcsec}^2]}, \tag{C.11}$$

where we have not included the factor of one-half included in Ward et al. (2003). For the red component of J00266, this prior eliminates $N_{\rm CO}/\Delta v > 10^{18}\,{\rm cm}^{-2}\,({\rm km/s})^{-1}$. Combining this prior with the optical depth prior effectively limits us to a very small range in $N_{\rm CO}/\Delta v$ without more knowledge about the beam filling fraction.

Bibliography

Aguirre, P. A., Baker, A. J., Menanteau, F., Lutz, D., & Tacconi, L. J. 2013, ApJ, in press

Alaghband-Zadeh, S., Chapman, S. C., Swinbank, A. M., et al. 2012, MNRAS, 424, 2232

Alexander, D. M., Bauer, F. E., Brandt, W. N., et al. 2003, AJ, 125, 383

Aravena, M., Younger, J. D., Fazio, G. G., et al. 2010, ApJ, 719, L15

Arimoto, N., Sofue, Y., & Tsujimoto, T. 1996, PASJ, 48, 275

Baker, A. J., Lutz, D., Genzel, R., Tacconi, L. J., & Lehnert, M. D. 2001, A&A, 372, L37

Baker, A. J., Tacconi, L. J., Genzel, R., Lehnert, M. D., & Lutz, D. 2004, ApJ, 604, 125

Baldwin, J. A., Phillips, M. M., & Terlevich, R. 1981, PASP, 93, 5

Balland, C., Devriendt, J. E. G., & Silk, J. 2003, MNRAS, 343, 107

Barger, A. J., Cowie, L. L., Sanders, D. B., et al. 1998, Nature, 394, 248

Barger, A. J., Cowie, L. L., Smail, I., et al. 1999, AJ, 117, 2656

Barvainis, R., & Ivison, R. 2002, ApJ, 571, 712

Baugh, C. M., Lacey, C. G., Frenk, C. S., et al. 2005, MNRAS, 356, 1191

Bayet, E., Gerin, M., Phillips, T. G., & Contursi, A. 2004, A&A, 427, 45

—. 2009, MNRAS, 399, 264

Bertoldi, F., Carilli, C. L., Menten, K. M., et al. 2000, A&A, 360, 92

Béthermin, M., Le Floc'h, E., Ilbert, O., et al. 2012, A&A, 542, A58

Bigiel, F., Leroy, A., Walter, F., et al. 2010, AJ, 140, 1194

—. 2008, AJ, 136, 2846

Binney, J., Gerhard, O., & Silk, J. 2001, MNRAS, 321, 471

Blain, A. W. 1999, MNRAS, 304, 669

Blain, A. W., Chapman, S. C., Smail, I., & Ivison, R. 2004, ApJ, 611, 725

Blain, A. W., Jameson, A., Smail, I., et al. 1999, MNRAS, 309, 715

Blain, A. W., Smail, I., Ivison, R. J., Kneib, J.-P., & Frayer, D. T. 2002, Phys. Rep., 369, 111

Bloemen, J. B. G. M., Strong, A. W., Mayer-Hasselwander, H. A., et al. 1986, A&A, 154, 25

Bolatto, A. D., Leroy, A. K., Rosolowsky, E., Walter, F., & Blitz, L. 2008, ApJ, 686, 948

Bonfield, D. G., Jarvis, M. J., Hardcastle, M. J., et al. 2011, MNRAS, 416, 13

Bongiorno, A., Zamorani, G., Gavignaud, I., et al. 2007, A&A, 472, 443

Bothwell, M. S., Smail, I., Chapman, S. C., et al. 2013, MNRAS, 429, 3047

Bouché, N., Cresci, G., Davies, R., et al. 2007, ApJ, 671, 303

Bouchet, P., Lequeux, J., Maurice, E., Prevot, L., & Prevot-Burnichon, M. L. 1985, A&A, 149, 330

Bournaud, F., Chapon, D., Teyssier, R., et al. 2011, ApJ, 730, 4

Bromm, V., & Larson, R. B. 2004, ARA&A, 42, 79

Brook, C. B., Governato, F., Roškar, R., et al. 2011, MNRAS, 415, 1051

Buat, V., Deharveng, J. M., & Donas, J. 1989, A&A, 223, 42

Bussmann, R. S., Narayanan, D., Shirley, Y. L., et al. 2008, ApJ, 681, L73

Calzetti, D., Kinney, A. L., & Storchi-Bergmann, T. 1994, ApJ, 429, 582

Calzetti, D., Kennicutt, R. C., Engelbracht, C. W., et al. 2007, ApJ, 666, 870

Calzetti, D., Wu, S.-Y., Hong, S., et al. 2010, ApJ, 714, 1256

Carilli, C. L., Cox, P., Bertoldi, F., et al. 2002, ApJ, 575, 145

Carilli, C. L., Daddi, E., Riechers, D., et al. 2010, ApJ, 714, 1407

Cecchi-Pestellini, C., Bodo, E., Balakrishnan, N., & Dalgarno, A. 2002, ApJ, 571, 1015

Chabrier, G. 2003, PASP, 115, 763

Chapin, E. L., Pope, A., Scott, D., et al. 2009, MNRAS, 398, 1793

Chapman, S. C., Blain, A. W., Smail, I., & Ivison, R. J. 2005, ApJ, 622, 772

Cole, S., Lacey, C. G., Baugh, C. M., & Frenk, C. S. 2000, MNRAS, 319, 168

Conselice, C. J., Chapman, S. C., & Windhorst, R. A. 2003, ApJ, 596, L5

Coppin, K., Pope, A., Menéndez-Delmestre, K., et al. 2010, ApJ, 713, 503

Coppin, K. E. K., Swinbank, A. M., Neri, R., et al. 2007, ApJ, 665, 936

Cowie, L. L., Barger, A. J., Bautz, M. W., Brandt, W. N., & Garmire, G. P. 2003, ApJ, 584, L57

Daddi, E., Elbaz, D., Walter, F., et al. 2010, ApJ, 714, L118

Danielson, A. L. R., Swinbank, A. M., Smail, I., et al. 2011, MNRAS, 410, 1687

Dannerbauer, H., Daddi, E., Riechers, D. A., et al. 2009, ApJ, 698, L178

Davé, R., Finlator, K., Oppenheimer, B. D., et al. 2010, MNRAS, 404, 1355

Devlin, M. J., Ade, P. A. R., Aretxaga, I., et al. 2009, Nature, 458, 737

Devriendt, J. E. G., & Guiderdoni, B. 2000, A&A, 363, 851

Dickman, R. L. 1978, ApJS, 37, 407

Dickman, R. L., Snell, R. L., & Schloerb, F. P. 1986, ApJ, 309, 326

Diehl, H. T., Allam, S. S., Annis, J., et al. 2009, ApJ, 707, 686

Domínguez, A., Primack, J. R., Rosario, D. J., et al. 2011, MNRAS, 410, 2556

Downes, D., & Solomon, P. M. 1998, ApJ, 507, 615

—. 2003, ApJ, 582, 37

Downes, D., Solomon, P. M., & Radford, S. J. E. 1993, ApJ, 414, L13

Elbaz, D., Daddi, E., Le Borgne, D., et al. 2007, A&A, 468, 33

Elmegreen, B. G. 2002, ApJ, 577, 206

Engel, H., Tacconi, L. J., Davies, R. I., et al. 2010, ApJ, 724, 233

Engelbracht, C. W., Gordon, K. D., Rieke, G. H., et al. 2005, ApJ, 628, L29

Fabian, A. C., Smail, I., Iwasawa, K., et al. 2000, MNRAS, 315, L8

Fadely, R., Allam, S. S., Baker, A. J., et al. 2010, ApJ, 723, 729

Ferrarese, L., & Merritt, D. 2000, ApJ, 539, L9

Fixsen, D. J., Dwek, E., Mather, J. C., Bennett, C. L., & Shafer, R. A. 1998, ApJ, 508, 123

Fontanot, F., Monaco, P., Silva, L., & Grazian, A. 2007, MNRAS, 382, 903

Frayer, D. T., Ivison, R. J., Scoville, N. Z., et al. 1998, ApJ, 506, L7

Frayer, D. T., Reddy, N. A., Armus, L., et al. 2004, AJ, 127, 728

Frayer, D. T., Smail, I., Ivison, R. J., & Scoville, N. Z. 2000, AJ, 120, 1668

Frayer, D. T., Ivison, R. J., Scoville, N. Z., et al. 1999, ApJ, 514, L13

Gao, Y., & Solomon, P. M. 2004, ApJ, 606, 271

Garcia-Burillo, S., Guelin, M., & Cernicharo, J. 1993, A&A, 274, 123

Gebhardt, K., Bender, R., Bower, G., et al. 2000, ApJ, 539, L13

Genzel, R., Baker, A. J., Tacconi, L. J., et al. 2003, ApJ, 584, 633

Genzel, R., Tacconi, L. J., Gracia-Carpio, J., et al. 2010, MNRAS, 407, 2091

Genzel, R., Tacconi, L. J., Combes, F., et al. 2012, ApJ, 746, 69

Giavalisco, M. 2002, ARA&A, 40, 579

Gilmore, R. C., Somerville, R. S., Primack, J. R., & Domínguez, A. 2012, MNRAS, 422, 3189

Glover, S. C. O., & Mac Low, M.-M. 2011, MNRAS, 412, 337

Goldreich, P., & Kwan, J. 1974, ApJ, 189, 441

Goldsmith, P. F. 2001, ApJ, 557, 736

Graciá-Carpio, J., García-Burillo, S., Planesas, P., Fuente, A., & Usero, A. 2008, A&A, 479, 703

Granato, G. L., Lacey, C. G., Silva, L., et al. 2000, ApJ, 542, 710

Granato, G. L., Silva, L., Monaco, P., et al. 2001, MNRAS, 324, 757

Greve, T. R., Ivison, R. J., & Papadopoulos, P. P. 2003, ApJ, 599, 839

—. 2004, A&A, 419, 99

Greve, T. R., Papadopoulos, P. P., Gao, Y., & Radford, S. J. E. 2009, ApJ, 692, 1432

Greve, T. R., Bertoldi, F., Smail, I., et al. 2005, MNRAS, 359, 1165

Guesten, R., Serabyn, E., Kasemann, C., et al. 1993, ApJ, 402, 537

Guiderdoni, B., Hivon, E., Bouchet, F. R., & Maffei, B. 1998, MNRAS, 295, 877

Guilloteau, S., & Lucas, R. 2000, in Astronomical Society of the Pacific Conference Series, Vol. 217, Imaging at Radio through Submillimeter Wavelengths, ed. J. G. Mangum & S. J. E. Radford, 299

Guilloteau, S., Delannoy, J., Downes, D., et al. 1992, A&A, 262, 624

Hainline, K. N., Shapley, A. E., Kornei, K. A., et al. 2009, ApJ, 701, 52

Hainline, L. J., Blain, A. W., Greve, T. R., et al. 2006, ApJ, 650, 614

Hainline, L. J., Blain, A. W., Smail, I., et al. 2011, ApJ, 740, 96

Hao, C.-N., Kennicutt, R. C., Johnson, B. D., et al. 2011, ApJ, 741, 124

Harris, A. I., Baker, A. J., Zonak, S. G., et al. 2010, ApJ, 723, 1130

Harris, A. I., Baker, A. J., Jewell, P. R., et al. 2007, in Astronomical Society of the Pacific Conference Series, Vol. 375, From Z-Machines to ALMA: (Sub)Millimeter Spectroscopy of Galaxies, ed. A. J. Baker, J. Glenn, A. I. Harris, J. G. Mangum, & M. S. Yun , 82

Harris, A. I., Baker, A. J., Frayer, D. T., et al. 2012, ApJ, 752, 152

Hayward, C. C., Kereš, D., Jonsson, P., et al. 2011, ApJ, 743, 159

Hayward, C. C., Narayanan, D., Kereš, D., et al. 2013, MNRAS, 428, 2529

Hernquist, L. 1989, Nature, 340, 687

Hinz, J. L., & Rieke, G. H. 2006, ApJ, 646, 872

Hodge, J. A., Carilli, C. L., Walter, F., et al. 2012, ApJ, 760, 11

Holland, W. S., Robson, E. I., Gear, W. K., et al. 1999, MNRAS, 303, 659

Hollenbach, D. J., & Tielens, A. G. G. M. 1997, ARA&A, 35, 179

Hopkins, A. M., & Beacom, J. F. 2006, ApJ, 651, 142

Howarth, I. D. 1983, MNRAS, 203, 301

Hughes, D. H., Serjeant, S., Dunlop, J., et al. 1998, Nature, 394, 241

Iono, D., Wilson, C. D., Yun, M. S., et al. 2009, ApJ, 695, 1537

Israel, F. P. 1997, A&A, 328, 471

Ivison, R. J., Papadopoulos, P. P., Smail, I., et al. 2011, MNRAS, 412, 1913

Ivison, R. J., Smail, I., Barger, A. J., et al. 2000, MNRAS, 315, 209

Ivison, R. J., Smail, I., Frayer, D. T., Kneib, J.-P., & Blain, A. W. 2001, ApJ, 561, L45

Ivison, R. J., Smail, I., Papadopoulos, P. P., et al. 2010, MNRAS, 404, 198

Ivison, R. J., Smail, I., Amblard, A., et al. 2012, MNRAS, 425, 1320

Juneau, S., Narayanan, D. T., Moustakas, J., et al. 2009, ApJ, 707, 1217

Karim, A., Swinbank, M., Hodge, J., et al. 2012, ArXiv e-prints

Kauffmann, G., Heckman, T. M., Tremonti, C., et al. 2003, MNRAS, 346, 1055

Kaviani, A., Haehnelt, M. G., & Kauffmann, G. 2003, MNRAS, 340, 739

Kennicutt, R. C., & Evans, N. J. 2012, ARA&A, 50, 531

Kennicutt, Jr., R. C. 1989, ApJ, 344, 685

—. 1998, ApJ, 498, 541

Kennicutt, Jr., R. C., Calzetti, D., Walter, F., et al. 2007, ApJ, 671, 333

Klamer, I. J., Ekers, R. D., Sadler, E. M., et al. 2005, ApJ, 621, L1

Komatsu, E., Smith, K. M., Dunkley, J., et al. 2011, ApJS, 192, 18

Kong, X., Charlot, S., Brinchmann, J., & Fall, S. M. 2004, MNRAS, 349, 769

Koornneef, J., & Code, A. D. 1981, ApJ, 247, 860

Kreysa, E., Gemuend, H.-P., Gromke, J., et al. 1998, in Society of Photo-Optical Instrumentation Engineers (SPIE) Conference Series, Vol. 3357, Society of Photo-Optical Instrumentation Engineers (SPIE) Conference Series, ed. T. G. Phillips, 319

Kroupa, P., Tout, C. A., & Gilmore, G. 1993, MNRAS, 262, 545

Krumholz, M. R., McKee, C. F., & Klein, R. I. 2005, Nature, 438, 332

Krumholz, M. R., McKee, C. F., & Tumlinson, J. 2009, ApJ, 699, 850

Krumholz, M. R., & Thompson, T. A. 2007, ApJ, 669, 289

La Franca, F., Fiore, F., Comastri, A., et al. 2005, ApJ, 635, 864

Lacey, C., & Silk, J. 1991, ApJ, 381, 14

Lacey, C. G., Baugh, C. M., Frenk, C. S., et al. 2008, MNRAS, 385, 1155

Lagache, G., Abergel, A., Boulanger, F., Désert, F. X., & Puget, J.-L. 1999, A&A, 344, 322

Larson, R. B. 1981, MNRAS, 194, 809

Le Floc'h, E., Aussel, H., Ilbert, O., et al. 2009, ApJ, 703, 222

Leroy, A., Bolatto, A., Walter, F., & Blitz, L. 2006, ApJ, 643, 825

Li, Y., Mac Low, M.-M., & Klessen, R. S. 2005, ApJ, 626, 823

Loeb, A., & Barkana, R. 2001, ARA&A, 39, 19

Low, F. J., & Tucker, W. H. 1968, Physical Review Letters, 21, 1538

Lutz, D., Valiante, E., Sturm, E., et al. 2005, ApJ, 625, L83

Lutz, D., Sturm, E., Tacconi, L. J., et al. 2008, ApJ, 684, 853

Madau, P., Ferguson, H. C., Dickinson, M. E., et al. 1996, MNRAS, 283, 1388

Madden, S. C. 2000, New Astronomy Reviews, 44, 249

Maller, A. H., & Dekel, A. 2002, MNRAS, 335, 487

Mao, R. Q., Henkel, C., Schulz, A., et al. 2000, A&A, 358, 433

Mauersberger, R., Henkel, C., Walsh, W., & Schulz, A. 1999, A&A, 341, 256

McKee, C. F., & Ostriker, E. C. 2007, ARA&A, 45, 565

Meier, D. S., Turner, J. L., Beck, S. C., et al. 2010, AJ, 140, 1294

Menéndez-Delmestre, K., Blain, A. W., Smail, I., et al. 2009, ApJ, 699, 667

Motohara, K., Takata, T., Iwamuro, F., et al. 2005, AJ, 129, 53

Moustakas, J., Kennicutt, Jr., R. C., & Tremonti, C. A. 2006, ApJ, 642, 775

Murphy, E. J., Condon, J. J., Schinnerer, E., et al. 2011, ApJ, 737, 67

Narayanan, D., Cox, T. J., Hayward, C. C., & Hernquist, L. 2011, MNRAS, 412, 287

Narayanan, D., Cox, T. J., Shirley, Y., et al. 2008, ApJ, 684, 996

Narayanan, D., Groppi, C. E., Kulesa, C. A., & Walker, C. K. 2005, ApJ, 630, 269

Narayanan, D., Hayward, C. C., Cox, T. J., et al. 2010, MNRAS, 401, 1613

Narayanan, D., Krumholz, M. R., Ostriker, E. C., & Hernquist, L. 2012, MNRAS, 421, 3127

Neri, R., Genzel, R., Ivison, R. J., et al. 2003, ApJ, 597, L113

Nesvadba, N. P. H., Lehnert, M. D., Genzel, R., et al. 2007, ApJ, 657, 725

Netzer, H., Lutz, D., Schweitzer, M., et al. 2007, ApJ, 666, 806

Niemi, S.-M., Somerville, R. S., Ferguson, H. C., et al. 2012, MNRAS, 421, 1539

Oka, T., Hasegawa, T., Hayashi, M., Handa, T., & Sakamoto, S. 1998, ApJ, 493, 730

Papadopoulos, P., Ivison, R., Carilli, C., & Lewis, G. 2001, Nature, 409, 58

Papadopoulos, P. P., & Seaquist, E. R. 1999, ApJ, 516, 114

Papadopoulos, P. P., van der Werf, P., Isaak, K., & Xilouris, E. M. 2010, ApJ, 715, 775

Partridge, R. B., & Peebles, P. J. E. 1967, ApJ, 148, 377

Pope, A., Scott, D., Dickinson, M., et al. 2006, MNRAS, 370, 1185

Puget, J., Abergel, A., Bernard, J., et al. 1996, A&A, 308, L5

Ranalli, P., Comastri, A., & Setti, G. 2003, A&A, 399, 39

Reddy, N. A., & Steidel, C. C. 2009, ApJ, 692, 778

Riechers, D. A. 2013, ApJ, 765, L31

Riechers, D. A., Carilli, C. L., Walter, F., & Momjian, E. 2010, ApJ, 724, L153

Riechers, D. A., Walter, F., Carilli, C. L., et al. 2006, ApJ, 650, 604

Riechers, D. A., Carilli, C. L., Maddalena, R. J., et al. 2011a, ApJ, 739, L32

Riechers, D. A., Cooray, A., Omont, A., et al. 2011b, ApJ, 733, L12

Riechers, D. A., Carilli, L. C., Walter, F., et al. 2011c, ApJ, 733, L11

Rieke, G. H., Alonso-Herrero, A., Weiner, B. J., et al. 2009, ApJ, 692, 556

Rigby, J. R., Marcillac, D., Egami, E., et al. 2008, ApJ, 675, 262

Rodighiero, G., Daddi, E., Baronchelli, I., et al. 2011, ApJ, 739, L40

Rowan-Robinson, M. 1995, MNRAS, 272, 737

Salpeter, E. E. 1955, ApJ, 121, 161

Sanders, D. B., & Mirabel, I. F. 1996, ARA&A, 34, 749

Sanders, D. B., Scoville, N. Z., & Soifer, B. T. 1991, ApJ, 370, 158

Sargent, M. T., Béthermin, M., Daddi, E., & Elbaz, D. 2012, ApJ, 747, L31

Schmidt, M. 1959, ApJ, 129, 243

Schruba, A., Leroy, A. K., Walter, F., et al. 2011, AJ, 142, 37

Scoville, N. Z., Sargent, A. I., Sanders, D. B., & Soifer, B. T. 1991, ApJ, 366, L5

Scoville, N. Z., & Solomon, P. M. 1974, ApJ, 187, L67

Scoville, N. Z., Yun, M. S., & Bryant, P. M. 1997, ApJ, 484, 702

Serjeant, S. 2012, MNRAS, 424, 2429

Sharon, C. E., Baker, A. J., Harris, A. I., & Thomson, A. P. 2013a, ApJ, 765, 6

Sharon, C. E., Harris, A. I., Lutz, D., Tacconi, L. J., & Longmore, S. 2013b, (in prep.)

Shu, F. H., Adams, F. C., & Lizano, S. 1987, ARA&A, 25, 23

Silk, J. 1997, ApJ, 481, 703

Smail, I., Chapman, S. C., Blain, A. W., & Ivison, R. J. 2004, ApJ, 616, 71

Smail, I., Ivison, R. J., & Blain, A. W. 1997, ApJ, 490, L5

Smail, I., Ivison, R. J., Blain, A. W., & Kneib, J. 1998, ApJ, 507, L21

—. 2002, MNRAS, 331, 495

Smail, I., Smith, G. P., & Ivison, R. J. 2005, ApJ, 631, 121

Solomon, P. M., & Barrett, J. W. 1991, in IAU Symposium, Vol. 146, Dynamics of Galaxies and Their Molecular Cloud Distributions, ed. F. Combes & F. Casoli, 235

Solomon, P. M., Downes, D., Radford, S. J. E., & Barrett, J. W. 1997, ApJ, 478, 144

Solomon, P. M., Rivolo, A. R., Barrett, J., & Yahil, A. 1987, ApJ, 319, 730

Solomon, P. M., & Sage, L. J. 1988, ApJ, 334, 613

Solomon, P. M., & Vanden Bout, P. A. 2005, ARA&A, 43, 677

Somerville, R. S., Gilmore, R. C., Primack, J. R., & Domínguez, A. 2012, MNRAS, 423, 1992

Somerville, R. S., Hopkins, P. F., Cox, T. J., Robertson, B. E., & Hernquist, L. 2008, MNRAS, 391, 481

Somerville, R. S., Primack, J. R., & Faber, S. M. 2001, MNRAS, 320, 504

Strong, A. W., Bloemen, J. B. G. M., Dame, T. M., et al. 1988, A&A, 207, 1

Swinbank, A. M., Smail, I., Chapman, S. C., et al. 2004, ApJ, 617, 64

Swinbank, A. M., Lacey, C. G., Smail, I., et al. 2008, MNRAS, 391, 420

Swinbank, A. M., Smail, I., Chapman, S. C., et al. 2010a, MNRAS, 405, 234

Swinbank, A. M., Smail, I., Longmore, S., et al. 2010b, Nature, 464, 733

Swinbank, A. M., Papadopoulos, P. P., Cox, P., et al. 2011, ApJ, 742, 11

Tacconi, L. J., Neri, R., Chapman, S. C., et al. 2006, ApJ, 640, 228

Tacconi, L. J., Genzel, R., Smail, I., et al. 2008, ApJ, 680, 246

Tacconi, L. J., Genzel, R., Neri, R., et al. 2010, Nature, 463, 781

Tacconi, L. J., Neri, R., Genzel, R., et al. 2012, ArXiv e-prints

Takahashi, J. 2001, ApJ, 561, 254

Takeuchi, T. T., Buat, V., & Burgarella, D. 2005, A&A, 440, L17

Tecza, M., Baker, A. J., Davies, R. I., et al. 2004, ApJ, 605, L109

Thomas, D., Maraston, C., Bender, R., & Mendes de Oliveira, C. 2005, ApJ, 621, 673

Thomson, A. P., Ivison, R. J., Smail, I., et al. 2012, MNRAS, 425, 2203

Valiante, E., Lutz, D., Sturm, E., et al. 2007, ApJ, 660, 1060

van der Tak, F. F. S., Black, J. H., Schöier, F. L., Jansen, D. J., & van Dishoeck, E. F. 2007, A&A, 468, 627

Veilleux, S., Cecil, G., & Bland-Hawthorn, J. 2005, ARA&A, 43, 769

Vieira, J. D., Marrone, D. P., Chapman, S. C., et al. 2013, Nature, 495, 344

Voit, G. M. 1992, MNRAS, 258, 841

Walter, F., Weiß, A., Downes, D., Decarli, R., & Henkel, C. 2011, ApJ, 730, 18

Ward, J. S. 2002, PhD thesis, California Institute of Technology

Ward, J. S., Zmuidzinas, J., Harris, A. I., & Isaak, K. G. 2003, ApJ, 587, 171

Wardlow, J. L., Smail, I., Coppin, K. E. K., et al. 2011, MNRAS, 415, 1479

Wei, L. H., Vogel, S. N., Kannappan, S. J., et al. 2010, ApJ, 725, L62

Weiß, A., Downes, D., Henkel, C., & Walter, F. 2005a, A&A, 429, L25

Weiß, A., Downes, D., Walter, F., & Henkel, C. 2007, in Astronomical Society of the Pacific Conference Series, Vol. 375, From Z-Machines to ALMA: (Sub)Millimeter Spectroscopy of Galaxies, ed. A. J. Baker, J. Glenn, A. I. Harris, J. G. Mangum, & M. S. Yun , 25

Weiß, A., Henkel, C., Downes, D., & Walter, F. 2003, A&A, 409, L41

Weiß, A., Walter, F., & Scoville, N. Z. 2005b, A&A, 438, 533

White, S. D. M., & Frenk, C. S. 1991, ApJ, 379, 52

Wild, W., Harris, A. I., Eckart, A., et al. 1992, A&A, 265, 447

Wilson, C. D. 1995, ApJ, 448, L97

Wu, J., Vanden Bout, P. A., Evans, II, N. J., & Dunham, M. M. 2009, ApJ, 707, 988

Yang, B., Stancil, P. C., Balakrishnan, N., & Forrey, R. C. 2010, ApJ, 718, 1062

Yao, L., Seaquist, E. R., Kuno, N., & Dunne, L. 2003, ApJ, 588, 771

York, D. G., Adelman, J., Anderson, Jr., J. E., et al. 2000, AJ, 120, 1579

Young, J. S., Schloerb, F. P., Kenney, J. D., & Lord, S. D. 1986, ApJ, 304, 443

Young, J. S., & Scoville, N. Z. 1991, ARA&A, 29, 581

Yun, M. S., Scott, K. S., Guo, Y., et al. 2012, MNRAS, 420, 957

Zhu, M., Seaquist, E. R., & Kuno, N. 2003, ApJ, 588, 243